

Hannes Gruber, BSc

**Proof of concept – Characterization of roller bearings in  
racing applications**

**Entwicklung und Umsetzung eines Prüfkonzeptes zur  
Charakterisierung von Wälzlagern in  
Rennsportanwendungen**

**MASTER'S THESIS**

to achieve the university degree of

**Diplom-Ingenieur**

submitted to

**Graz University of Technology**

Faculty of Mechanical Engineering and Economic Sciences

Institute of Machine Components and Methods of Development

Supervisor: Assoc.Prof. Dipl.-Ing. Dr. techn. Michael Bader

Graz, 03.03.2019

Restricted access until 03.03.2021



# Acknowledgement

***“Innovation is infinite; there is always a next goal,  
and only the limits of science are the limits we should really accept.”***

*Prof. Dr. h.c. Helmut List*

Ever since I was a child, I wanted to learn how to design, build, test and maybe sometimes destroy things in the interest of science and for the greater good. On the way throughout my studies at the Technical University of Graz, I had the luck to meet people, now known as friends, who supported me beyond their obligations and helped me to fulfill my dream becoming a mechanical engineer.

I want to express my greatest thankfulness to Matthias Dank, Helmut Kokal, and Johann Eitzinger. Since my first day joining the AVL family, they gave personal and professional advice, listened to my problems, and helped me, whenever help was needed.

Additionally, I want to thank the team of the Institute of Machine Components at the TU Graz and especially Peter Haidl and Michael Bader for supporting me professionally throughout my entire thesis. Peter and Michael, thank you very much for all your patience and dedication during the last years.

Finally, my sincere and endlessly gratefulness goes to my family, especially to my parents Monika and Johann. Words could never express how grateful I am that I got the chance to choose my own path and that you spared no effort to support me in my decisions.

THANK YOU

# Statutory Declaration

I declare that I have authored this thesis independently, that I have not used other than the declared sources/resources, and I have explicitly marked all material which has been quoted either literally or by content from used sources.

.....

(Date)

.....

(Signature)

# Abstract

This thesis deals with the possibility to measure and compare the friction losses in a wheel bearing. For this purpose, the potential influencing factors should be assessed, based on a representative wheel hub bearing assembly and a list of requirements for a test concept should be defined. In compliance with the defined boundary conditions, different measurement and test approaches were evaluated, and a combination of methods was found to measure the friction torque with sufficient accuracy. The technique with the most significant potential for success was developed and validated in compliance with the previously created specification. The experimental setup shows that a steady-state load can be applied by tensioning two similar test specimens against each other. The forces simulate a tire-road contact, which has a significant influence on the total friction torque. Central data acquisition and test run automation can standardize data analysis. An existing friction torque calculation method can be adapted to provide speed and load dependent model for the statistical design of the experiment, taking into account the performed tests. Therefore a way was found, which finds the best possible configuration regarding their friction losses for bearing development parameters such as preload or lubricant quantity while minimizing the necessary number of tests.

# Kurzfassung

Die vorliegende Diplomarbeit befasst sich mit der Möglichkeit, die auftretenden Reibungsverluste in einem Radlager mess- und damit vergleichbar zu machen. Dazu sollen die potentiellen Einflussgrößen anhand eines repräsentativen Lagers ermittelt, beurteilt und eine Anforderungsliste für ein Prüfkonzept erstellt werden. Unter Einhaltung der definierten Randbedingungen wurden unterschiedliche Mess- und Prüfanordnungen bewertet und eine Kombination aus Technologien gefunden, mit der die Reibungsmessung mit ausreichender Genauigkeit durchgeführt werden kann. Die Methode mit dem größten Erfolgspotential wurde unter Berücksichtigung der zuvor erstellten Anforderungsliste entwickelt und validiert. Der Versuchsaufbau zeigt, dass mittels der symmetrischen Verspannung von zwei äquivalenten Prüflingen eine stationäre Last aufgebracht werden kann. Die so aufgebrauchten Kräfte simulieren einen Reifen-Straße-Kontakt, welcher einen signifikanten Einfluss auf das absolute Reibmoment zeigt. Durch eine zentrale Messdatenerfassung und Prüflaufautomatisierung kann die Datenerfassung standardisiert werden. Auf Basis der durchgeführten Messungen wurde eine bestehende Methode zur Reibmomentberechnung angepasst, wodurch ein drehzahl- und lastabhängiges Modell für eine statistische Versuchsplanung erstellt werden kann. Damit ist eine Methode gefunden, welche unter der Minimierung der notwendigen Versuchsreihen die bestmögliche Konfiguration hinsichtlich ihrer Reibungsverluste für Lagerparameter, wie Vorspannung oder Schmiermittelmenge und -art, findet.

# Contents

- Acknowledgment..... 3
- Statutory Declaration..... i
- Abstract ..... ii
- Kurzfassung ..... iii
- Contents..... iv
- Abbreviations..... vi
- Symbols..... vii
- 1 Introduction..... 8
  - 1.1 Motivation..... 8
  - 1.2 Target..... 9
- 2 Methodology and Theory..... 12
  - 2.1 UUT description..... 12
    - 2.1.1 Wheel speed distribution..... 12
    - 2.1.2 External bearing loads..... 13
    - 2.1.3 Test rig requirements ..... 17
  - 2.2 Efficiency measurement methods..... 18
    - 2.2.1 Torque measurement ..... 19
    - 2.2.2 Speed measurement..... 23
    - 2.2.3 Force measurement..... 25
  - 2.3 Evaluation of methods ..... 26
  - 2.4 Design parameters..... 29
  - 2.5 Friction torque estimation ..... 31
    - 2.5.1 Required torque estimation..... 31
    - 2.5.2 Tribology in rolling bearings ..... 34
- 3 Proof of concept - Layout..... 38
  - 3.1 Mechanical components..... 39
    - 3.1.1 Adjustable and locating frame ..... 40

3.1.2	Force application mechanism.....	41
3.1.3	Rotor assembly .....	42
3.1.4	Static simulation .....	43
3.1.5	Dynamic simulation.....	46
3.2	Drive Motor.....	48
3.3	Data acquisition & analysis .....	51
3.3.1	Speed signal .....	51
3.3.2	Temperature signal.....	52
3.3.3	Speed setpoint frequency.....	52
3.3.4	Data acquisition device .....	53
3.4	Assembly & Commissioning.....	54
4	Results .....	56
4.1	Commissioning tests.....	57
4.2	Repeatability force conditions.....	59
4.3	Repeatability and reproducibility .....	62
4.4	Overall Friction correlation .....	67
4.5	Design of experiments.....	69
5	Discussion .....	72
5.1	Conclusion.....	72
5.2	Outlook.....	73
	List of Figures.....	I
	List of Tables.....	III
	List of Appendices .....	IV
	Bibliography .....	V
A.	Appendix.....	VII

# Abbreviations

In alphabetical order:

<b>% FS</b>	Accuracy in % of the full measurement range
<b>% FS</b>	Accuracy in % of the defined target value
<b>AVL</b>	Anstalt für Verbrennungskraftmaschinen List
<b>CAD</b>	Computer aided design
<b>CAE</b>	Computer aided engineering
<b>comp</b>	Indices for compensated measured values
<b>DIN</b>	Deutsches Institut für Normung e. V.
<b>EHD</b>	Elastohydrodynamic
<b>GGV</b>	Performance envelope diagram
<b>GUI</b>	Graphical user interface
<b>HBM</b>	Hottinger Baldwin Messtechnik
<b>HMT</b>	Highest Measureable Torque
<b>HoQ</b>	House of Quality
<b>I/O</b>	Input/Output
<b>IRL</b>	Indy Racing League
<b>ISO</b>	International Organization for Standardization
<b>LMT</b>	Lowest Measurable Torque
<b>LVDT</b>	Linear Variable Differential Transformer
<b>Meas</b>	Indices for measured values
<b>NASCAR</b>	National Association for Stock Car Auto Racing
<b>PoC</b>	Proof of concept
<b>PWM</b>	Pulse width modulation
<b>QFD</b>	Quality Function Deployment
<b>RC</b>	Radio controlled
<b>RTD</b>	Resistance temperature detectors
<b>SAE</b>	Society of automotive engineers
<b>SPC</b>	Statistical Process Control
<b>UUT</b>	Unit under test
<b>VG 100</b>	Viscosity grade, i.e. 100 centistokes at 40 °C
<b>VSM</b>	Vehicle Simulation Model

# Symbols

Symbol	Explanation	Unit
<b>A</b>	Bearing Location A - Inner bearing	-
<b>B</b>	Bearing Location B - Outer bearing	-
<b>c<sub>A</sub></b>	Axial stiffness	N/mm
<b>cc</b>	Cubic capacity	L
<b>c<sub>combi</sub></b>	Combined stiffness	N/mm
<b>c<sub>R</sub></b>	Radial stiffness	N/mm
<b>d<sub>tire</sub></b>	Tire diameter	mm
<b>d<sub>flywheel</sub></b>	Diameter of the flywheel	mm
<b>d<sub>frictionwheel</sub></b>	Diameter of the friction wheel	mm
<b>dn</b>	Delta speed	RPM
<b>dn/dt</b>	Derivative of the rotational frequency over time	1/s <sup>2</sup>
<b>f<sub>0</sub></b>	Bearing factor acc. ISO 15312	-
<b>f<sub>1</sub></b>	Bearing factor acc. ISO 15313	-
<b>F<sub>A</sub></b>	Axial load	N, kN, MN
<b>f<sub>crit</sub></b>	Highest excitation frequency	Hz
<b>f<sub>i</sub></b>	Eigenmode #i frequency	Hz
<b>f<sub>max</sub></b>	Max measurement frequency of the speed sensor	Hz
<b>F<sub>R</sub></b>	Radial load	N, kN, MN
<b>f<sub>rotor</sub></b>	Rotor frequency	Hz
<b>F<sub>X</sub></b>	Force in X-Direction	N, kN, MN
<b>F<sub>X,sim</sub></b>	Simulated force in X-Direction	N, kN, MN
<b>F<sub>Y</sub></b>	Force in Y-Direction	N, kN, MN
<b>F<sub>Y,sim</sub></b>	Simulated force in Y-Direction	N, kN, MN
<b>F<sub>Z</sub></b>	Force in Z-Direction	N, kN, MN
<b>F<sub>Z,sim</sub></b>	Simulated force in Z-Direction	N, kN, MN
<b>J</b>	Rotational Inertia	kgm <sup>2</sup>
<b>L<sub>XX</sub></b>	CAD calculated Rotor Inertia around the X-axis	kgm <sup>2</sup>
<b>m</b>	vehicle mass	kg
<b>n</b>	Counting variable	-
<b>n<sub>wheel</sub></b>	Wheel speed	RPM
<b>n<sub>wheel,sim</sub></b>	Simulated wheel speed	RPM
<b>n<sub>i</sub></b>	speed at location i	RPM
<b>n<sub>motor</sub></b>	Motor speed	RPM
<b>P<sub>friction</sub></b>	Total power loss	W, kW, mW
<b>P<sub>1</sub></b>	Combined bearing load	N, kN, MN
<b>T</b>	Torque	Nm, Nmm
<b>T<sub>0</sub></b>	Speed dependent friction torque acc. To Schäffler	Nm, Nmm
<b>T<sub>1</sub></b>	Load dependent friction torque acc. To Schäffler	Nm, Nmm
<b>T<sub>Friction</sub></b>	Total friction torque according to Schäffler	Nm, Nmm
<b>T<sub>UUT1/2</sub></b>	Friction torque of the unit under test #1 or #2	Nm, Nmm
<b>T<sub>max</sub></b>	Maximum friction torque of the UUT	Nm, Nmm
<b>T<sub>motor</sub></b>	Motor torque	Nm, Nmm
<b>v</b>	Kinematic viscosity of the base oil	cS
<b>v<sub>max</sub></b>	Maximum vehicle speed	km/h
<b>v<sub>mean</sub></b>	Average vehicle speed	km/h
<b>ΔT<sub>0</sub></b>	Compensation torque for state model approach	Nm, Nmm
<b>ΔT<sub>1</sub></b>	Compensation torque for state model approach	Nm, Nmm
<b>ω</b>	Rotational frequency	1/s
<b>π</b>	Mathematical constant	-

# 1 Introduction

## 1.1 Motivation

Vehicle performance, reliability, and efficiency are the key factors in modern motorsports to be competitive. Within the last ten years, the margin of victory in the famous Indianapolis 500 race was below 2.15 seconds [1]. Within a given ruleset in a race series, specific measures are taken to ensure equal power/performance at the crankshaft and therefore competitive races. These restrictions create the need to reduce or eliminate even the smallest friction sources, to provide the highest possible power output through the drivetrain to the wheels.

Therefore, it makes sense to locate and characterize friction sources and identify their influence on a given system. According to the 2<sup>nd</sup> law of thermodynamics, all components in a system are subject to create losses. However, some of the effects can be neglected; others are substantial and worth to be modeled and optimized. A typical powertrain layout contains the following main rotating friction sources [2]:

- Bearings
- Gears
- Sealings
- Shafts
- Clutches

These components generate losses by different friction mechanisms. The main mechanisms are:

- body/body contacts (direct contact friction)
- body/fluid contacts (aerodynamic friction, EHD contact)
- internal damping effects (microscopic body/body contacts),

Mechanical contact friction sources are defined by many design parameters, i.e., dimensions, tolerances, surface conditions, lubrication, loads with cross-relations between each other. From an engineering point of view, these sources promise the highest probability to influence the friction in a given system.

Aerodynamic forces are mainly influenced by the overall size and shape of objects at constant reference speed. These factors are mostly limited in powertrain design.

Internal damping effects are based on the mechanical properties of materials. Steel alloys stressed in the elastic range, typically have damping ratios of less than 0.01. This value defines the ratio between the actual damping behavior and the critical damping behavior were the system is considered fully damped. Due to this definition, a value of zero represents an undamped system. That leads to the assumption that internal friction forces can be neglected on parts with negligible deformation.

Last but not least, the absolute amount of friction sources is essential to determine the overall system friction. Equal elements that are used repeatedly have more importance than parts that are only used one or two times in the system.

### **1.2 Target**

Considering the factors in chapter 1.1, one of the most promising driveline components to reduce friction is the wheel bearing assembly of a car. Race teams are allowed to modify this assembly within certain boundaries and the fact that it is present in every car four times makes it even more interesting. Until now, the friction behavior of wheel hubs under load was not yet quantified independently, despite the evidence that the bearing assembly is considered one of the main friction sources [3].

The objective of this thesis is to evaluate a concept that quantifies the performance of a racing wheel hub assembly within a given set of boundary conditions. These conditions can be split up in 3 main categories:

- Design parameters (size of bearings, the pretension of the assembly, type & amount of grease)
- Ambient conditions (Temperature)
- Bearing Loads

The influence of design parameters and ambient conditions can be studied in document [4].

Recognizing that, the mentioned objective can only be achieved if a suitable setup can be found that is able to apply adjustable loads (axial and radial) onto the bearings, allows measuring them and the occurring losses.

The following chapters deal with the evaluation of possible concepts, and the proof of concept (PoC, includes: design, manufacturing, and testing) of the setup with the highest proposed success rate. Furthermore, the following parameters of the test rig should be assessed:

- speed range
- torque measuring range
- the accuracy of the overall system
- repeatability of the overall testing process
- reproducibility of the overall testing process
- estimated testing time per development task
- estimated costs of an industrialized version of the rig

For these parameters, it is now necessary to define representative boundary values. Therefore, a demo bearing must be chosen that meets the three parameters listed below. By selecting a proper test bearing, it can be ensured that the system is able to cover a wide range of units under test.

- wide speed range
- high loads on bearings
- high efficiency in the overall powertrain

A demo UUT that meets all the mentioned criteria is a NASCAR specified wheel hub assembly. The ruleset of the NASCAR sprint cup series allows the race teams to change all design parameters of the bearing, for example:

- size, amount of rollers
- pretension
- type of grease
- pressure angle



**Figure 1: NASCAR specified wheel hub**

The only limitations are the bearing type, which must be a tapered roller bearing and the minimum weight of the assembly, which must be higher than 6,25 pounds [5]. Figure 1 shows a picture of a NASCAR specified wheel hub manufactured by the Timken cooperation, mounted on a reworked NASCAR specified spindle (wheel hub carrier) unit.

## 2 Methodology and Theory

### 2.1 The unit under test description

The parameters in Table 1 are defining the main relevant parameters of a NASCAR Sprint cup vehicle. With the vehicle mass, it is possible to calculate the base load on the bearings in the radial direction. The tire diameter defines the rotational speed of the wheel, where the maximum speed defines the maximum speed of the testing assembly, and the average speed defines the range where the friction should be quantified. Based on these values implicit requirements can be defined, which will be discussed in the following chapters.

**Table 1: NASCAR vehicle specification [5]**

Parameter	Value
<b>Vehicle Mass [m]</b>	3450 pounds (eqv. to 1565 kg)
<b>Tire diameter [<math>d_{tire}</math>]</b>	28 inches (711 mm)
<b>Maximum speed [<math>v_{max}</math>]</b>	Up to 220 mph (eqv to 354 km/h)
<b>Average speed [<math>v_{mean}</math>]</b>	188 – 204 mph (eqv to 302.6 – 328.3 kmh)

#### 2.1.1 Wheel speed distribution

As a first estimation, the average and maximum wheel speeds can be calculated by Equation 1 and the corresponding parameters for the tire diameter and the given speeds. The real wheel speeds depend on the effective tire diameter. This diameter is considered in the simulation in chapter 2.1.2. in order to refine the maximum system speed requirement. The outcome defines the maximum operational speed of the testbed and the essential speeds for the friction evaluation.

$$n_{wheel} = \frac{v_{max}}{d_{tire} * \pi} \quad 1$$

Table 2: NASCAR wheel speed distribution

Speed	Value
Maximum speed	2641.4 RPM
Average speed lower boundary	2257.9 RPM
Average speed upper boundary	2449.6 RPM

### 2.1.2 External bearing loads

In order to quantify the bearing load, it is necessary to implement coordinate systems to all the following considerations. All coordinate systems in this thesis are following the SAE Vehicle Dynamics Terminology J670e. This nomenclature corresponds to the Vehicle DIN 70000 standard with an inverted Z-component and therefore an inverted Y-component. By using the SAE version, the increasing tire contact force during a left-hand corner in the z-direction is positive, as well as the lateral force in the y-direction.

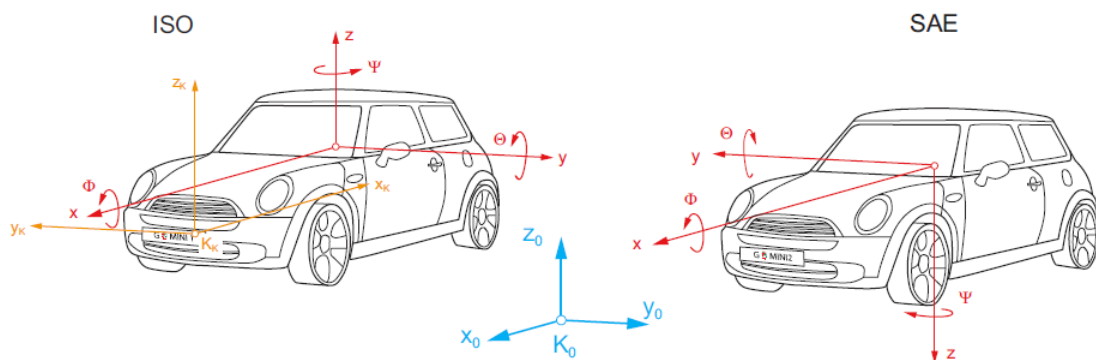
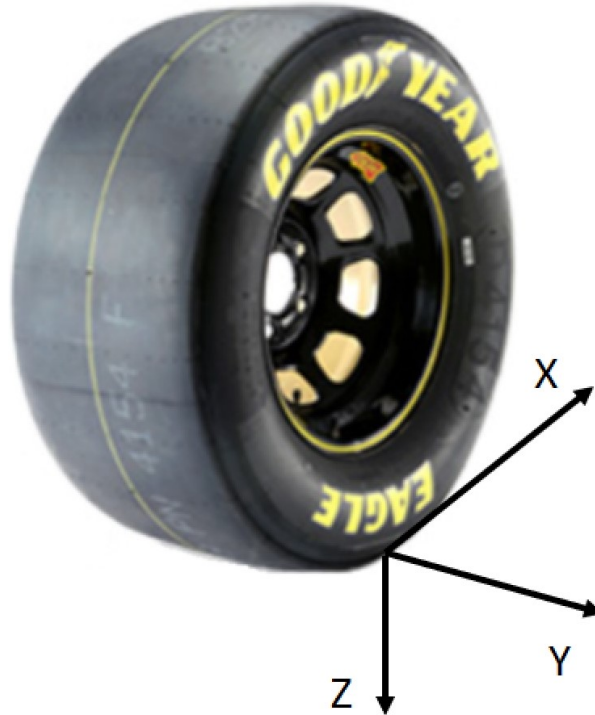


Figure 2: Vehicle coordinate system according to DIN / ISO 70000 and SAE J670e, reproduced from W. Hirschberg [6]

All calculations are based on the front right tire since it's the one with the highest loads during operation. Reason for that is that NASCAR tracks only contain left-hand corners and therefore centrifugal forces result in high loads. Further forces resulting from deceleration are higher than

those occurring during acceleration and deceleration forces acting on the front wheels. By this definition, the front right tire coordinate system can be defined as shown in Figure 3.

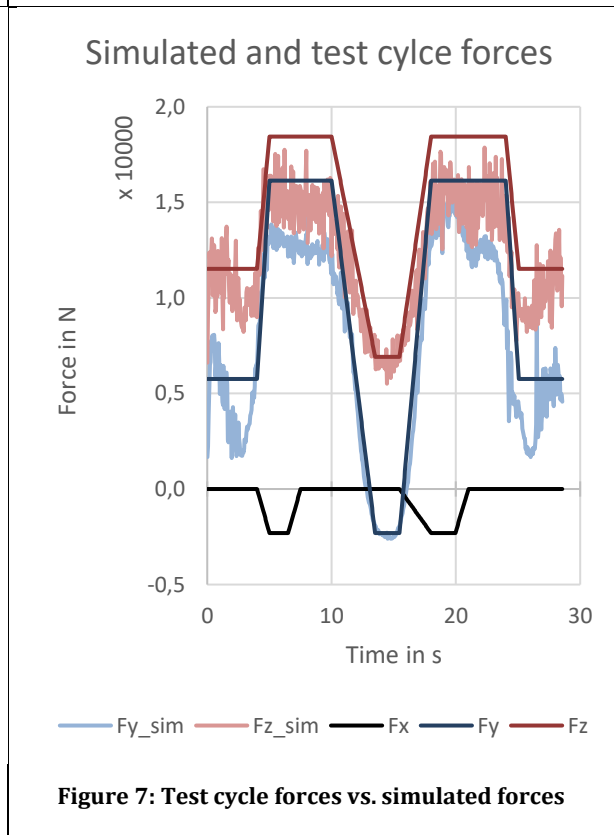
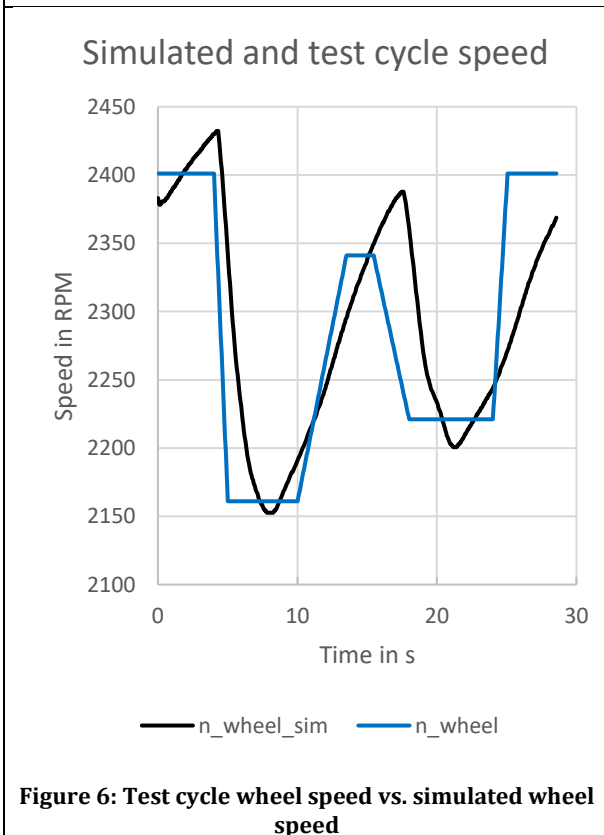
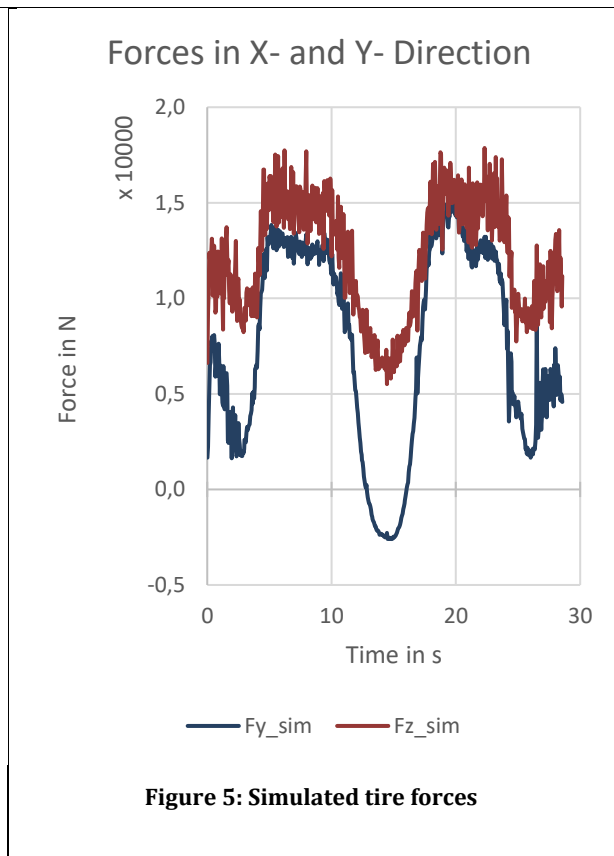
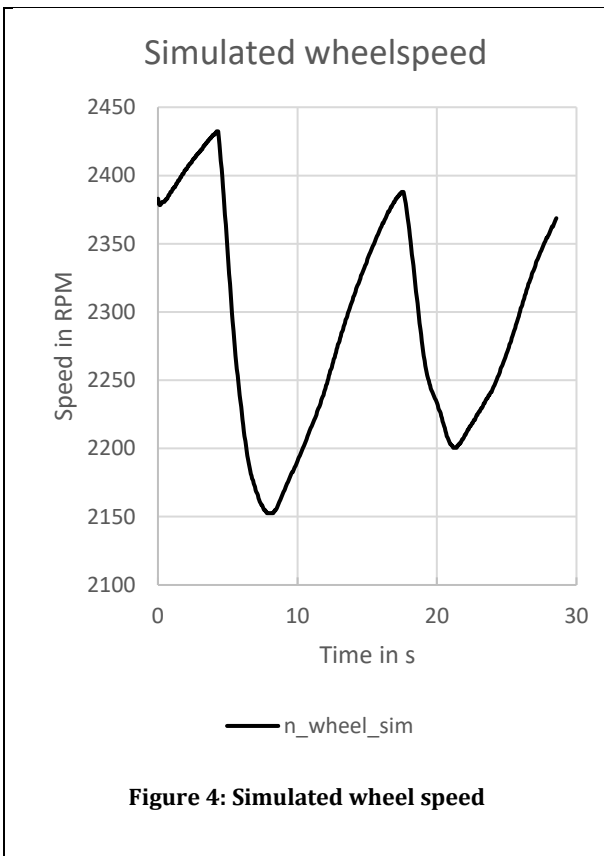


**Figure 3: Tire coordinate system, reproduced from Goodyear[7]**

AVL VSM™ was used to estimate the forces in the tire contact area. Hence this simulation contains sensitive data, owned by the AVL List GmbH, this thesis shows a modified dataset. The author of this thesis is in possession of the original dataset which can be reviewed upon request.

Figure 4 and Figure 5 show the wheel speed and  $F_Y / F_Z$  distribution over a representative NASCAR lap. Figure 5 shows two plateau zones during two highspeed left-hand corners and a low-force zone during the straights for the Z-direction. The Y-force indicates high lateral accelerations during cornering and approximately in the middle of the track a zone without any – or even contrary – steering forces. Since the overall load profile can be divided into repeating sections, the data is simplified by considering an average load during each section. Figure 6 shows the reduced test cycle profile versus the original simulated speed profile. Figure 7 shows the reduced test cycle forces versus the simulated forces. The colors in Figure 6 and Figure 7 are chosen to match the correspondent force direction. Reddish colors indicate forces in the Z-direction, bluish colors in the Y-direction. Figure 7 also includes the longitudinal force on the front right wheel, which is zero during acceleration and around 2300 N in the deceleration zones. The braking system of the vehicle causes this force.

Table 3: Speed and force dataset



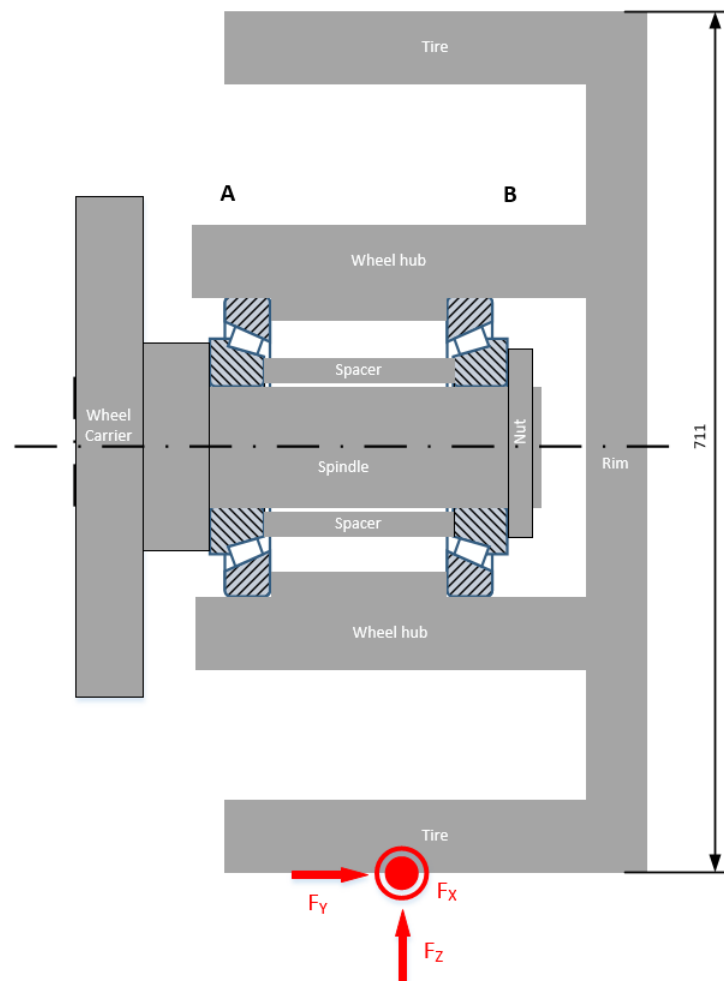


Figure 8: System sketch, original drawing confidential [3]

Figure 8 gives an overview of the location and the direction of the forces in relation to the test object. The mechanical equilibrium enforces the following forces on the bearing arrangement:

- $F_Y$  acts as an axial load on the bearing setup. The system itself creates an absolute force on both bearings. The axial force on bearing A decreases, the force on bearing B increases.
- $F_Z$  and  $F_X$  create radial loads. For all future considerations,  $F_X$  is neglected since the friction torque of the hub during braking as well as the rolling resistance at high speeds is not relevant due to its low magnitude.
- $F_Y$  enforces a bending torque to the system which is calculated by the force times the half wheel diameter.

Therefore, one can abstract the setup with a simple beam arrangement which is described in chapter 2.5 in detail. The simulated wheel speeds indicate that the calculated wheel speeds in chapter 2.1. overestimate the wheel speeds. For all future considerations, the speed range above 2600 RPM is considered as an over-speed capability

### 2.1.3 Test rig requirements

The UUT parameters discussed in the last chapters define the requirements for the test rig. The main criteria are to load the bearing arrangement with the loads defined in section 2.1.2 and to measure the torque loss in the speed ranges described in this chapter. Table 4 sums up the requirements.

**Table 4: Test rig requirements**

Parameter	Value
<b>Speed range</b>	Up to 2600 RPM
<b>Z-Force</b>	Up to 18,5 kN
<b>Y-Force</b>	Up to 15 kN
<b>Force application and measuring accuracy</b>	< 5 %
<b>Estimated friction value</b>	Up to 2000 Nmm
<b>Data measurement</b>	continuously
<b>Relative friction measurement</b>	Yes
<b>Absolute friction measurement</b>	Yes
<b>Repeatability</b>	<10 Nmm
<b>Reproducibility</b>	<10 Nmm
<b>Accuracy</b>	<5 Nmm
<b>Acquisition cost</b>	Less than 10 k€

The speed range defines the required maximum operating speed to cover the same speed range as the real vehicle. The forces are based on the calculations in chapter 2.1.2 to apply equivalent loads on the bearing. The accuracy of the application mechanism should be in the range of less than 5 % percent to ensure equal testing conditions during different test setups. The expected maximum torque defines the required acceleration torque of the drive motor. A continuous data measurement is required to analyze all data within one single toolchain comfortably. Relative friction measurement describes the ability to compare a unit under test against another unit under test, where the absolute friction measurement evaluates the difference between a specimen and a fixed reference point. Repeatability describes the variation that occurs when measurements are made under identical conditions. Reproducibility describes the variation that occurs when

measurements are made under similar, but not exactly the same conditions, like a different operator or a specimen with the same specification but a different serial number. The accuracy describes the overall expected deviation between the measured value and the real value. A cost-efficient setup is critical to offer competitive testing prices. Therefore a target value for the production cost of 10 k€ was set.

Since this table contains explicit and implicit requirements, it is necessary to categorize & structure the entries according to their importance. This structure is correlating to a QFD technique called “House of Quality” (HoQ) and used throughout this thesis. In addition to the values of the parameters, an “importance” parameter is used to create the relative weight (relative importance) of each requirement. Table 5 shows the contents from Table 4 translated to the HoQ standard.

**Table 5: Requirement Importance & Rating**

<i>Row #</i>	<i>Requirements (Explicit and Implicit)</i>	<i>Importance</i>	<i>Relative Weight</i>	<i>Weight Chart</i>
1	Relative friction measurement	9	14 %	
2	Absolute friction measurement	5	8 %	
3	Nominal speed range capability (<= 2600 RPM)	9	14 %	
4	Overspeed capability (2700 - 3000 RPM)	2	3 %	
5	Full measurement range (up to 2000 Nmm)	9	14 %	
6	Repeatability <10 Nmm	4	6 %	
7	Reproducibility <10 Nmm	3	5 %	
8	Accuracy	5	8 %	
9	Load application system	9	14 %	
10	Wide range of UUTs	3	5 %	
11	Cost efficiency	5	5 %	

The importance is based on internal knowledge to complement the AVL testing portfolio in the best possible way. With this rating, it is now possible to find technical solutions and rate them according to their potential to fulfill the requirements.

## 2.2 Efficiency measurement methods

By definition, mechanical efficiency is the ratio of the measured performance to the performance of an ideal component or machine [8]. Therefore, a system that can measure efficiency must be able to quantify the performance of the ideal and the real system. In the case of a bearing, the

performance indicator is the difference in torque on the system with and without the component, commonly known as torque loss.

If the definition of performance is extended to the mechanical power a system can convert, the measurement of the rotational speed is also necessary.

Another challenge achieving the given requirements is to apply forces to the UUT without creating additional friction sources, which is, by the nature of physical transport processes, impossible, since every mechanical solution will act as an additional and unknown friction source. Therefore, it has to be investigated if a configuration can be found where this effect can either be neglected or calculated.

### 2.2.1 Torque measurement

According to [9], torque measurement methods can be divided into direct and indirect measurement methods, where Figure 9 gives an overview of the discussed methods. Direct methods have the benefit that the signal can be recorded with high frequency since the measurement device is placed within the driveline. Indirect methods use a transfer signal such as force, current or speed to calculate the torque.

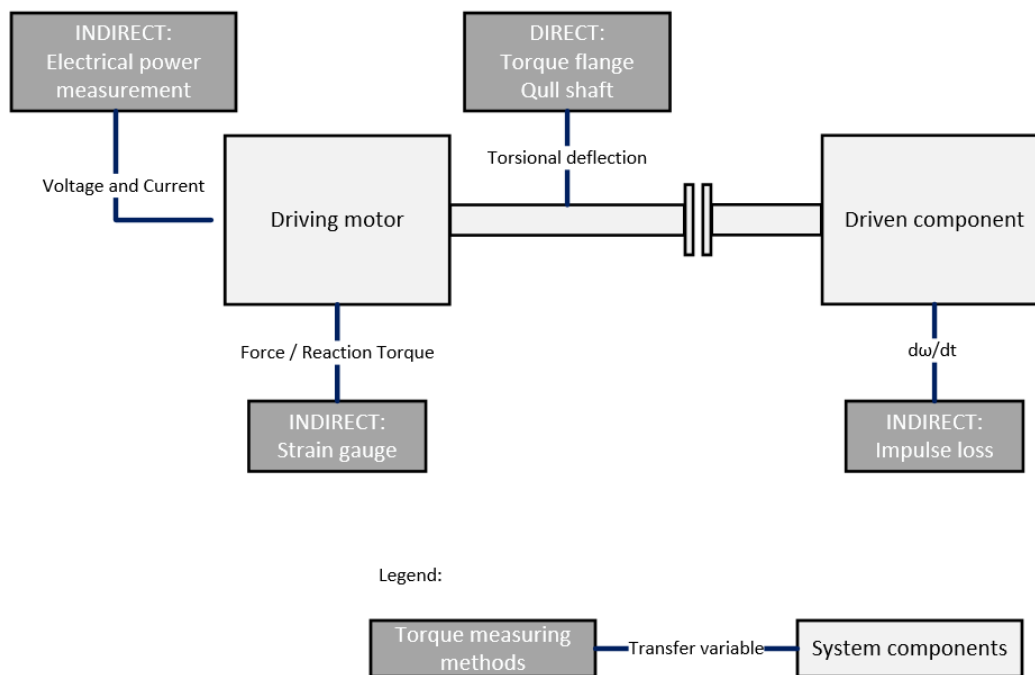


Figure 9: Overview of the discussed torque measuring methods

In general, torque measurement methods are based on various physical concepts. Probably the most common method is the measurement of a torsional deflection within a rotating component. This deflection is picked up by a strain gauge which converts the change in length into an electrical signal by measuring the resistance of the sensor. This signal compared to a calibrated reference scale creates the starting point for a torque calculation. This principle is used with HBM torque measuring flanges. One downside of these sensors is the fact that the measuring range is limited and cannot be adjusted since the stress on the section where the strain gauge is applied is limited by the mechanical properties of the sensor shaft.

Another method directly measures the angular deflection with two marker discs and a quill shaft in between. If the torsional stiffness of the shaft is known, the torque is calculated by picking up the value of the deflection between the reference and a marker disc. This method is also limited by the mechanical properties of the measuring shaft. If the shaft has a low torsional stiffness, the accuracy is high, but it probably cannot withstand the high acceleration/deceleration torque. If the torsional stiffness is high, the system does not provide the required sensitivity.

Reaction torque measurement methods measure the force that is required to counteract the torque in the rotating assembly. This force is picked up by a strain gauge and then multiplied by the length of the reaction beam.

The indirect measurement of the torque loss via the loss of momentum represents another method of measurement. The conservation of momentum is the basis of this principle. Equations 2-4 show the formulation that is relevant in this context.

$$\vec{T} = J * \dot{\omega} \tag{2}$$

$$\dot{\omega} = \frac{d\omega}{dt} = 2 * \pi * \frac{dn}{dt} \tag{3}$$

$$\vec{T} = 2 * J * \pi * \frac{dn}{dt} \tag{4}$$

, where  $\omega$  represents the angular frequency, T the torque, J the rotational inertia and n the rotational speed of the system.

The extension of Table 5 to a full HoQ is necessary to compare the three systems regarding their ability to fulfill the given requirements. Therefore, the functional capability of a method and the requirement are put into relation. Table 6 gives an overview of the possible rating scores within a standardized HoQ. The scores are based on AVL internal know-how.

**Table 6: Relationship scores for a standardized HoQ**

Relationship / Ability to fulfill the requirement		
Strong	9	●
Moderate	3	○
Weak	1	▽

This score is multiplied by each relative weight and then summed up for each functional capability. The outcome is a numeric value that describes the probability for each method to fulfill the broadest possible range of requirements. The relative value of this score is used as an indicator to compare the different methods against each other.

Table 7 shows a complete house of quality (HoQ) with the final result section at the bottom end. The outcome of this graph indicates that the torque measurement for this type of application should be done with the impulse loss method.

Table 7: HoQ for torque measurement methods

Row #	Weight Chart	Relative Weight	Importance	Maximum Relationship	Requirements (Explicit and Implicit)	DIRECT: Torque Flange	DIRECT: Quill Shaft	INDIRECT: Electrical Power Measurement	INDIRECT: Strain Gauge / Reaction Torque	INDIRECT: Impulse Loss
1		14%	9	9	Relative friction measurement	○	○	○	●	●
2		8%	5	9	Absolute friction measurement	○	○	▽	▽	●
3		14%	9	9	Nominal speed range capability (<2600 RPM)	●	●	●	●	●
4		3%	2	9	Overspeed capability (2600 - 3000 RPM)	●	●	●	●	●
5		14%	9	9	Full measurement range (10 - 1000 Nmm)	▽	○	▽	○	●
6		6%	4	9	Repeatability <10 Nmm	○	○	○	●	●
7		5%	3	9	Reproducibility <10 Nmm	○	○	▽	●	●
8		8%	5	9	Accuracy	●	●	○	●	●
11		5%	5	9	Cost efficiency	▽	▽	●	○	●
<b>Max Relationship</b>						9	9	9	9	9
<b>Technical Importance Rating</b>						347.86	376.43	314.84	522.94	702.14
<b>Relative Weight</b>						15%	17%	14%	23%	31%
<b>Weight Chart</b>										

### 2.2.2 Speed measurement

Rotational speed is defined by the amount of time required to cover a rotational distance (e.g., angle) [10]. If not otherwise stated, the angle equals one full rotation. Typical units are RPM (revolutions per minute) and [1/s] (revolutions per second). Per definition, speed is a time-based value and therefore an accurate time measurement device is needed to come to a highly accurate result. Devices that can measure rotational speed are called speedometers. Typical working principles are:

- Tacho generators
- Impulse speedometer
- Optical encoders
- Inductive proximity sensors
- Stroboscopic tachometer

Tacho generators use the principle of an electrical generator, where the output voltage or power is correspondent to the rotational speed of a shaft. Therefore, a direct connection to the rotating system is required which would create an additional friction source in our application.

Stroboscopic tachometer technology uses the inertia of the human eye. It is widely used to check systems running at a fixed speed.

The other methods use a counter signal where the time between two marks is measured. They only diverge in the physical method of how the marks are counted. The optical encoders have the benefit of being genuinely contactless, compared to the other speedometers where magnetic fields or field changes are the triggers for the sensor pick-up.

To quantify the best suiting method, again the HoQ technique is used, where Table 8 shows the result. The impulse speedometer, inductive proximity sensors, and optical encoders have almost the same technical ability to fulfill the requirements. Since the optical speed sensors are insensitive against the physical distance to the rotor, the proposed application uses this method.

**Table 8: HoQ for speed measurement methods**

Row #	Weight Chart	Relative Weight	Importance	Maximum Relationship	Requirements (Explicit and Implicit)	Functional Capabilities	Tacho generator	Impulse speedometer	Optical Encoder	Inductive proximity sensor	Stroboscopic tachometer
3		14%	9	9	Nominal speed range capability (<2600 RPM)		●	●	●	●	●
4		3%	2	9	Overspeed capability (2600 - 3000 RPM)		○	○	●	●	○
8		8%	5	9	Accuracy		○	●	●	●	▽
9		14%	9	9	Load application system		▽	●	●	●	○
10		5%	3	9	Wide range of UUTs		○	○	●	○	●
11		5%	5	9	Cost efficiency		○	○	▽	○	●
<b>Max Relationship</b>							9	9	9	9	9
<b>Technical Importance Rating</b>							205.48	367.38	405	386.43	276.75
<b>Relative Weight</b>							13%	22%	25%	24%	17%
<b>Weight Chart</b>											

### 2.2.3 Force measurement

According to [11], the main force measurement methods can be classified as per Table 9.

**Table 9: Guide to force transducer types and characteristics[11]**

<b>Device type</b>	<b>Typical range of rated capacities</b>	<b>Typical uncertainty % of reading</b>	<b>Typical temperature sensitivity % of reading per °C</b>
Strain gauge load cells Thin film gauges Foil gauges	0.01 N to 1 MN	0.02 to 1	0.01 (-40 °C to +80 °C)
Piezoelectric crystal	1.5 mN to 120 MN	0.3 to 1	0.02 (-190 °C to +200 °C)
Hydraulic	500 N to 5 MN	0.25 to 5	0.05 (+5 °C to +40 °C)
Pneumatic	10 N to 500 kN	0.1 to 2	0.05 (+5 °C to +40 °C)
LVDT, capacitive, tuning-fork, vibrating wire	10 mN to 1 MN	0.02 to 2	0.02 (-40 °C to +80 °C)
Magnetostrictive	2 kN to 50 MN	0.5 to 2	0.04 (-40 °C to +80 °C)

Strain gauge-based methods use a deflection that is converted into a change in the electrical resistance of a conductor. If the strain gauge is mounted inside a housing with standardized connection interfaces, it is commonly named load cell.

Piezoelectric crystals induce a voltage in a closed electrical circuit corresponding to their mechanical deflection. Since the value of this voltage depends on the rate of change during the deflection, it is highly accurate for measuring fast changes in forces. A change of force with a frequency of less than 1 Hz is considered not suitable for piezoelectric crystals. [2]

Hydraulic and Pneumatic force measurement methods are based on a pressure measurement inside a circuit. By multiplying the pressure with a given reference surface (i.e., hydraulic cylinder piston cross-section), a force can be calculated.

LVDT, capacitive, tuning fork and vibrating wire methods are based on the change of a physical value that describes the sensor system. In the case of LVDT and capacitive sensors the electrical capacity of the sensor changes under load. The tuning fork and vibrating wire methods are based on the change of the resonance frequency of a loaded wire under load.

The magnetostrictive measurement sensors pick up the change of the magnetic field during a deflection with measurement coils.

Again, the house of quality is used to assess the best suitable method. Strain gauges with signal conditioning units are preferable to other solutions, due to the practicality and the cost-effectiveness.

**Table 10: HoQ for force measurement methods**

Row #	Weight Chart	Relative Weight	Importance	Maximum Relationship	Requirements (Explicit and Implicit)	Strain gauge	Piezoelectric crystal	Hydraulic	Pneumatic	Tuning fork	Magnetostrictive
8		8%	5	9	Accuracy	●	○	●	○	●	○
9		14%	9	9	Load application system	●	○	●	○	▽	○
10		5%	3	9	Wide range of UUTs	●	○	○	●	▽	○
11		5%	5	9	Cost efficiency	●	▽	○	●	▽	▽
<b>Max Relationship</b>						9	3	9	9	9	3
<b>Technical Importance Rating</b>						287.86	85.952	229.29	154.52	95.476	85.952
<b>Relative Weight</b>						31%	9%	24%	16%	10%	9%
<b>Weight Chart</b>											

### 2.3 Evaluation of methods

Based on the results from chapter 2.2, the combination of the following three methods is the one with the highest expectation to fulfill the given requirements:

- Strain gauges to measure the forces
- An optical encoder to measure the speed
- The impulse loss method to measure torque



a (PoC) basis. The solution with the mirrored UUT arrangement is described in chapter 2.4. V1 PoC is built to create a baseline for all future force dependent measurements.

Table 12: System HoQ

Row #	Weight Chart	Relative Weight	Importance	Requirements (Explicit and Implicit)	Functional Capabilities	Testing inside a Powertrain Test Cell	Testing with one drive motor and strain gauge	existing Spin rig without force replica, with / without vacuum chamber	Horizontal spin rig, old drive motor, old friction wheel	NEW SETUP - Horizontal spin rig, new drive motor, new friction wheel, mirroring of setup & force actuation
1		14%	9	Relative friction measurement		▽	○	●	●	●
2		8%	5	Absolute friction measurement		▽	▽	○	○	○
3		14%	9	Nominal speed range capability (<2600 RPM)		●	●	○	○	●
4		3%	2	Overspeed capability (2600 - 3000 RPM)		●	●	○	○	●
5		14%	9	Full measurement range (10 - 1000 Nmm)		○	○	▽	▽	●
6		6%	4	Repeatability <10 Nmm		▽	○	●	○	○
7		5%	3	Reproducibility <10 Nmm		▽	▽	●	○	○
8		8%	5	Accuracy		▽	▽	●	●	●
9		14%	9	Load application system		○	●	▽	▽	●
10		5%	3	Wide range of UUTs		●	○	▽	○	○
11		5%	5	Cost efficiency		▽	○	●	○	▽
<b>Technical Importance Rating</b>						331.98	440.4	454.52	367.38	690.71
<b>Relative Weight</b>						15%	19%	20%	16%	30%
<b>Weight Chart</b>										

## 2.4 Design parameters

The following concept results from the findings in chapter 2.3. It is proposed to use a back-to-back arrangement of 2 equivalent UUT's and mount this rotating assembly to a mirrored rigid frame construction. One of the two frames acts as a locating bearing, the other one as a movable bearing, where forces can be applied. Figure 10 contains a functional sketch of the system

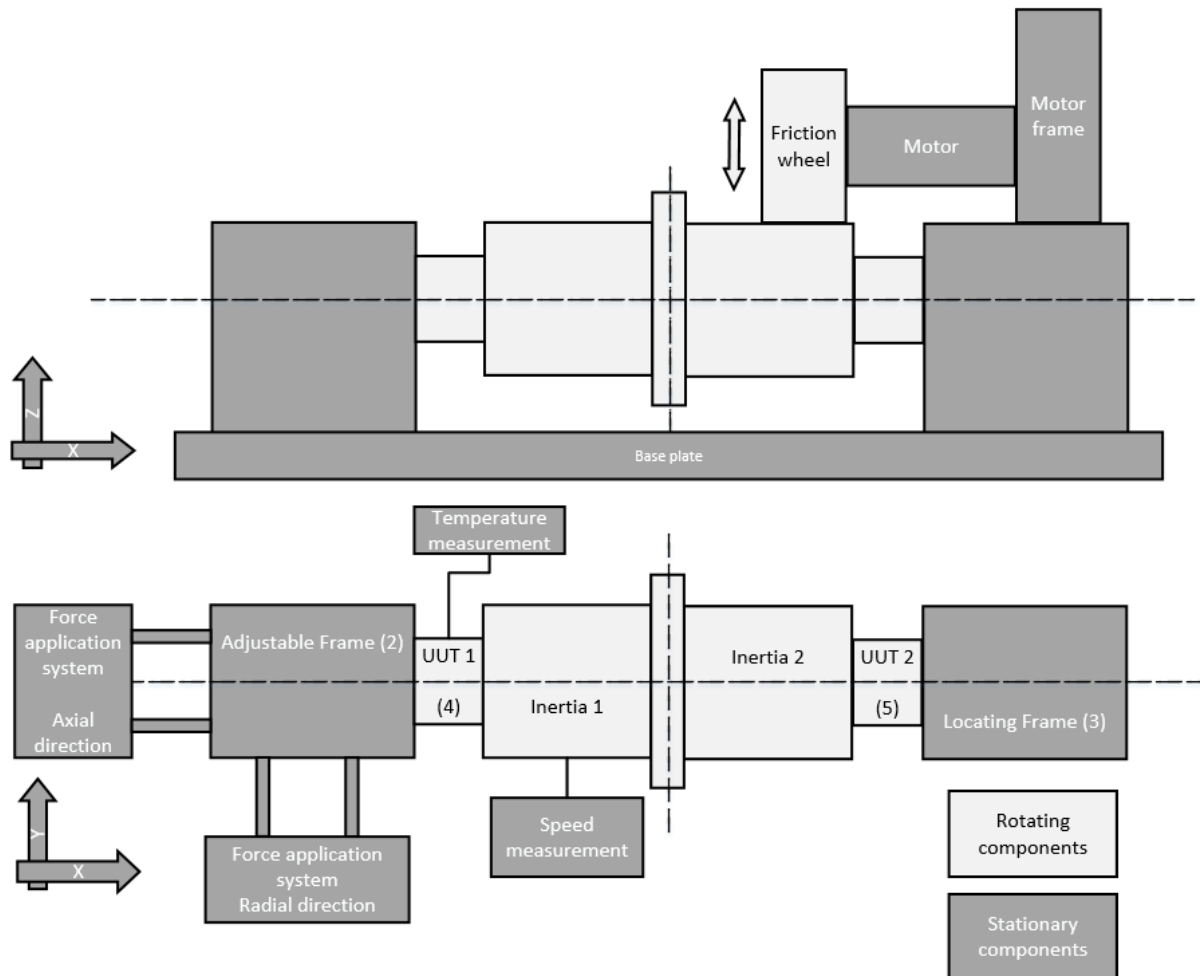


Figure 10: Conceptual overview

The Frames (2 & 3) are mounted to the base plate. Both UUT's (4 & 5) are mounted between the two frames and connected by two equally sized inertias. The force application system & force measurement sensors are used to pre-tension the UUT's against each other in axial & radial direction. A drive motor accelerates the system to the maximum operating speed. This motor can be disengaged to avoid any friction influence by the motor during the run-out process. The non-driven system is now decelerating with a natural gradient (impulse loss). Due to the equations of

motion & energy, two factors influence impulse loss: The mechanical friction torque and aerodynamic losses. In low-speed applications, the aerodynamic losses are negligible compared to the friction losses [4]. For tests with high rotational speeds or for absolute torque measurement, a vacuum chamber is placed over the entire system in order to minimize the influence of the aerodynamic effects, or the aerodynamic losses are subtracted from known measurements. Therefore, the change of speed over time is correlating to the friction torque created by the 2 UUT's.

$$T_{UUT1} = T_{UUT2} = \frac{J * \dot{\omega}}{2} \quad 5$$

based on Equation 2

$$T_{UUT} = \frac{J}{2} * \frac{\pi}{30} * \frac{dn}{dt} = J * \frac{\pi}{60} * \frac{dn}{dt} \quad 7$$

based on Equation 4

Since the inertia of the system can be calculated after designing the system, the only factor to be measured is the speed of the system over time, as described in chapter 2.2., temperature sensors are used to monitor the inner spindle temperature, to gain more knowledge of the settings and circumstances.

According to Equation 7, the accuracy depends on the system speed and the inertia. The estimated deceleration time can be calculated with an estimated maximum friction torque and the target system inertia.

$$\Delta t = \frac{J * \pi * \Delta n}{60 * T_{UUT}} = 40,9 \text{ s} \quad 7$$

based on Equation 4

Calculated with:

$$J = 0,6 \text{ kgm}^2$$

Estimated target inertia

$$dn = 2600 \text{ RPM}$$

Maximum delta speed

$$T_{UUT} = 2 \text{ Nm}$$

Estimated combined UUT torque (for two UUTs)

The estimated deceleration time is the critical indicator of the physical accuracy of the test setup. If this run out time is too short, it cannot be ensured that all resonance effects and non-linearities are visible in the results, since the averaged calculation of the derivative delays logging frequency to a maximum of 1000 Hz within the measurement chain. With a maximum logging frequency of

1000 Hz and an expected run-out time of 30 seconds, one will get 30.000 measurement points. Decelerating from the maximum over-speed capability of 3000 RPM this results in a resolution of 10 measurement points per 1 RPM speed decrease, which is considered as a sufficient value to visualize non-linear effects like resonance fluctuations directly. Therefore, all measurements within this thesis are based on the raw data. If required, a data point reduction method can be found in [4].

Another boundary for the design is the existing base plate with a length of 700 mm and a width of 500 mm. The frame for the wheel hub assembly as well as the frame for the force application systems is required to fit on this given space.

## 2.5 Friction torque estimation

### 2.5.1 Required torque estimation

According to [12], the primary sources of friction and the corresponding influencing factors are shown in Table 13. Schäffler provides a guideline to calculate the friction torque which is used in the following calculation, where it has to be mentioned that other models are available as well. A comparison of the most common methods regarding their quality is discussed by [4].

**Table 13: Friction components & influencing parameters**

Friction component	Influencing Parameter
Rolling friction	Size of the load
Sliding friction of the rolling elements Sliding friction of the cage	Size and direction of the load Speed and lubrication state break-in condition
Fluid friction (flow resistance)	Type and speed Type, quantity and operating viscosity of the lubricant
seal friction	Type and preload of the seal

According to Schäffler, the above-mentioned friction components can be assigned into two different categories: speed and load dependent. The overall friction torque is the sum of those components. In the following calculation, the speed dependent component is described by the variable  $T_0$  and the load dependent component by  $T_1$ . The friction power is calculated by multiplying the total torque  $T_{Friction}$  with the angular velocity of the rotor. The factor 2 considers the two bearings in the UUT.

$$T_{Friction} = (T_0 + T_1) \quad 8$$

$$P_{Friction} = T_{Friction} * \frac{\pi * n}{30} \quad 9$$

For  $T_0$ , Schäffler distinguishes between a speed-viscosity factor below and above 2000. The difference in the empiric formulas can be found in the influence of the kinematic viscosity of the lubricant. Equation 10 shows the version of the formula for a factor of  $v * n$  greater than 2000, where  $f_0$  is an empirical bearing factor according to ISO 15312,  $v$  the kinematic viscosity of the lubricating oil,  $n$  the system speed and  $d_M$  is the average bearing diameter. The bearing factors are valid for broken-in bearings with evenly distributed lubricant and can be found in tables or graphs. The values for  $f_0$  can be two to five times higher before the break-in procedure.

$$T_0 = f_0 * (v * n)^{\frac{2}{3}} * d_M^3 * 10^{-7} \quad 10$$

$$T_1 = f_1 * P_1 * d_M \quad 11$$

$$P_1 = 2 * Y * F_a \text{ or } P_1 = F_r \quad 12$$

The description of a typical unit under test bearing is necessary to calculate the estimated friction torque. Since the actual dimensions of a NASCAR specified wheel hub including its bearings is the core know-how of a few bearing manufacturers it is kept secret; there is no data for the actual bearing available. Therefore, a bearing similar to the used ones is chosen from the Schäffler bearing catalog in order to perform the estimation. Figure 11 gives an overview of the dimension locations described in Table 14.

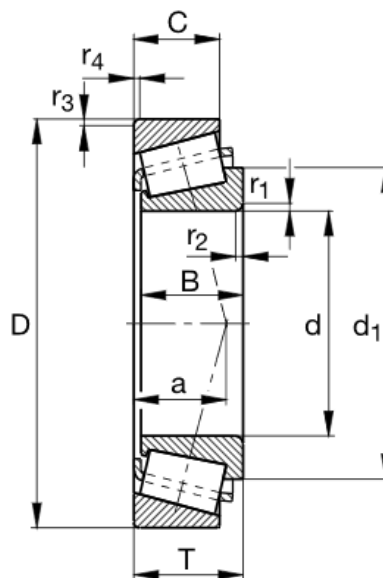


Figure 11: Main bearing dimensions, reproduced from [12]

**Table 14: Reference bearing dimensions and characteristics**

<b>Representative bearing type:</b>		<b>30208</b>
<b>d</b>		40 mm
<b>D</b>		80 mm
<b>T</b>		20 mm
<b>a</b>		17 mm
<b>B</b>		18 mm
<b>C</b>		16 mm
<b>Y</b>		1.8
<b>d<sub>m</sub></b>		60 mm
<b>f<sub>0</sub></b>		3
<b>f<sub>1</sub></b>		0.0004

The calculation of  $T_1$  is based on the type of the used bearing. Equation 11 outlines the case of a tapered roller bearing, where  $f_1$  is a factor similar to  $f_0$  and  $P_1$  is the combined bearing load. Since the rig should be used for multiple configurations and types of UUTs, if applicable, the highest values for the bearing factors are used in this calculation. For the reference bearing the value for  $f_1$  is defined as 0,0004 and for  $f_0$  the value is 3. For Y a value of 1.8 is given. For the kinematic viscosity of the base oil, ISO VG 100 is recommended by the bearing manufacturer [13]. The UUT uses a pretensioned O-arrangement with an unknown pretension force. This force can be estimated later in the results section, when a test without any force is done. In theory, any friction torque that is exceeding  $T_0$  is created by the inner forces of the bearing. To estimate a friction torque, it is assumed, that the criteria  $P_1 = F_r$  is valid for the given UUT specification. The results for  $T_0, T_1, T_{Friction}$  and  $P_{Friction}$  are shown below, for the case of a broken-in UUT as well as for a new or re-greased unit.

**Table 15: Results friction torque estimation**

	<b>Broken-In</b>	<b>New</b>
$T_0$	221 Nmm	1108 Nmm
$T_1$	432 Nmm	432 Nmm
$T_{Friction\_UUT}$	1307 Nmm	3080 Nmm
$P_{Friction\_UUT}$	273.8 W	645.7 W

The total torque of two broken-in bearings is below the assumption of 2 Nm in chapter 2.4. Based on this result, the estimated deceleration time in chapter 2.4 can be recalculated with Equation 7

to 62,5 seconds. Based on this calculation the system boundary of 2 Nm for the maximum friction torque is valid.

$$\Delta t = \frac{J * \pi * \Delta n}{60 * T_{UUT}} = 62,5 \text{ s} \quad 7-2$$

Calculated with:	$J = 0,6 \text{ kgm}^2$	Estimated target design inertia
	$dn = 2600 \text{ RPM}$	Maximum delta speed
	$T_{UUT} = 1307 \text{ Nmm}$	Calculated combined UUT torque (for two UUTs)

Further calculations on the estimated torque are done in chapter 4. With the combination of dedicated tests, it is possible to refine the model from Schäffler to meet the given set of UUTs.

Further attention should be given to the split between  $T_0$  and  $T_1$ . In both cases, the torque induced by the applied forces,  $T_1$  is constant, however in the case of the broken-in bearings, the values for the speed dependent torque  $T_0$  are significantly depending on the kinematic viscosity and on the empiric value  $f_0$ . To get an insight into this relation it is necessary to understand the tribological mechanisms in a (tapered) roller bearing.

### 2.5.2 Tribology in rolling bearings

Due to the uncertainty in the calculation parameters for  $T_0$ , it is worth to pay closer attention to the concept of tribology in rolling bearings. According to Hung Nguyen-Schäfer[14] and Piet M. Lugt[15], EHD friction inside a roller bearing heavily depends on the grease and basis oil properties, which can also be seen in the nonlinear factor of  $v^{2/3}$  in the Schäffler formula.

As an introduction to this topic, it is necessary to answer the question, why bearings need to be lubricated at all. In theory, a roller gets in contact with the inner and outer race without any sliding. In this theoretical case, there would be no need for a lubricant. However, due to the flattening of the roller and the raceway under pressure and due to the kinematics of the bearing slip will occur.

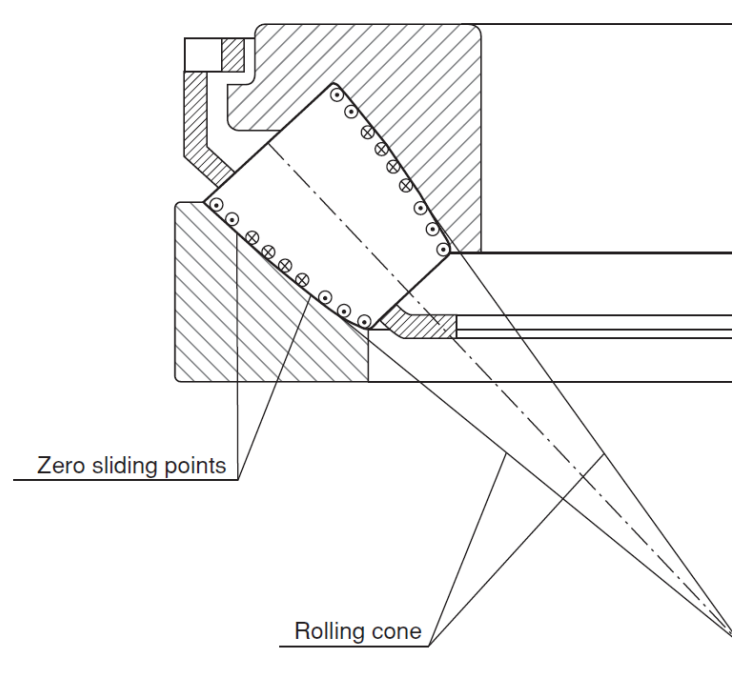


**Figure 12: Slip in a spherical roller thrust bearing. Reproduced from Piet M. Lugt [15]**

The sliding motion leads to high contact forces combined with a relative movement between two surfaces which immediately creates heat. The presence of a lubricant prevents the direct contact of the two surfaces and absorbs the shear stress into the fluid.

First, it has to be mentioned, that in a grease-lubricated bearing, not the grease itself is responsible for the lubrication, but the bound oil inside the grease is. Up to 80 % of the grease consists of base oil; the rest consists of a thickener which is used as a bonding matrix for the oil and additives. Based on this concept it is possible to understand, that the lubrication can be split up into two main phases: The churning phase and the bleeding phase.

The churning phase (or break-in phase) is characterized by grease flowing next to the running tracks, and a part of the grease is distributed inside the bearing elements (under the cage or in the cage pockets). This effect leads to high friction torques because of the high “viscosity” of the grease itself. Followed by a sudden increase of temperature, the grease gets swept out of all the running tracks and inside of the bearing. Once the running tracks are getting cleaner, the temperature begins to decrease or to stabilize. This behavior indicates the end of the churning phase, which can take from several hours up to one day, depending on the inner design of the bearing and the type of grease and base oil. During the churning phase, the contact between the rollers and the running tracks is entirely flooded with oil & remaining grease components.

The bleeding phase is characterized by a stable temperature at defined running speeds. The lubrication mechanism during this phase is either described by bleeding of the surrounding grease or by the breakdown of the thickener structure in the contacts. The bleeding concept is considered as the primary mechanism for lubrication in roller bearings. Due to the minimal amount of oil and grease in the contact area, the friction torque is significantly reduced compared to the churning phase. Studies show that the bleeding properties of grease have an essential impact on friction behavior during the churning and the bleeding phase. It was also proved, that roller bearings require greases with higher bleeding rates compared to ball bearings. According to Piet M. Lugt, there is evidence, that the central bleeding in tapered roller bearings occurs from grease located under the cage bar.

The primary feed mechanisms in the bleeding phase are described as either feed by oil bleeding, bleeding due to shear, capillary forces and centrifugal forces which drive the lubricant flow. On the other hand, the primary loss mechanisms are side flow induced by pressure; centrifugal forces induced side flow, evaporation and cage scrapping. According to the literature, this behavior can be different in the case of a rotating outer ring. A fully broken-in bearing shows a film thickness in the contact area of approximately 70 % compared to the full thickness right after churning. The main effect for the thinning is the Hertzian pressure and therefore the corresponding side flow.

As a recommendation, approximately 30 % of the available air space inside a tapered roller bearing should be filled with grease, since too much grease will lead to excessive churning and therefore to high friction levels and too little grease filling provides no basis for the replenishment of oil at the edge of the running track. According to Piet M. Lugt, a small variation in the grease amount can lead to significant changes in friction behavior. Considering the results from Chapter 2.5.1, this has a highly significant impact on the total friction torque.

Due to the exponential decrease in viscosity over temperature, it is also essential to investigate the thermal behavior of a bearing set. As described above, the final operating temperature is dependent on the filling, the speed and the oil type used.

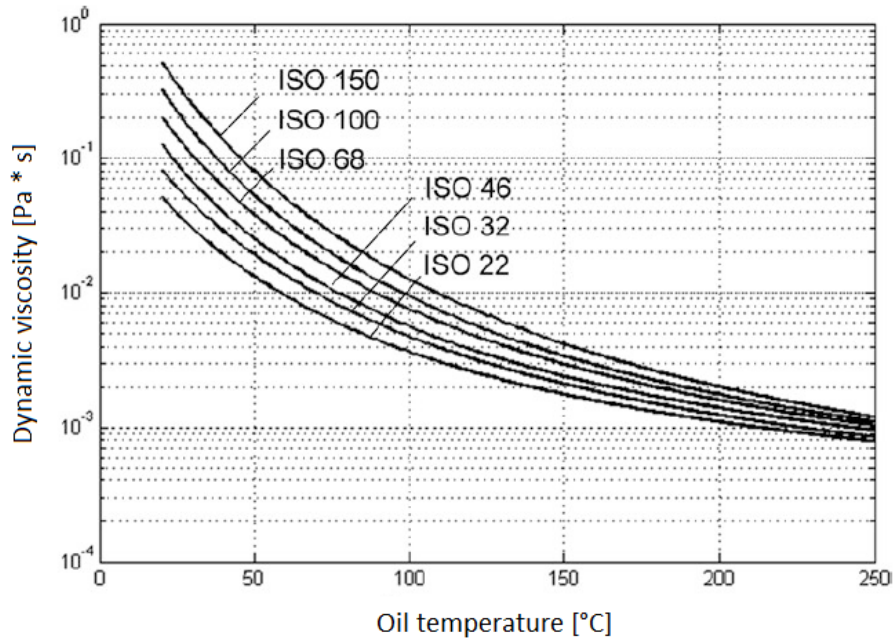


Figure 13: Viscosity of ISO classes over temperature, reproduced from Hung Nguyen-Schäfer [14]

Also, in the application of a car wheel hub, there are external heating sources like the brake disk and caliper close to the bearing. Without the presence of external sources, it can be stated, that a bearing creates the least amount of friction when it runs at cooler temperatures compared to an equivalent bearing operated with higher self-induced temperatures [14].

All the mentioned models and values are stated for bearings with a rotating inner ring. Fewer studies are done on settings with rotating outer rings. Despite that, there are some aspects known that influence the mechanisms described before.

One observed mechanism is the presence of the higher centrifugal force on the outer ring which forces more oil (in the bleeding phase) and grease (in the churning phase) into the raceways, which leads to higher friction values and faster grease degradation. The degradation of the grease lifetime is also accelerated by the higher centrifugal forces of the rollers against the outer race. All the findings in this chapter underline the importance of the high measurement accuracy of the system. All following design considerations should be made under this maxim.

### 3 Proof of concept - Layout

The mechanical design of the rig was executed under the constraints defined in chapter 2 within a system design process. The main task of this process is to ensure a structured approach to master the complex engineering task by splitting the entire product into sub-systems. To apply this logic to the given testing task it is necessary to develop the following sub-systems:

- Mechanical components
- Drive Motor incl. decoupling mechanism & controls
- Data acquisition system
- Sensor definition

The next pages provide an outlook on the detailed work done to design each system with the utmost care. Within each section, the state-of-the-art engineering tools were used to validate the assumptions from the systemic approach during the requirement engineering phase and to avoid potential issues upfront. Pictures & renderings are used throughout the entire chapter to supplement the written content. The manufacturing drawings and datasheets for all components can be found in the chapter A.1 of the appendix.

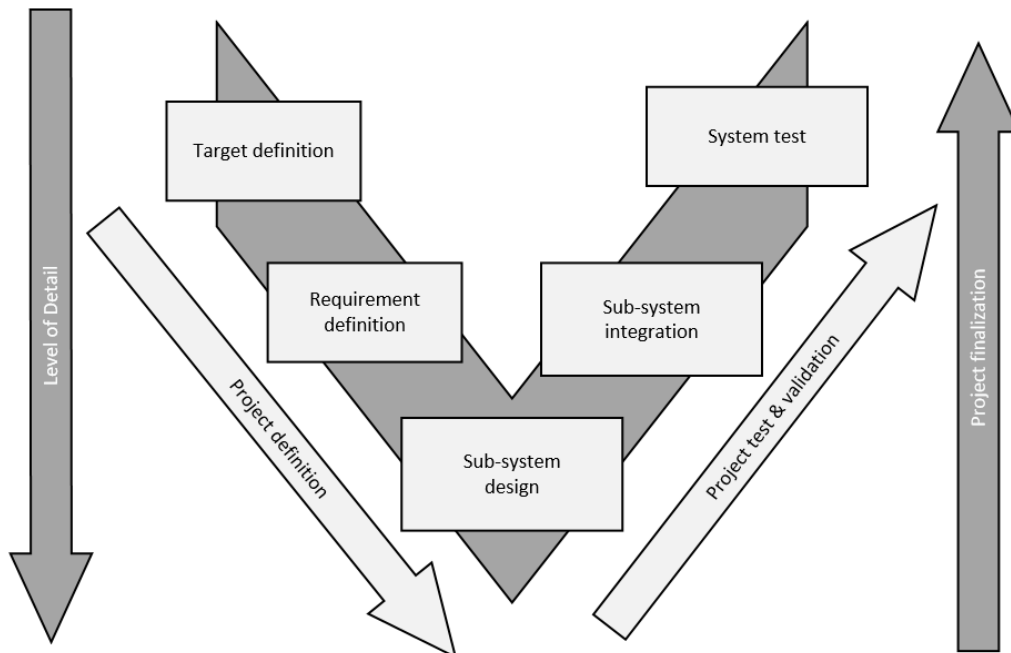


Figure 14: System design process [2]

### 3.1 Mechanical components

Throughout the entire design process, the CAD / CAE software Solidworks® was used to design the system. Building the assembly bottom-up was a result of the given dimensions from the unit under test (UUT). All the mechanical parts interfacing with the UUT are designed to connect to the bearing as close as possible to ensure maximum system stiffness, without compromising the handling and safety of the equipment during operation.

Figure 15 provides an overview of the final system with the main elements numbered as followed:

1. Locating frame and adjustable frame
2. Force application mechanism in the axial and radial direction
3. Rotor assembly

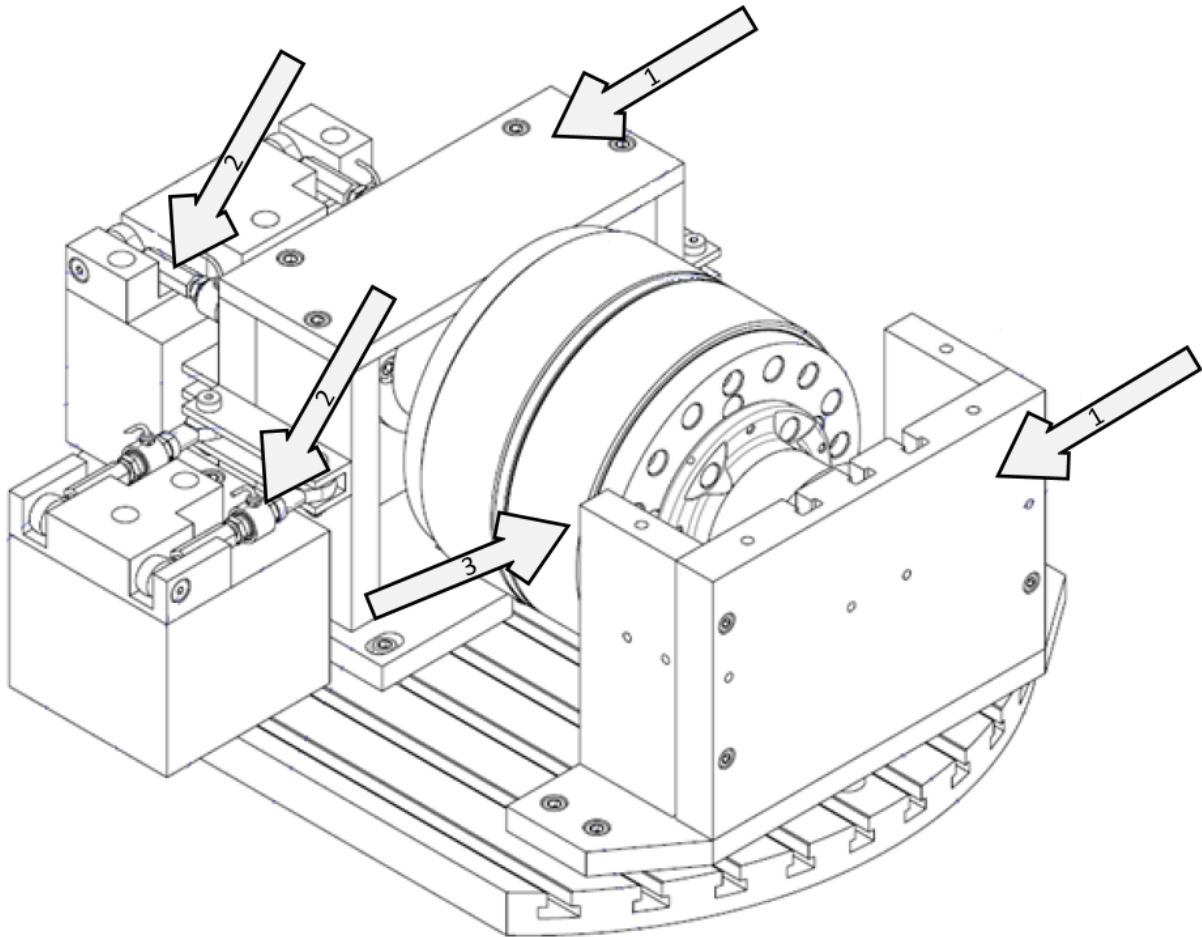
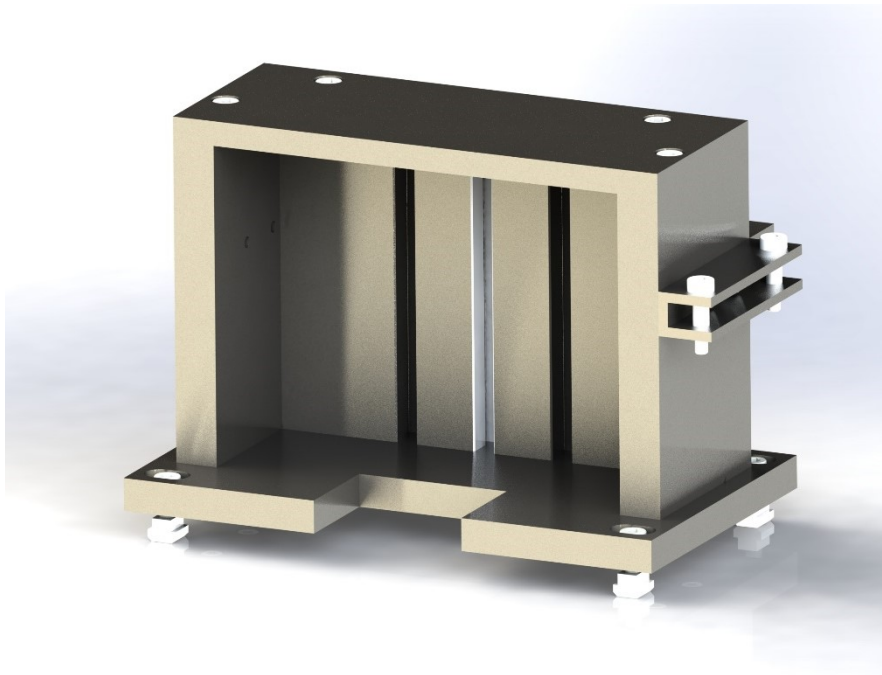


Figure 15: Mechanical system sketch

### 3.1.1 Adjustable and locating frame

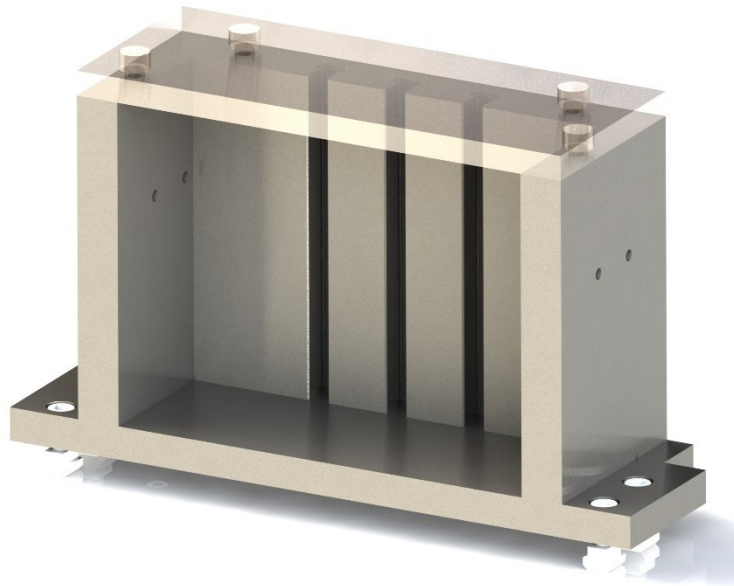
The frames where the bearings are mounted to have a simple, but even more critical task. The backplate with vertical T-nuts provides the possibility to use different UUT's with a defined interface. The side and top plates create a closed shear flow in the Y-Z plane, to ensure the highest possible rigidity within the given dimensions. This implicit requirement is defined by the nature of the force application system, which ideally requires an absolute stiff link to the UUT.

Figure 16 shows the adjustable frame with the connection rail to the force application mechanism shown on the right side of the picture.



**Figure 16: Movable frame with force application rail**

The backplate, as well as the side and the top plates, are identical for the locating as well as for the adjustable frame. The adjustable frame features a more substantial base plate and the mounting holes for the force application rail, compared to the fixed frame.



**Figure 17: Locating frame with a transparent top plate**

Both frames feature countersunk holes to provide a flat surface on the top of the baseplate. The holes on the adjustable frame are slotted by 10 mm to provide sufficient space for the deflection during the force application.

### **3.1.2 Force application mechanism**

This mechanism represents the core technology of the proposed setup. It is responsible for loading and deflecting the adjustable frame against the locating frame. The more robust and functional this setup is, the better the results will be. Therefore, a simple threaded solution was chosen, to tension the adjustable frame against a fixed reaction block. Both ends are fitted with ball heads and bolted with a locating screw to the respective frame.



**Figure 18: Pendulum rod including strain gauge**

The combined left and right-hand thread in the adjustment nut allows changing the length of the rod infinitely variable. Since this assembly directly creates the force between the two frames, it is obvious to place the strain gauge, required to measure the torque, right in between of the threaded studs. Details of the strain gauge are discussed in the sensor definition section of this chapter.

### 3.1.3 Rotor assembly

Two rim adapters, two flywheels, and a connecting plate are required to connect the two wheel hubs. All components are mirrored to create an equal load situation on the bearings. The entire rotor inertia, including the rotating components of the wheel hub, is calculated by the CAD system.

**Table 16: Inertia tensor, all values in  $\text{kgm}^2$**

$L_{xx} = 0.4561$	$L_{xy} = 0.0000$	$L_{xz} = 0.0000$
$L_{yx} = 0.0000$	$L_{yy} = 0.4574$	$L_{yz} = 0.0000$
$L_{zx} = 0.0000$	$L_{zy} = 0.0000$	$L_{zz} = 0.4574$

Table 16 shows the inertia tensor of the rotating assembly. Within the CAD coordinate system, the x-axis represents the rotational axis of the rotor. Therefore,  $L_{xx}$  represents the inertia relevant for our calculation. A reason for the deviation to the required  $0,6 \text{ kgm}^2$  is the physical mass of the rotor which should not exceed 50 kg due to handling reasons. The center of the

coordinate system is in the center of gravity of the entire rotor. Therefore  $L_{YY}$  equals  $L_{ZZ}$  which confirms the symmetrical setup. Figure 19 shows a section cut through the XZ-axis of the rotor. The unit under test is displayed in gold color; the rest of the testbed setup is shown in greyish colors.

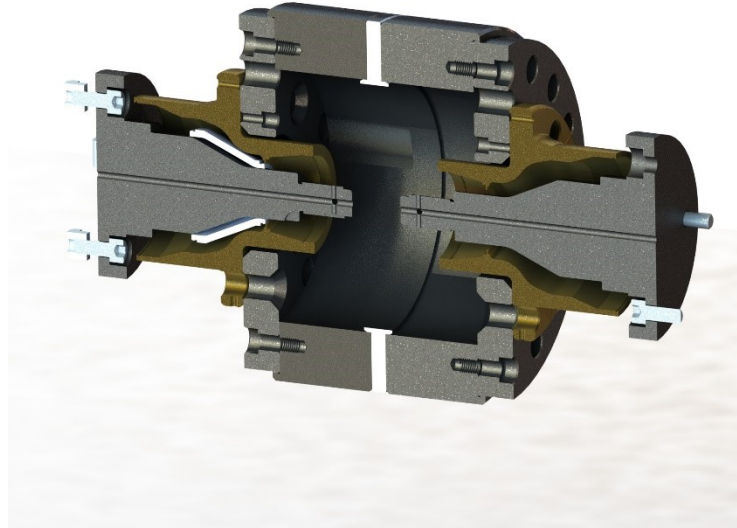


**Figure 19: The Assembled rotor**

### **3.1.4 Static simulation**

The assembly of the discussed parts must withstand forces of approximately 18000 newtons of force and is containing a rotor of 50 kilograms in mass. A static simulation based on the finite element method was performed to ensure the rigidity of the equipment and safety during operation. Solidworks® Simulation was used to perform this simulation. Like any other simulation tool, the workflow consists of the following steps:

1. Model preparation
2. Definition of the simulation type
3. Definition of boundary conditions
4. Creating the mesh
5. Solving
6. Data analysis

First, a static simulation was performed. Based on this simulation it is possible to estimate the stress in the components as well as the overall system stiffness.

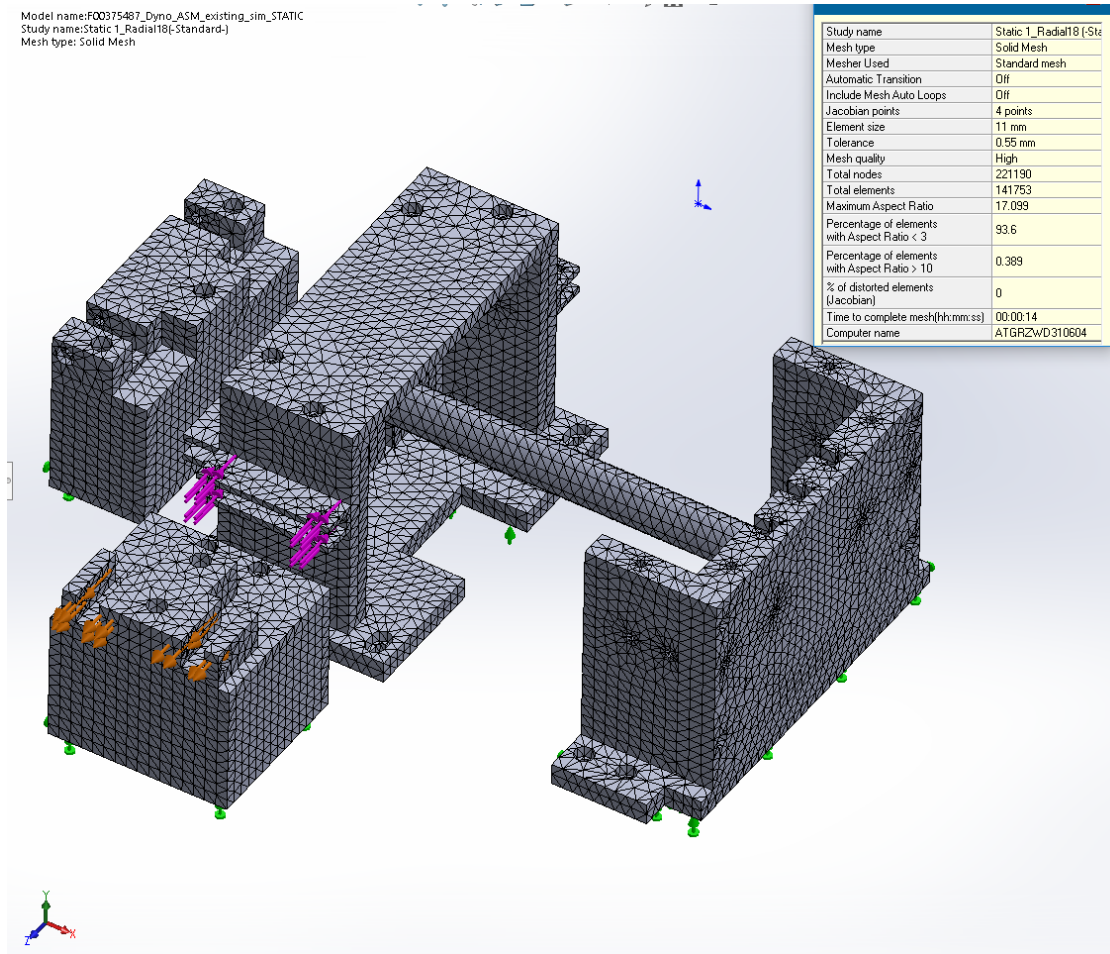


**Figure 20: Mesh & boundary conditions applied to the simulation model**

Figure 20 shows the abstracted simulation model with the necessary boundary conditions to run the simulation. In this case, the forces on the adjustable frame and the reaction forces are displayed in purple and orange color. The deformation boundary condition on the ground plate is shown in green.

The structural simulation was carried out with three different sets of boundary conditions:

- Radial force of 18 kN without axial force
- Axial force of 15 kN without radial force
- The combined axial and radial force

With the first two simulations, it is possible to calculate a numeric value for the stiffness between the reaction blocks and the adjustable frame. The stiffness provides information on the required force to deflect the setup by a certain amount. The boundary conditions determine the force, and the deflection is resulting from the calculation. Mechanical rigidity is an indicator of the quality of a testbed setup.

$$c_{a,r,combi} = \frac{F_{a,r,combi}}{x} \quad 13$$

Table 17: Calculated stiffness

	Force [N]	Deflection [mm]	Stiffness [N/mm]
Radial direction	18000	0.168	107142.9
Axial direction	16000	0.067	238806.0
Combined (vector sum)	24083	0.170	141665.8

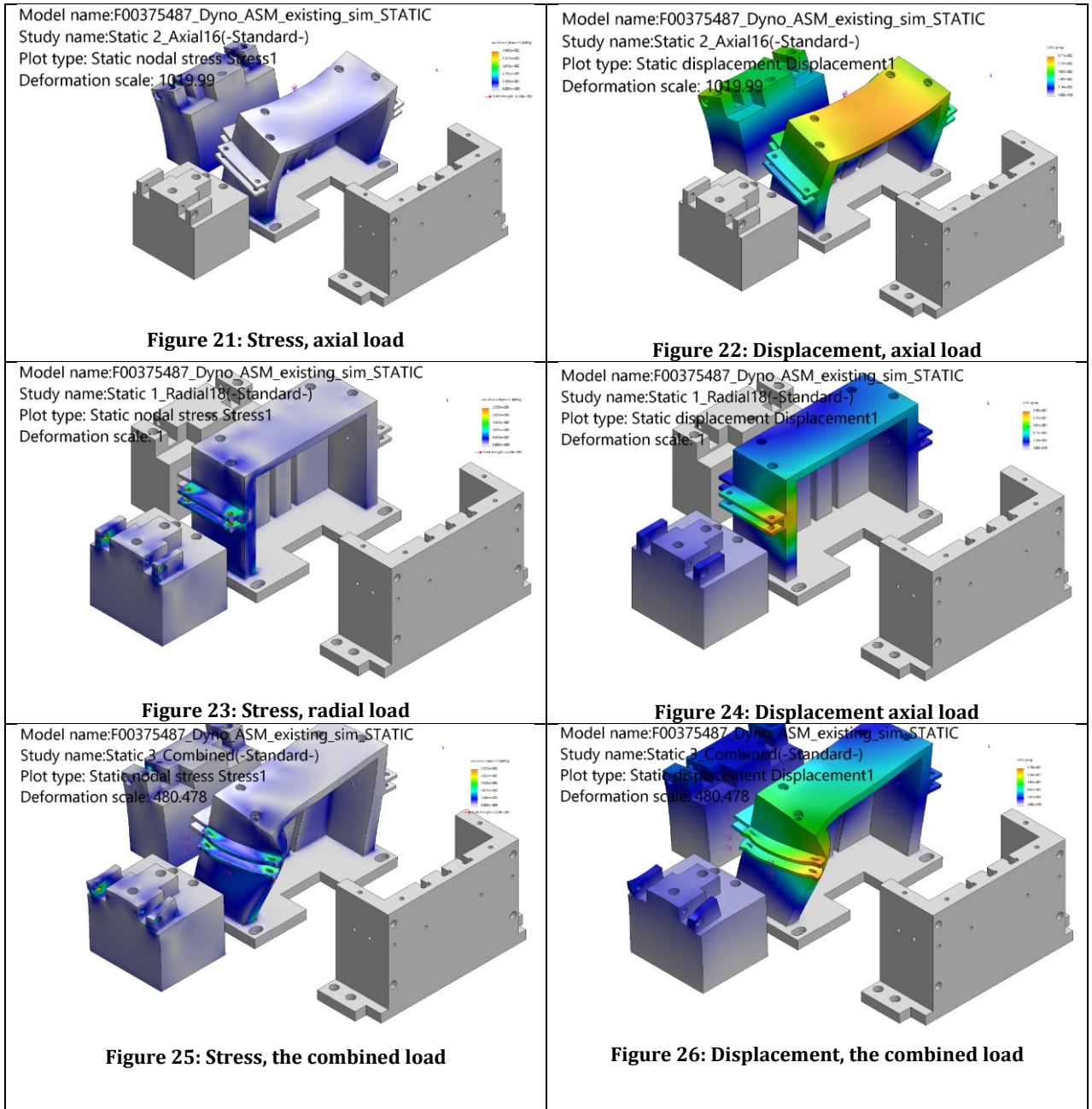
On the one hand, high stiffness values ensure that an angular or longitudinal error does not compromise the force transfer paths; on the other hand, it is an indicator for analyzing the structural eigenfrequencies. The method of finite elements is transferred to an eigenvalue approach, to quantify the resonance frequencies of the frame assembly as discussed in chapter 3.1.5.

Figure 21, Figure 23 and Figure 25 show the resulting von Mises stress in the adjustable frame under maximum load. High loads occur in the areas where the force application unit is connected. If the entire load is transferred via the fitting screw to the respectively tolerated holes, the stress results in the area of 100 MPa, leaving a safety factor of 2.3 to the yield strength of the used material.

Figure 22, Figure 24 and Figure 26 show zones of high physical deformation. The area around the second radial force application point displays the highest deformations, peaking at 0.17 mm at 18 kNm of force.

$$\frac{L}{1000} = \frac{210}{1000} > 0.17 \text{ mm} \quad 14$$

Comparing this value to the commonly used deformation rule for steel constructions [16] and a characteristic length of 210 mm, which is the height of the assembly, the maximum allowed deformation is calculated to 0,21 mm. Therefore, the maximum occurring deflection of 0,17 can be defined as not critical.

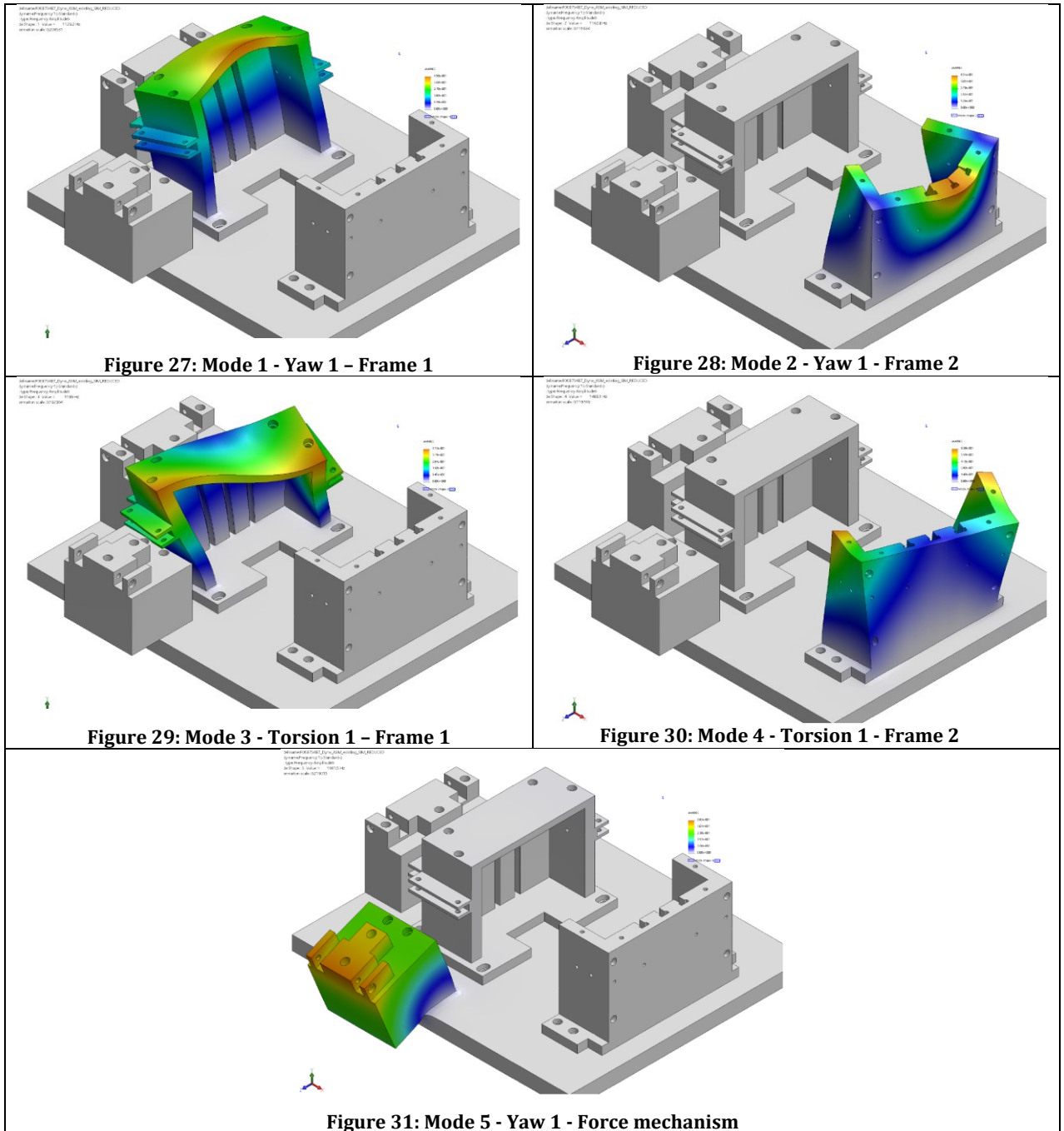


### 3.1.5 Dynamic simulation

An eigenmode simulation was performed to classify the quality of the system stiffness. This type of simulation provides an outline of the shape of the eigenmodes as well as the critical frequencies where these modes can be excited. In the decelerating rotor, due to unbalance forces, the primary mode of excitation is the 1<sup>st</sup> order. Equation 15 indicates the highest excitation frequency due to the unbalance.

$$f_{crit} = \frac{n_{max}}{60} = 44 \text{ Hz} \quad 15$$

The unbalance frequency should be lower than the first structural frequency by a factor of  $\sqrt{2}$ , which defines the lowest acceptable eigenmode frequency at 62,2 Hz [17]. The first five simulated eigenmodes are shown in Figure 27 to Figure 31.



The first mode of the adjustable frame, defined by its characteristic yaw shape, represents the lower boundary frequency and is calculated at 1129 Hz. The required eigenfrequency of 62,2 Hz shows a significant gap to the calculated 1129 Hz, and therefore the overall setup can be classified as acceptable for the given application task. Table 18 provides a summary of the calculated frequencies and corresponding mode shapes.

Table 18: Frequency table - Eigenmode simulation

Part	Mode #	Frequency	Mode Shape
Adjustable Frame	1	1129 Hz	Yaw X-Axis
	3	1189 Hz	Torsion Y-Axis
Frame without the top plate	2	1162 Hz	Yaw X-Axis
	4	1483 Hz	Torsion Y-Axis
Force application frame	5	1601 Hz	Yaw Z-Axis

### 3.2 Drive Motor

The drive motor and its engagement mechanism are responsible for the safe and fast acceleration of the rotor to the maximum speed of over 2600 RPM. Once the dedicated maximum speed is reached, the entire motor assembly should decouple, and the run-out test begins. The decoupling is necessary to avoid any braking torque induced by the motor and the friction wheel.

With a diameter of 270 mm for the rotor and a chosen diameter of 100 mm for the friction wheel, the motor speed calculates according to Equation 16 to 7020 RPM to reach the test specimen speed of 2600 RPM.

$$n_{motor} = \frac{n_{max} * d_{flywheel}}{d_{friction\ wheel}} \quad 16$$

$$= 7020 \text{ RPM}$$

The estimated drive torque to reach the maximum testing speed in an adequate amount of time can be found with the equation of motion. With an acceleration speed gradient of 50 RPM per second, the acceleration time ends up being less than 60 seconds, which is considered acceptable for this test setup.

$$T_{motor} = \frac{T_{max} * d_{flywheel}}{d_{friction\ wheel}} + \frac{J * \pi * n_{wheel}}{30} \quad 17$$

$$= 3,15 \text{ Nm}$$

The first summand represents the torque required to overcome the estimated friction torque of the rotor at maximum speed (see Chapter 2.5.1). The second term estimates the torque required to accelerate the system. By splitting up the results, it can be found that 75 % of the required 3,15

Nm is required to accelerate the system with a speed gradient of 50 RPM per second. The remaining 25 % is required to overcome the friction torque at maximum speed.

$$P_{motor} = T_{motor} * \omega_{motor} = 2374,5 \text{ W} \quad 18$$

The resulting power is not including any losses created by the friction wheel or by the mechanical efficiency of the drive system. A safety factor  $s = 1,2$  is chosen to calculate the required electrical supply. The friction wheel diameter of 100 mm gives an implicit boundary condition regarding the motor size. For the chosen engagement mechanism, the motor housing must be smaller in diameter than the wheel to provide enough space for the engagement mechanism.



Figure 32: Pichler Boost 180 motor



Figure 33: Motor controller S-CON 150HV

Reliable motors with these dimensions can be found in the field of RC sport. The Pichler Boost 160/180 motor series [18] provides a solid base within the given boundaries.

$$I_{supply} = \frac{P_{motor} * s}{U_{nominal}} = 64,8 \text{ A} \quad 19$$

The required current results from the nominal voltage to run the system and the maximum peak power defined by the test bed. A series of 2 x 6 cell lithium ion accumulators can reliably provide the required 64,8 amperes of current.

Table 19: Motor design parameters

Motor data – Boost 180	
Dimensions in mm	80 x 78
Mass in grams	1065
Shaft diameter in mm / Thread size	10.0 / M10
Li-Po	10-12S
Ri (mOhm)	31
Io (A)	1.2
Revolutions per Volt/min. (KV)	185
Overload current (20 sec)	85A
Motor controller	PICHLER S-CON 150 HV

An engagement mechanism is necessary to ensure a sufficient traction force. As a design parameter for this mechanism, the required radial force can be estimated with equation 20.

$$F_{radial} = \frac{F_{traction}}{\mu} = \frac{T_{motor\_electric}}{r_{friction\ wheel} * \mu} = 315\ N \quad 20$$

A linear electric cylinder can apply this force constantly and is therefore chosen for this application. The chosen cylinder can provide a maximum force of 1000 N, where the actual force of the cylinder can be limited by the electrical current to the system. This limitation also acts as an overload safety mechanism to avoid an overload on the motor.



Figure 34: Electrical cylinder[19]

### 3.3 Data acquisition & analysis

As described in chapter 2.4, the impulse loss method requires a speed signal to calculate the friction torque. It is necessary to store also the necessary ambient values as temperature and the forces on the force application mechanism to quantify the test conditions accurately. Additionally, the chosen motor and inverter setup require an input signal which should be ideally provided by the data acquisition system. Therefore, the following channels are required:

- Speed sensor (input signal)
- Temperature sensor (input signal)
- 4 x Force sensor (input signal)
- Speed output (setpoint – output signal)

#### 3.3.1 Speed signal

Given by the maximum system speed the angular frequency calculates to 43 Hz. The sensor requires a cut-off frequency of the angular frequency times the number of trigger points per revolution.

$$f_{max} = f_{rotor} * n = 350 \text{ Hz} \quad 21$$

Due to the rotor design, a hole pattern with 8 holes was used to pick up the speed signal. Therefore the minimum required cut-off frequency calculates to 350 Hz (see Equation 21). Therefore a high-frequency photo switch with a cut-off frequency of 1kHz was chosen.



Figure 35: IDEC laser sensor SA1E-L[20]

### 3.3.2 Temperature signal

It is necessary to measure the operating temperature of the unit under test to qualify the measured friction at a dedicated temperature. One possible location to measure is inside the bearing spindle. Based on internal studies [3], the expected temperature range of the UUT is below 120 °C and above room temperature, specified at 20 °C. RTD PT-100 Class AA sensors have an operating window of -50 °C to 250 °C. Therefore, this sensor with an outer diameter of 6 mm is used to measure the inner spindle temperature.



Figure 36: PT-100 sensor

### 3.3.3 Speed setpoint frequency

The speed setpoint frequency defines the speed of the drive motor at a given timestep. The motor controller requires a 50 Hz signal, similar to a PWM signal. The only difference is the standardized pulse width for 0 RPM at one-millisecond pulse width and maximum RPM at two milliseconds pulse width.

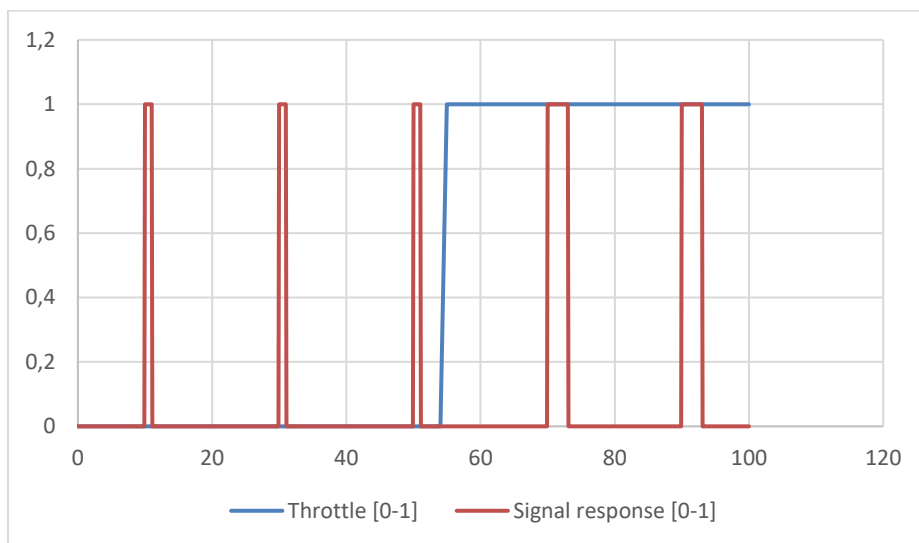


Figure 37: Setpoint speed signal, 0RPM, and maximum RPM

Therefore, a device or mechanism is needed that can provide the set speed signal shown in Figure 37. Since this device should be the same as the data storage device, this requirement is a prerequisite for the specification of the data acquisition device.

### 3.3.4 Data acquisition device

All the specified sensors and signals should be monitored by one single monitoring device. A monitoring device performs the synchronous time measurement of the signals. Hardware that is able to connect to all the described sensors, log high-frequency signals and create the setpoint frequency is the Delphin Expert Vibro. The highly performant I/O device has four high-frequency digital inputs, measuring at 1 MHz and eight high-frequency digital outputs, switching at 1 kHz which is compliant with the upfront defined signal requirements.



Figure 38: Delphin Expert Vibro[21]

For setting up the device, the native software Data Service Configurator is used. The data is analyzed and exported with the software ProfiSignal. The final data comparison is made with the AVL Software Concerto which will be described in chapter 4.

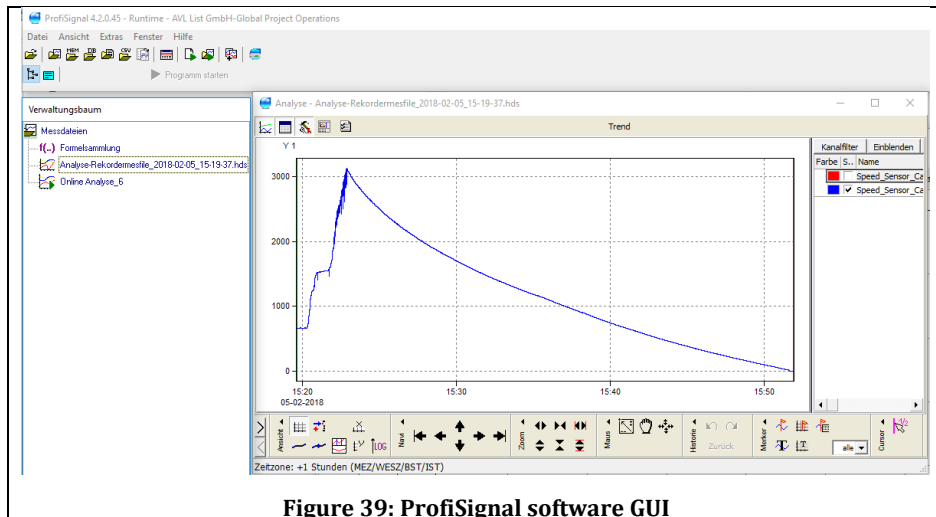


Figure 39: ProfiSignal software GUI

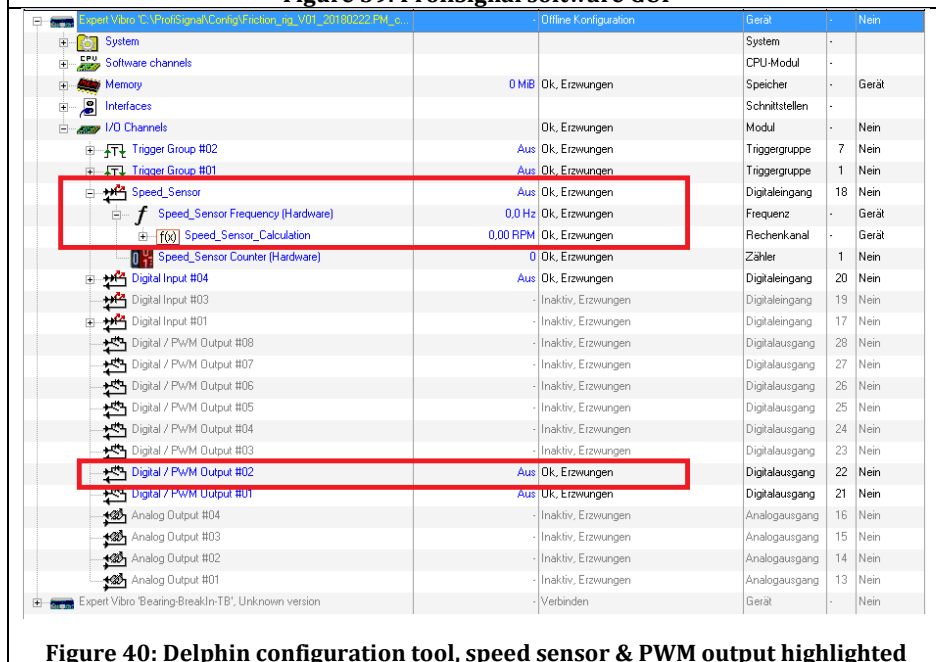
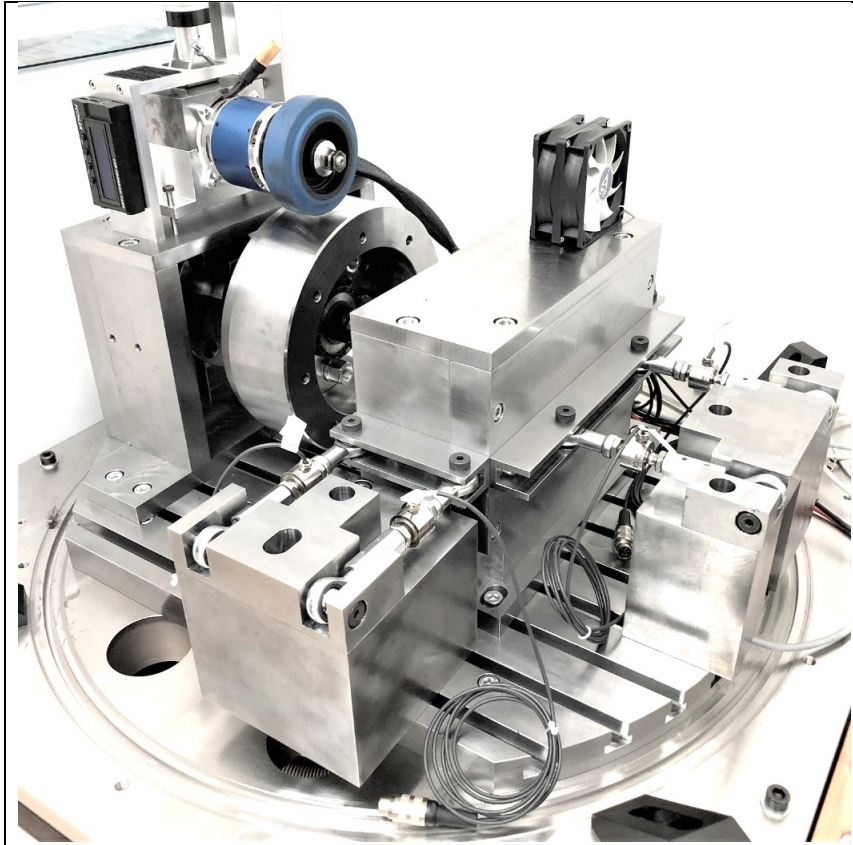


Figure 40: Delphin configuration tool, speed sensor & PWM output highlighted

### 3.4 Assembly & Commissioning

After the design of each sub-system, the rig was assembled and commissioned. Figure 41 gives an overview of the test setup during the commissioning phase, where the drive motor is mounted together with a half rotor assembly. Figure 42 focuses on the force application mechanism, with the two radial force actuators on the left and the two axial actuators on the right.

The act of commissioning a system describes all the necessary actions to assemble, install and test the sub-systems into one functioning entity. After setting up the mechanical components, all the measuring devices are installed and tested for functionality.



**Figure 41: Testbed overview**

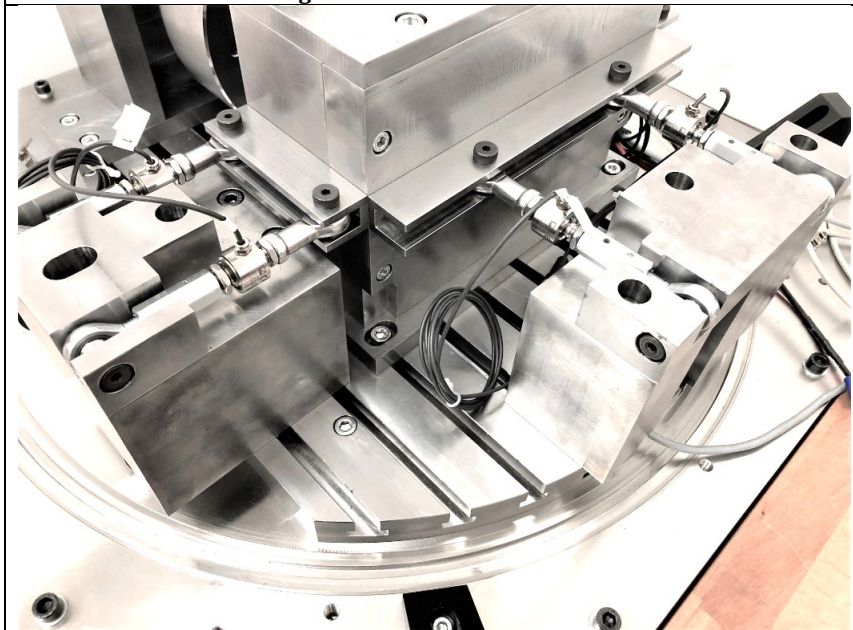


**Figure 42: Force application mechanism**

During the first tests with a rotating assembly, the focus is strictly on operational safety. Once the safe operation of the system is guaranteed, all the independent functions can be tested and assessed. The results based on this procedure are discussed in chapter 4. All detail drawings and specification sheets for the single components are added in the appendix of this thesis.

## 4 Results

The results from the commissioning phase and the first test runs should evaluate the capability of the system to fulfill the requirements specified in chapter 2.4. The corresponding procedure starts with the necessary function tests of each sensor and the first spinning tests at lower speeds and with only the half rotor mounted. Once these tests are successful, the first full-speed tests can be done to check the safe operation of the test bed. Once the system is able to run at full speed with the half rotor assembly, the complete rotor assembly is mounted and accelerated. The end of the commissioning phase is marked with a sign-off test that proves that the system is able to operate with the maximum force applied while the system spins at maximum speed and all the measured signals show values within a valid range. To sum it up, all the commissioning tests should be done to answer at least one of these questions:

- Is the system able to operate in the entire speed range?
- What is the lowest measurable torque?
- What is the highest measurable torque?
- What is the expected measurement accuracy?
- What is the expected repeatability?
- What is the expected reproducibility?
- How long does one standardized test take?
- Is there any shortcoming in the design or is the system not meeting a requirement?

Note: All tests are done with two different sets of units under test. This explains the difference in the overall torque levels between the chapters.

## 4.1 Commissioning tests

The first test series was performed to ensure the operational safety of the test setup. Therefore, the system speed was continuously ramped up, starting at 500 RPM and an increase of approximately 250 RPM between the tests. After each test, a visual check was performed. The tightening torques of all screws were checked after the first 2000 RPM run.



**Figure 43: Commissioning run**

Figure 43 shows one of the first commissioning tests, where a deceleration curve from 2000 RPM to 1000 RPM was logged, and the corresponding friction torque was calculated. The measured speed curve shows an almost constant deceleration rate with no visible fluctuation, where the calculated torque shows a +/- 15 % range in the total torque value. Within one test it is not possible to determine if the peaks, with amplitudes of more than 30 Nmm, are present or measurement artifacts due to unknown measurement errors. Therefore, it is necessary to do multiple tests and overlay the results based on the starting speed. This test configuration is evaluated in Chapter 4.2, where the overall measurement quality of the test bed is assessed.

The next commissioning test concludes the requirement of the speed capability. According to Figure 44, the maximum system speed was reached after an acceleration phase of 22 seconds at an acceleration rate of 118 RPM/s, which proves, that the system can operate in the entire defined

speed range. The system speed of 2600 RPM can be reached with a motor controller setting of 85 % and a ramp time of 22-24 seconds with one rotor. The speed capability of the full rotor set will be assessed in Chapter 4.5.

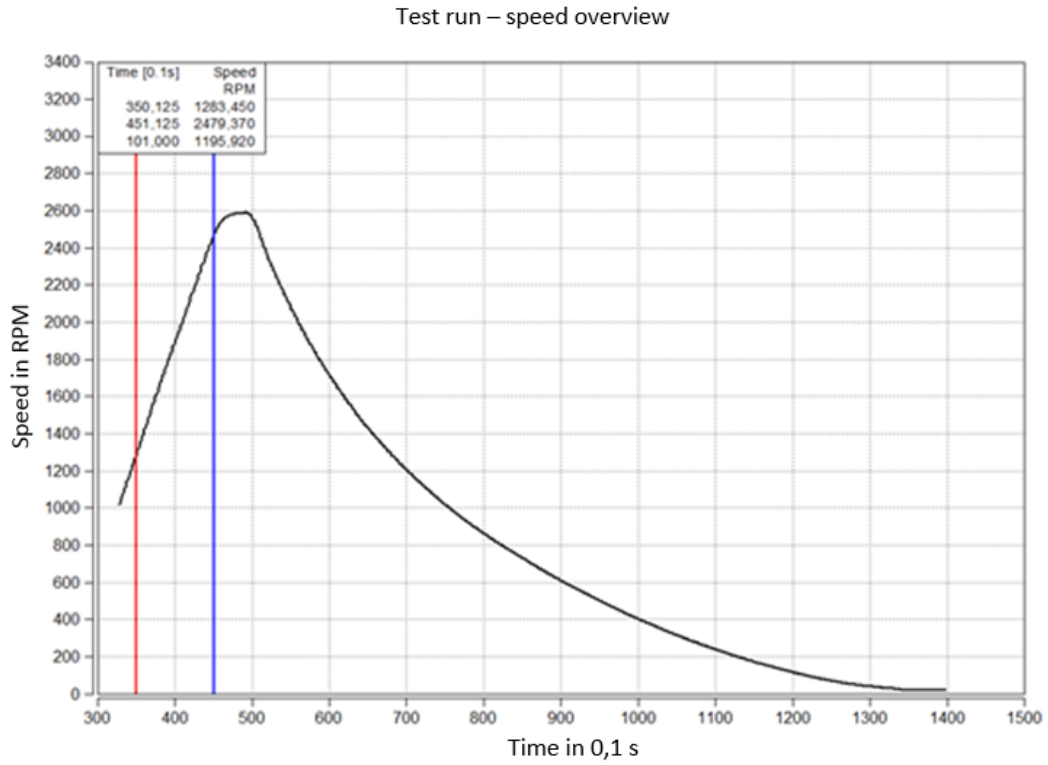


**Figure 44: Full system speed test run**

## 4.2 Repeatability of force conditions

After the commissioning tests, loads are applied to the non-rotating frame assembly, to quantify the reproducibility and repeatability of the force application mechanism. The system should be loaded with the maximum force in each direction, which is defined at 9 kN per Sensor in each direction.



Figure 45: Measurement device front plate

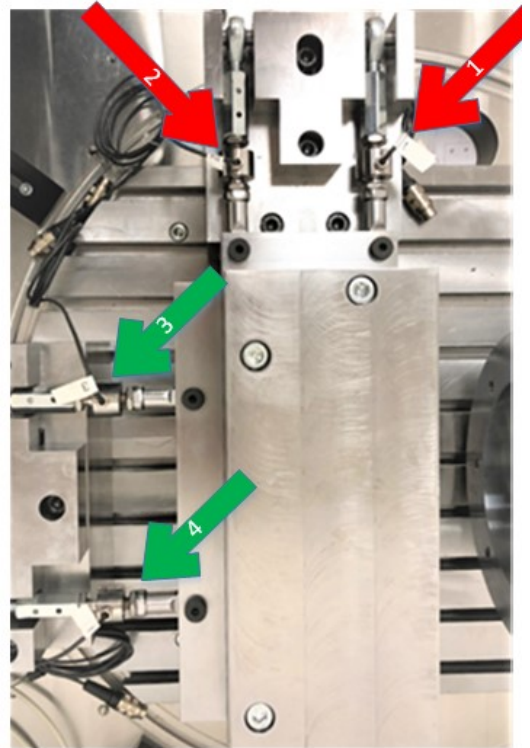


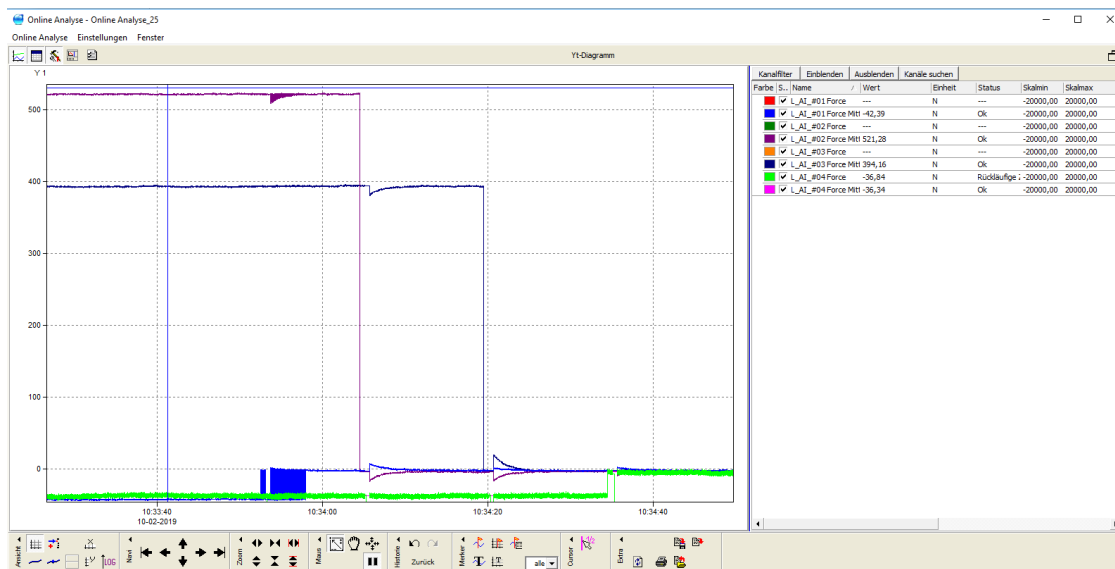
Figure 46: Sensor location, top right 1, left bottom 4



Figure 47: Charge amplifiers with paired sensor- and connection cables

Before the actual test, each sensor was paired with a charge amplifier. The datasheet of the charge amplifiers and the load cells can be found in the appendix of this thesis.

After the pairing of the sensor/amplifier units, an offset correction was necessary. Due to the tolerance of the inner resistances the sensors “measure,” a force value without any external force applied. Therefore it is necessary to shift the signal back to zero. This offset correction process is displayed in Figure 48, which shows a screenshot of the data analysis tool ProfiSignal® by the company Delphin Technology AG. In the left side of the diagram, it is visible that all sensors deviate from zero. One sensor after another was then offset corrected in the software, which can be seen in the sudden change in the force signal. On the right-hand side, the system is compensated and ready for operation.



**Figure 48: Offset correction of the sensor and amplifier**

With the calibrated system it is now possible to perform a reproducibility / repeatability test. The aim of this test is to adjust the force in the setup to a defined target as accurate as possible. A practical target value is the maximum force value which is 9000 N per sensor. Figure 49 shows such a reproducibility test, where three times the same load target had to be achieved. According to the graph, the average time to adjust the load between 2 sensors is around 50 seconds. The red vertical line indicates the location of the snapshot values, shown at the top of the graph. Each color indicates one test run. The top half shows the values over time for sensor number 1, the lower half for sensor number 2. By comparing two lines with the same color, it becomes evident that there is a cross-relation between the two forces. An increase in the force on one sensor leads to a decrease in the other sensor.

Force replication test

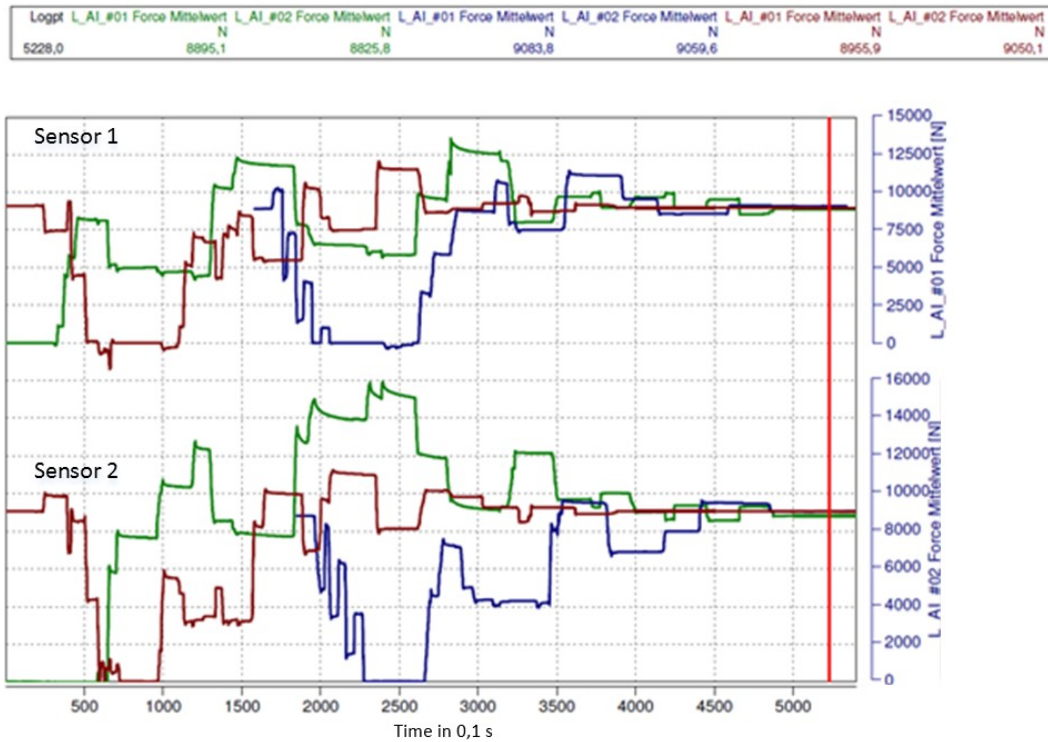


Figure 49: Force reproducibility test

As displayed in Table 20, the mean adjustability error over all tests is measured at less than 30 N. The highest error was measured at 174 N. The overall combined standard deviation is 96 N. Based on these results it can calculate the accuracy of the system.

Table 20: Force sensor statistics

Testrun	Target value	Sensor 1	Sensor 2	Combined Value	Error Sensor 1	Error Sensor 2	Combined Error
<b>Test 1</b>	9000 N	8895 N	8826 N		105 N	174 N	
<b>Test 2</b>	9000 N	9039 N	9060 N		-39 N	-60 N	
<b>Test 3</b>	9000 N	8956 N	9050 N		44 N	-50 N	
<b>Mean</b>	<b>9000 N</b>	<b>8963 N</b>	<b>8979 N</b>	<b>8971 N</b>	<b>37 N</b>	<b>22 N</b>	<b>29 N</b>
<b>Standard deviation</b>		<b>72 N</b>	<b>132 N</b>	<b>96 N</b>			<b>96 N</b>

Table 21 outlines the maximum and average accuracy levels on the total measurement range of the sensors as well as on the target value.

**Table 21: Accuracy of the force application & measurement**

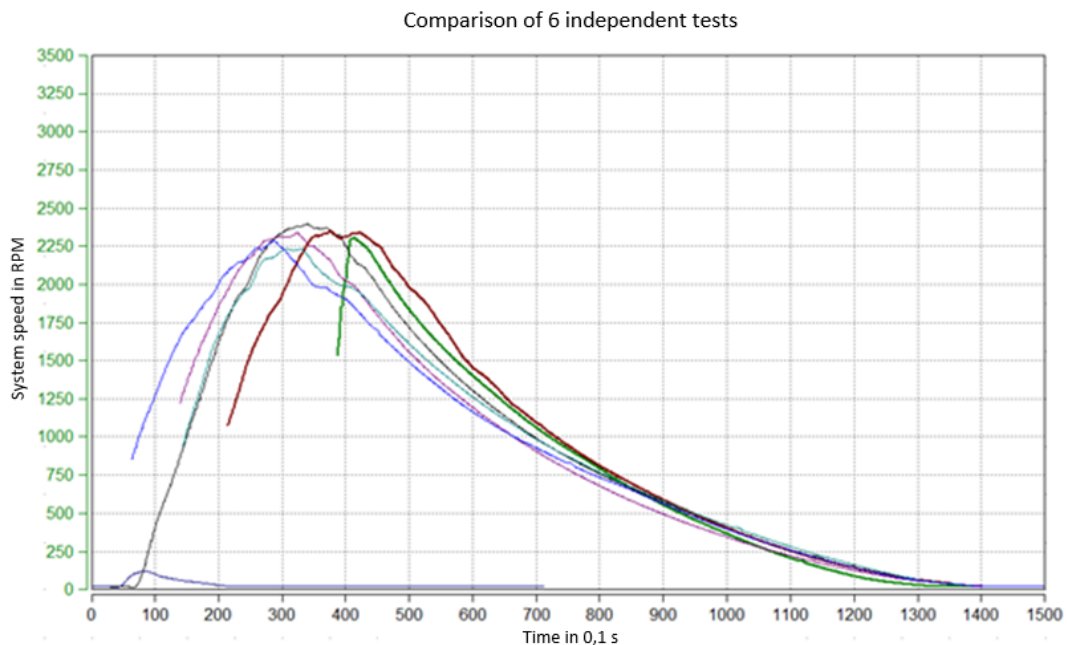
Accuracy	Maximum	Mean
% Target	1.9 %	0.4 %
% FS	0.9 %	0.2 %

The combined target error to adjust the force to a defined value is calculated at 1,9 % which confirms the required accuracy of 5 % specified in chapter 2.4.

### 4.3 Repeatability and reproducibility

Repeatability describes the variation that occurs when measurements are made under identical conditions. For the given setup this results in the need to test one given UUT multiple times by the same operator and the same test environment.

Figure 50 shows a summary of six similar test runs, executed within a short time frame. It is necessary to transform the speed signal to a torque signal via Equation 4, to calculate the given accuracy versus speed. Three measurements done right after each other are chosen from the given set of six measurements to calculate the repeatability.

**Figure 50: Repeatability test setting - speed over time**

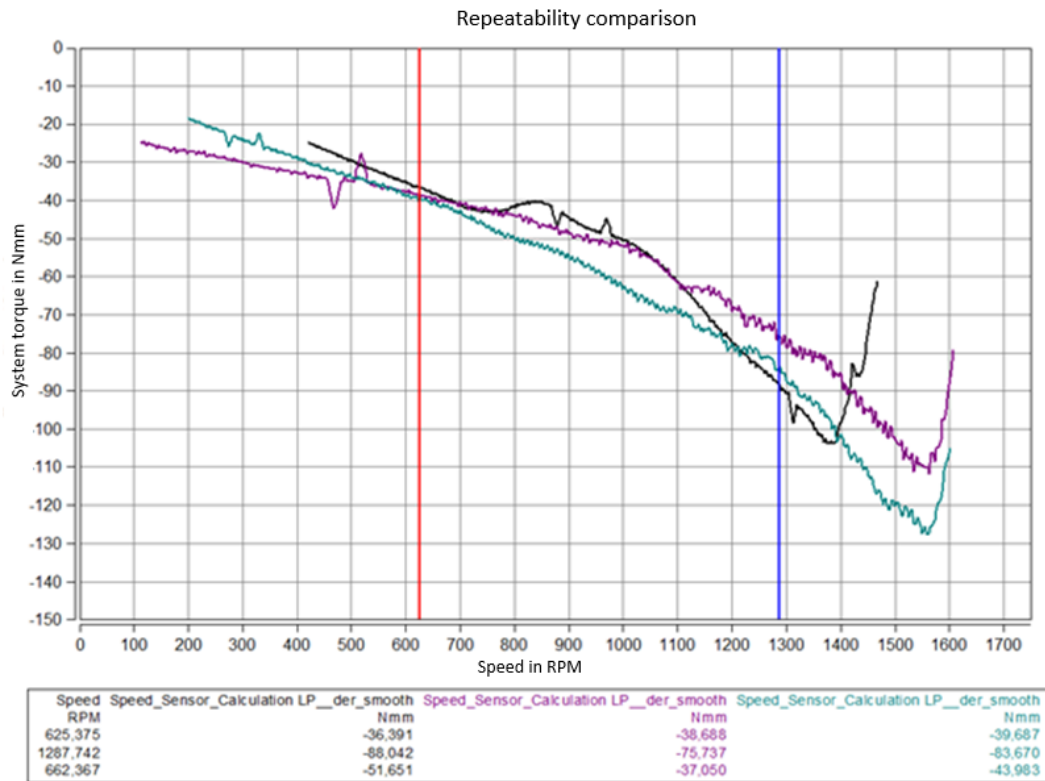


Figure 51: Torque repeatability - 2 evaluation points

The torque is plotted in Figure 51, where the 2 vertical lines indicate the randomly chosen evaluation points. Based on these values it is possible to calculate the repeatability based on the assumption that the target torque is the mean value of all test runs.

Table 22: Repeatability test results overview

Testrun	Speed 1	Speed 2	Combined Value	Error at Speed 1	Error at Speed 2	Combined Error
Test 1	36.39 Nmm	88.04 Nmm		0.99 Nmm	-5.89 Nmm	
Test 2	38.69 Nmm	74.74 Nmm		-1.31 Nmm	7.41 Nmm	
Test 3	37.05 Nmm	83.67 Nmm		0.33 Nmm	-1.52 Nmm	
<b>Target / Mean</b>	<b>37.38 Nmm</b>	<b>82.15 Nmm</b>				
<b>Standard deviation</b>	<b>1.18 Nmm</b>	<b>6.78 Nmm</b>	<b>3.98 Nmm</b>			<b>4.35 Nmm</b>

Compared to the overall friction torque this leads to statistical repeatability of 9 % at higher speeds and 19.8 % at lower speeds. This result indicates that a single test run is not representative of the overall mean value since the standard deviation is smaller than the expected deviation from

the test run to the mean value. Therefore it is recommended to perform at least a series of three to six test runs, in order to reach a statistical reproducible mean value for the friction torque.

**Table 23: Repeatability compared to Target and FS**

Accuracy	Speed 1	Speed 2	Combined
% Target	19.8 %	9.0 %	14 %
% FS	0.2 %	0.4 %	0.3 %

Reproducibility describes the variation that occurs when measurements are made under different conditions. Applying this definition to the PoC setup requires at least two different units under test with the precisely same specification and the independent testing of both groups under similar, but not precisely, the same conditions.

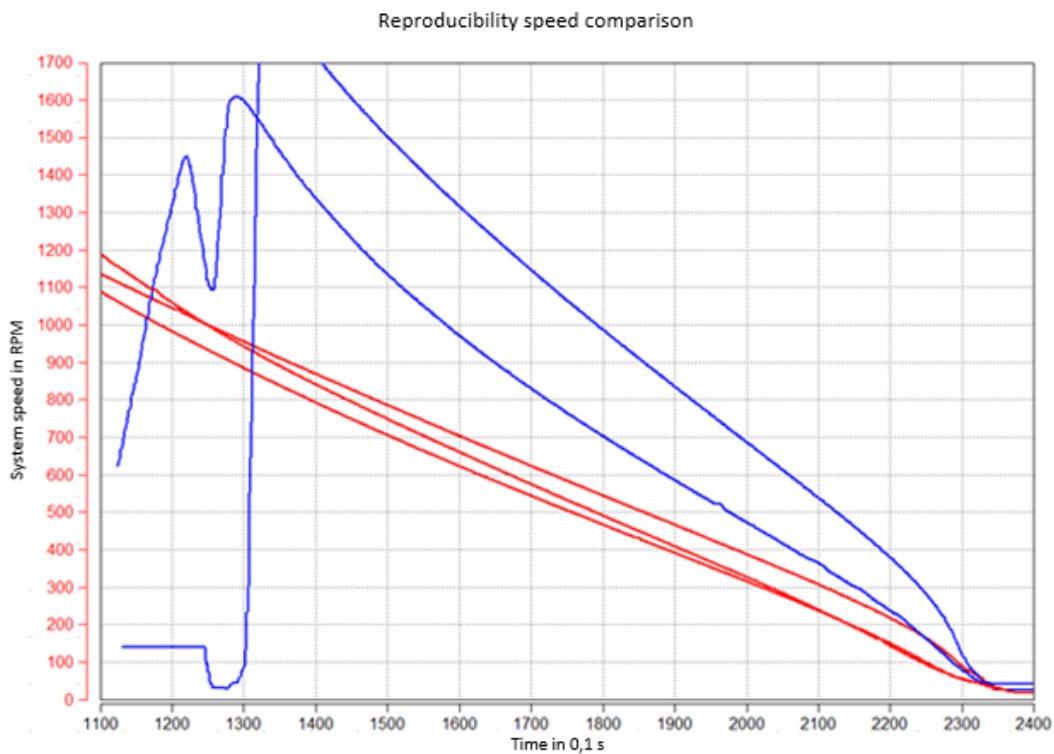


**Figure 52: Reproducibility speed comparison**

Figure 52 compares three test runs with the UUT used for the repeatability setup and two sets with a new UUT. It is evident that the new UUT has a different spin-out time, which could be due to several factors. One factor could be the break-in state of the bearings as described in chapter 2.5. The torque plot confirms the higher friction of the new unit under test.

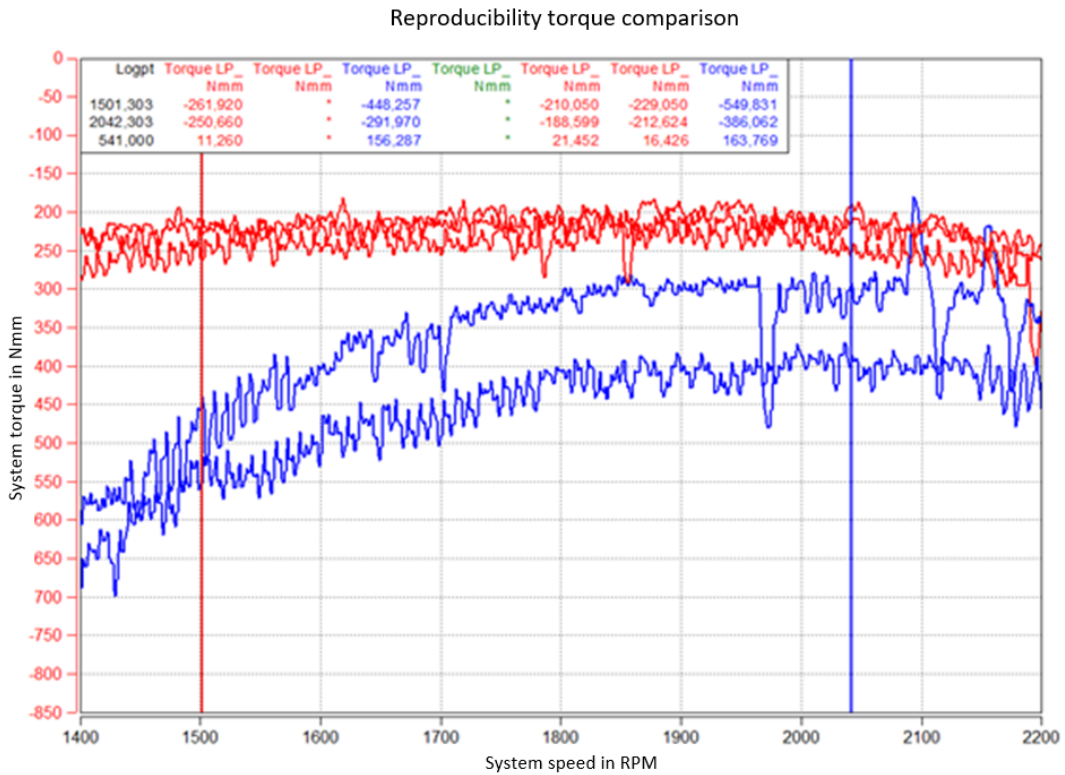


**Figure 53: Reproducibility Torque comparison**

Again, the vertical lines indicate the evaluation points; the two different colors in the data set are correspondent to the same UUT. This data is then used to evaluate the reproducibility of the system. Based on these results, the statistical reproducibility is calculated at 32 % of the nominal measurement value. Typically, the repeatability and reproducibility are compared to the full-scale boundary of the system, which is 2Nm, according to the requirements engineering chapter of this thesis. Table 24 gives an overview of the % FS values for the test rig.

Table 24: Reproducibility statistics

Testrun	Speed 1	Speed 2	Combined Value
Test 1 - UUT 1	261.90 Nmm	250.66 Nmm	
Test 2 - UUT 1	210.05 Nmm	188.60 Nmm	
Test 3 - UUT 1	229.05 Nmm	212.62 Nmm	
Test 1 - UUT 2	448.25 Nmm	291.97 Nmm	
Test 2 - UUT 2	549.80 Nmm	386.06 Nmm	
Mean 1	<b>233.67 Nmm</b>	<b>217.29 Nmm</b>	
Mean 2	<b>499.03 Nmm</b>	<b>339.02 Nmm</b>	
	<b>-265.36</b>	<b>-121.72</b>	<b>-71.82</b>
<b>Difference</b>	<b>Nmm</b>	<b>Nmm</b>	<b>Nmm</b>
<b>Reproducibility</b>			<b>32 %</b>
<b>Reproducibility FS</b>			<b>4 %</b>

The two mentioned parameters also define the overall precision of the measurement. All results within a certain margin of error are considered valid, and the corresponding mean values represent the real values, as long as they are statistically significant. By examining this convention, the following values for accuracy can be calculated:

Table 25: Accuracy level

Parameter	Target value	Full scale
Reproducibility	32 %	3.6 %
Repeatability	14 %	0.3 %
<b>Accuracy</b>	<b>46 %</b>	<b>3.9 %</b>

The 46 % combined accuracy indicates that a single test run is not sufficient to get a reliable data set. Again, 3-6 test runs are recommended to get an averaged measurement result.

#### 4.4 Overall Friction correlation

With the calculated accuracy levels, it is now possible to assess the full capability of the test rig combining the force actuation to the rotating test. As discussed in chapter 2.5, the expected friction torque values are going to diverge from the measured values because of the unknown inner pretension force, but the overall tendency for increased friction in case of higher loads can be shown by comparing the following test runs:

- Without force, the half rotor assembly
- Without force, the entire rotor assembly
- Half force, the entire rotor assembly

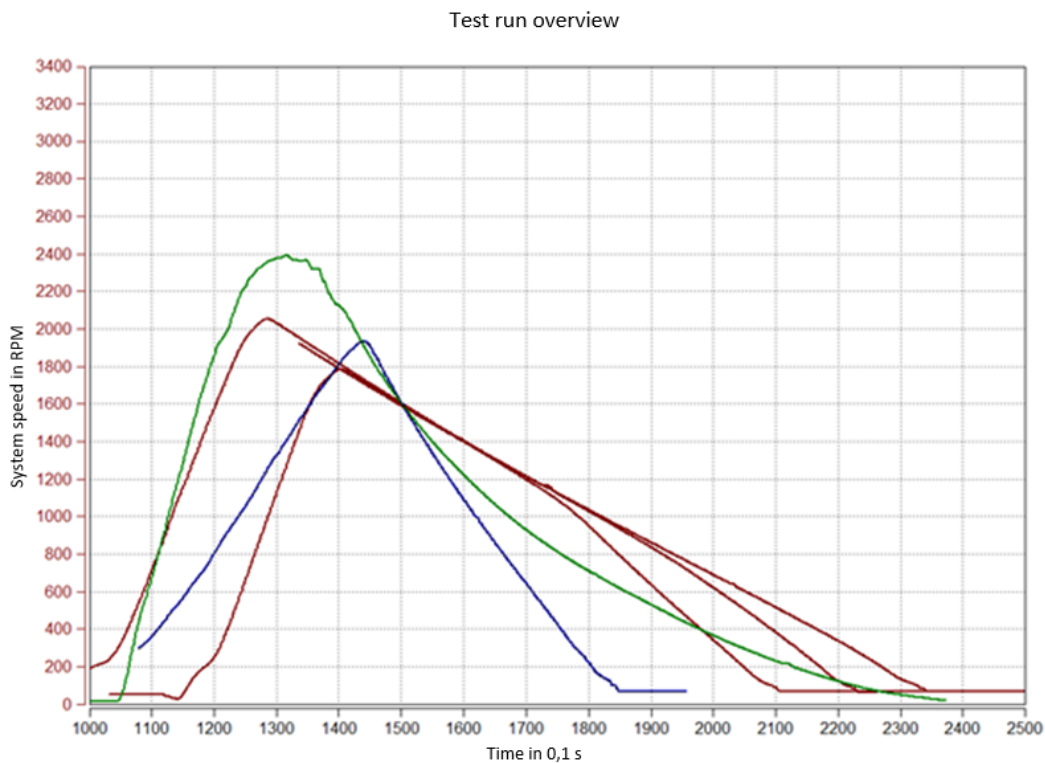


**Figure 54: Test run overview - half rotor, full rotor and with a load**

The green line shows a test run with the half rotor, as in the previous chapters, the three red lines show runs with the full rotor assembly but without any axial or radial load. Finally, the blue line indicates a radial and axial force of 5 kN each.

As predicted by the theory stated by Schäffler, it is visible, that the axial and radial forces have a significant influence on the friction, which can be seen in the steeper gradient of the blue curve in Figure 54 compared to the red curves.

The result indicates the importance of friction torque studies on wheel hub bearings. The torque loss for the measured curves is shown in the figure. Correlating the numbers outlines the potential to maximize the total efficiency value and therefore provide a basis to gain some critical 1/100 of a second within a race lap.

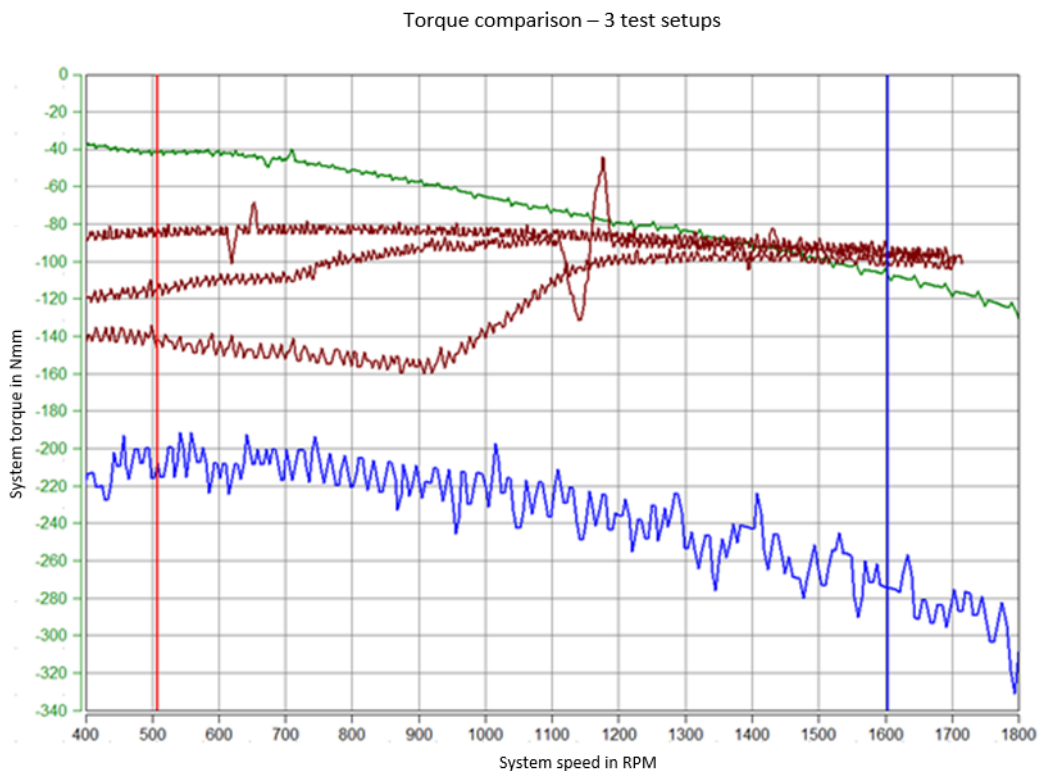


**Figure 55: Raw torque comparison, half rotor, full rotor, and loaded rotor**

Based on the values from Figure 55, the statistics of the torque increase can be calculated (Table 26). The loaded rotor shows an increased friction torque by 93,8 Nmm compared to the averaged full rotor runs and an increase of 166,46 Nmm compared to the half rotor test at low speeds. This equals an increase of friction compared to the full rotor test without load by 82 %. At higher speeds it is even more apparent: The increase of 184 % compared to the full rotor test runs results from a total loaded rotor torque of 274,2 Nmm. Compared to the significance values in chapter 4.3 both results are valid despite the fact that only one test run is shown in this graph.

**Table 26: Combined test run statistics**

	<b>500 RPM</b>	<b>1600 RPM</b>
Half rotor	42.10 Nmm	107.20 Nmm
Full rotor 1	86.67 Nmm	94.60 Nmm
Full rotor 2	115.20 Nmm	95.40 Nmm
Full rotor 3	142.40 Nmm	99.40 Nmm
Loaded rotor	208.56 Nmm	274.20 Nmm
Load vs. Full AV	93.80 Nmm	177.73 Nmm
Load vs. Half	166.46 Nmm	167.00 Nmm
Rel. Increase Load	82 %	184 %

## 4.5 Design of experiments

The next step was to have a look at the analysis of the data and to design a structured concept to evaluate engineering decisions as quickly as possible. A state-of-the-art approach to achieving this task is the concept of DoE (design of experiment), where mathematical models are used to estimate the outcome of a test. By redefining or compensating the model with real test data, it is possible to improve the quality of a model throughout the test significantly and therefore it is not necessary anymore to perform a full factorial test matrix.

A simple approach is to estimate the outcome of a test based on a state model. In the case of a wheel hub bearing, the Schäffler method described in chapter 2.5, can be used as a state model. By refining this model with test results, it is possible to improve the prediction quality of the model and therefore reduce valuable testing time.

Comparable to the degree of an equation, the first correlation of the state model to a test provides an offset compensation. The second correlation compensates for a gain error in the model. Nonlinear behavior can be predicted, starting from the third correlation.

$$T_0 = f_0 * (v * n)^{\frac{2}{3}} * d_M^3 * 10^{-7} - \Delta T_0 \quad 22$$

$$T_1 = f_1 * P_1 * d_M - \Delta T_1 \quad 23$$

Based on Equations 9 and 10, the extension with the terms  $\Delta T_0$  and  $\Delta T_1$  in Equations 22 and 23 represents the first order compensation to eliminate an offset error. To estimate the potential of quality improvement, a Schäffler state model is compared to a measured UUT.

The following values characterize this dedicated Schaffler state model:

- Kinematic viscosity according to ISO VG 100 at 70 °C
- no radial load
- 2000 RPM
- Mean bearing diameter  $d_M = 60$  mm
- $f_0$  according to chapter 2.5

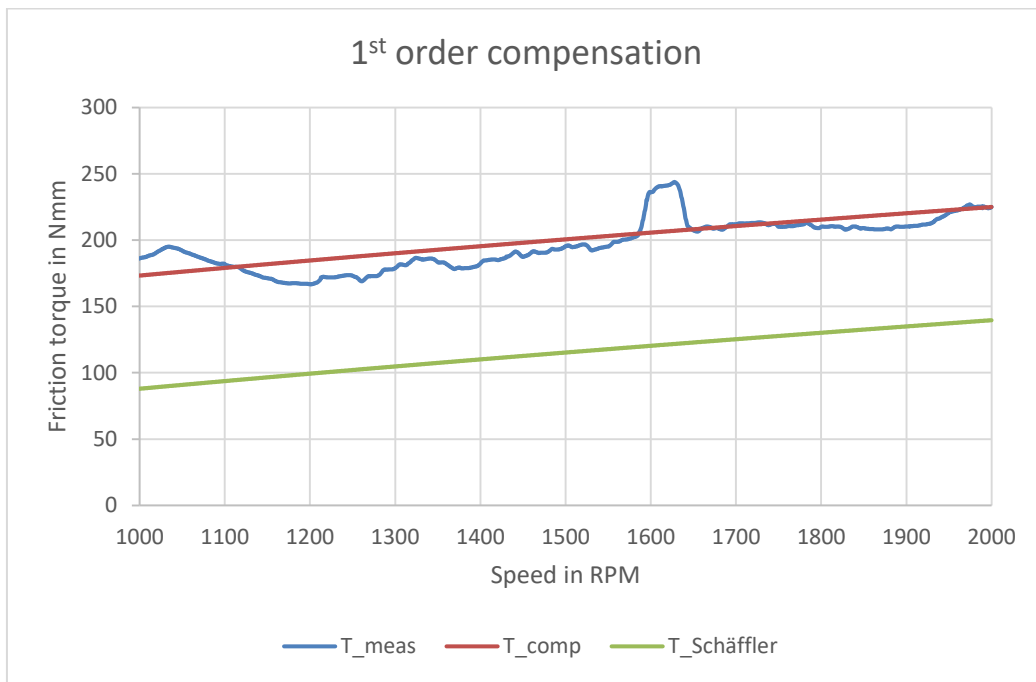


**Figure 56: Measured vs. calculated vs. compensated friction torque**

Figure 56 shows the significant difference between the measured values in blue and the calculated state model estimates in green. There are numerous reasons for this substantial difference, like:

- Factors  $f_0$  is an experimental factor based on experiments.
- Uncertainty in the kinematic viscosity of the used grease
- Unknown pretension force
- The accuracy of the measurement

Despite this uncertainty, it is evident that the gradient of the calculated friction torque is similar to the measured torque. Therefore, the method of a first order compensation is used to eliminate the unknown error in the state model. Figure 57 shows the compensated Schaffler values in red, compared to the measured values in blue.

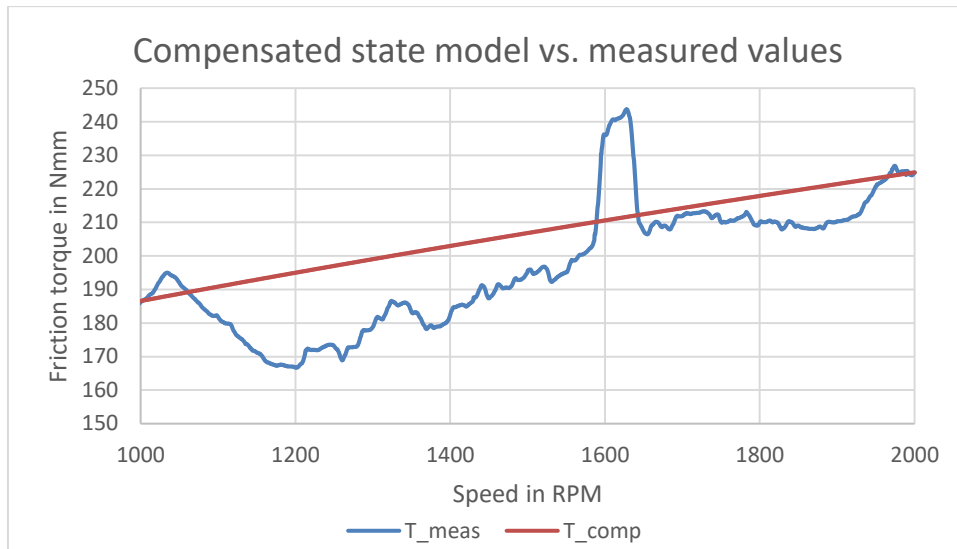


Figure 57: Refined state model

The result indicates a significant improvement and allows the estimation of the friction with an error of less than 30 Nmm. Figure 58 compares the compensated model error with the estimated model error, where the quality improvement is visualized over the speed range between 1000 and 2000 RPM. The method of order correlation can be used in a multi-dimensional manner. For the speed estimation, a correlation order of one is proved sufficient, however for other effects, like grease amount, pretension, axial and radial forces this method could be insufficient. The order evaluation of these effects is not part of this thesis and needs further investigation

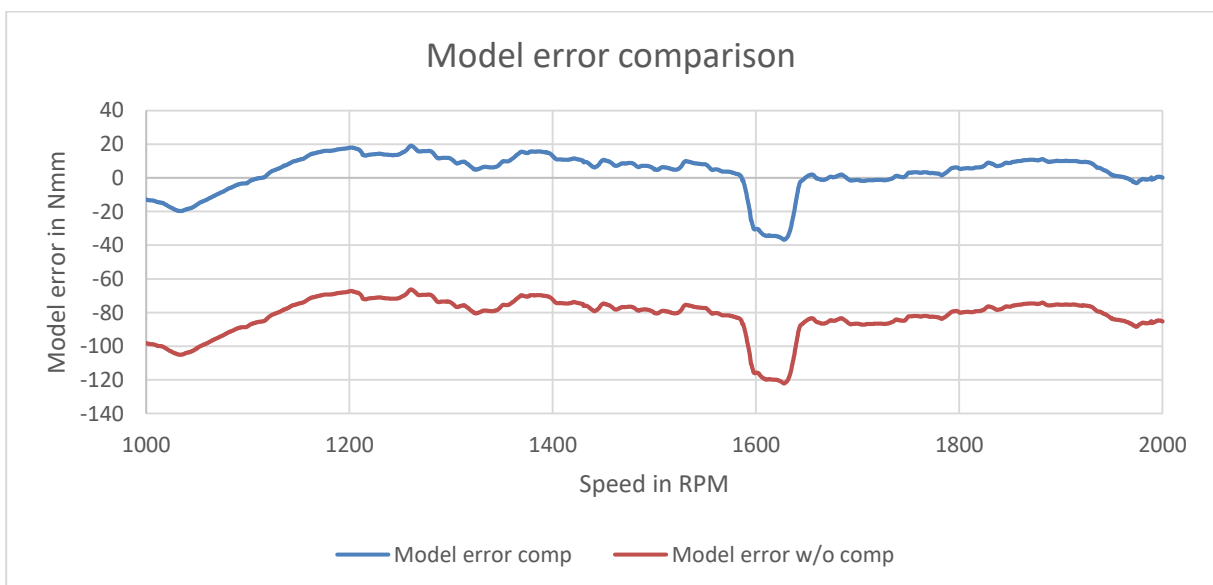


Figure 58: Model error comparison

## 5 Discussion

### 5.1 Conclusion

As described in chapter 4, the defined setup can achieve the requirements without sacrificing any essential boundaries. As an indicator, it is now crucial to compare the necessities, shown in Table 4, with the resulting parameters, calculated throughout the last chapter. The indicator column in Table 27 compares the achieved value to the target value. “+” indicates a fully achieved target, “o” a partially achieved target and “-“ a not achieved target.

**Table 27: Requirement achievement**

<b>Parameter</b>	<b>Value [Target]</b>	<b>Value [achieved]</b>	<b>Indicator</b>
Speed range	Up to 2600 RPM	2850 RPM	<b>+</b>
Z-Force	Up to 18,5 kN	40 kN	<b>+</b>
Y-Force	Up to 15 kN	40 kN	<b>+</b>
Force accuracy	< 5 %	Max. 1,9 %	<b>+</b>
Estimated friction value range	Up to 2000 Nmm	Up to 2000 Nmm	<b>+</b>
Data measurement	continuously	continuously and automatic	<b>+</b>
Relative friction measurement	Yes	Yes	<b>+</b>
Absolute friction measurement	Yes	With limitations	<b>o</b>
Repeatability	<10 Nmm	7,42 Nmm	<b>+</b>
Reproducibility	<10 Nmm	71,82 *	<b>o</b>
Accuracy	<5 Nmm	79,24 *	<b>o</b>
Cost efficiency	10 k€	8,5 k€	<b>+</b>

Based on these results it can be stated, that the impulse loss torque measuring principle is suitable to characterize a set of units under test over the entire speed range while providing high-quality data.

The values for reproducibility and accuracy (\*) are stated for a single run measurement, which was declared as unsuitable for the testing task. Overall it can be stated, that at least three successful measurements are required to get a statistical safety of less than 5 % based on the actual measurement value.

One limitation of the setup can be found in the static force application mechanism. With the given PoC it is not possible to apply speed dependent loads within one test run. Therefore it is still necessary to run a relatively high number of load variation tests to create a graph based on the longitudinal and lateral acceleration and vehicle speed – commonly known as GGK diagram. It is worth mentioning that this was not a design criterion for this test bed. However, it could be worth to investigate this in the future in an automatic and dynamic force application mechanism.

Another limitation is the capability to measure the absolute value of the friction torque. As stated in the introduction chapter, the setup should be able to determine the difference between two or more given sets of UUTs. The absolute value of the friction torque, however, requires the ability to eliminate or quantify the aerodynamic losses in the impulse equation. With a vacuum chamber, it is possible to measure the friction losses of the bearings without the aerodynamic forces. However, the procedure of evacuating the test chamber was defined as too time intensive within the given requirements for the development. As described by [4], the aerodynamic losses for a similar rotor assembly show a quadratic tendency with an aerodynamic braking torque of 22 Nmm at 2600 RPM. Subtracting this aerodynamic drag function from all measured values in this thesis is the easiest way to compensate for the aerodynamic drag, which is considered valid for the half rotor assembly, due to the similarity in the rotor layout. However, this is not valid for the full rotor assembly. Therefore, another possibility to estimate the friction is to calculate the aerodynamic drag with either via a simple calculation based on the theory of fluid transfer or a CFD model and subtract the result from the calculated torque in the Schäffler model.

## 5.2 Outlook

Due to the successful commissioning of this test bed, it is now possible to conduct further research in the area of friction development for bearing setups, like wheel hub assemblies. The same testing method and potentially the same test rig can be used to characterize other machine elements as well, in example sealings, gear sets, clutches, and other rotating components.

This exact setup will be used by the development partner AVL to evaluate the friction torque of wheel hub bearing assemblies. An improved version of the testbed would require a more robust drive motor and a re-engineered connection plate to the flywheel to accommodate an increased variety regarding test specimen. The handling of the massive rotor assembly could be improved by a 100-200 kg crane unit, either mounted directly on the test bed frame or mounted in the test cell itself.

For units under test with a higher friction torque, it would be possible to estimate the losses via the increase of temperature or a common torque measurement device, which would be a topic for further investigation in the future as well. For units with lower estimated losses, the measuring principle of impulse loss measurement still provides the highest accuracy. Therefore it can be stated, that this testing concept is worth to be re-engineered for other low-friction testing applications such as bearings, sealings, and gears.

The ability to adjust the applied forces throughout the test run could be assessed in another thesis or a development project. Implementing this ability would reduce the necessary number of tests even further.

The emulation of the temperature settings inside a racecar could be substantial to the testing results as well. Therefore it would be necessary to apply a heat source to the wheel carrier. The adaption of heating elements to the system can be done with low effort and is part of the development project following this thesis.

# List of Figures

Figure 1: NASCAR specified wheel hub .....	11
Figure 2: Vehicle coordinate system according to DIN / ISO 70000 and SAE J670e, reproduced from W. Hirschberg [6] .....	13
Figure 3: Tire coordinate system, reproduced from Goodyear[7].....	14
Figure 4: Simulated wheel speed.....	15
Figure 5: Simulated tire forces.....	15
Figure 6: Test cycle wheel speed vs. simulated wheel speed.....	15
Figure 7: Test cycle forces vs. simulated forces .....	15
Figure 8: System sketch, original drawing confidential [3] .....	16
Figure 9: Overview of the discussed torque measuring methods.....	19
Figure 10: Conceptional overview.....	29
Figure 11: Main bearing dimensions, reproduced from [12].....	32
Figure 12: Slip in a spherical roller thrust bearing. Reproduced from Piet M. Lugt [15] .....	35
Figure 13: Viscosity of ISO classes over temperature, reproduced from H. Nguyen-Schäfer [14]37	
Figure 14: System design process [2] .....	38
Figure 15: Mechanical system sketch.....	39
Figure 16: Movable frame with force application rail.....	40
Figure 17: Locating frame with a transparent top plate .....	41
Figure 18: Pendulum rod including strain gauge.....	42
Figure 19: The Assembled rotor.....	43
Figure 20: Mesh & boundary conditions applied to the simulation model .....	44
Figure 21: Stress, axial load.....	46
Figure 22: Displacement, axial load.....	46
Figure 23: Stress, radial load .....	46
Figure 24: Displacement axial load .....	46
Figure 25: Stress, the combined load .....	46
Figure 26: Displacement, the combined load.....	46
Figure 27: Mode 1 - Yaw 1 – Frame 1.....	47
Figure 28: Mode 2 - Yaw 1 - Frame 2.....	47
Figure 29: Mode 3 - Torsion 1 – Frame 1 .....	47
Figure 30: Mode 4 - Torsion 1 - Frame 2 .....	47
Figure 31: Mode 5 - Yaw 1 - Force mechanism .....	47
Figure 32: Pichler Boost 180 motor.....	49

Figure 33: Motor controller S-CON 150HV .....	49
Figure 34: Electrical cylinder[19] .....	50
Figure 35: IDEC laser sensor SA1E-L[20] .....	51
Figure 36: PT-100 sensor .....	52
Figure 37: Setpoint speed signal, 0RPM, and maximum RPM .....	52
Figure 38: Delphin Expert Vibro[21] .....	53
Figure 39: ProfiSignal software GUI .....	54
Figure 40: Delphin configuration tool, speed sensor & PWM output highlighted.....	54
Figure 41: Testbed overview .....	55
Figure 42: Force application mechanism .....	55
Figure 43: Commissioning run.....	57
Figure 44: Full system speed test run.....	58
Figure 45: Measurement device front plate .....	59
Figure 46: Sensor location, top right 1, left bottom 4.....	59
Figure 47: Charge amplifiers with paired sensor- and connection cables.....	59
Figure 48: Offset correction of the sensor and amplifier .....	60
Figure 49: Force reproducibility test .....	61
Figure 50: Repeatability test setting - speed over time .....	62
Figure 51: Torque repeatability - 2 evaluation points .....	63
Figure 52: Reproducibility speed comparison .....	64
Figure 53: Reproducibility Torque comparison .....	65
Figure 54: Test run overview - half rotor, full rotor and with a load.....	67
Figure 55: Raw torque comparison, half rotor, full rotor, and loaded rotor.....	68
Figure 56: Measured vs. calculated vs. compensated friction torque.....	70
Figure 57: Refined state model.....	71
Figure 58: Model error comparison.....	71

# List of Tables

- Table 1: NASCAR vehicle specification [5] ..... 12
- Table 2: NASCAR wheel speed distribution..... 13
- Table 3: Speed and force dataset ..... 15
- Table 4: Test rig requirements..... 17
- Table 5: Requirement Importance & Rating ..... 18
- Table 6: Relationship scores for a standardized HoQ ..... 21
- Table 7: HoQ for torque measurement methods..... 22
- Table 8: HoQ for speed measurement methods ..... 24
- Table 9: Guide to force transducer types and characteristics[11] ..... 25
- Table 10: HoQ for force measurement methods ..... 26
- Table 11: Measurement technology HoQ ..... 27
- Table 12: System HoQ..... 28
- Table 13: Friction components & influencing parameters..... 31
- Table 14: Reference bearing dimensions and characteristics ..... 33
- Table 15: Results friction torque estimation ..... 33
- Table 16: Inertia tensor, all values in  $\text{kgm}^2$  ..... 42
- Table 17: Calculated stiffness ..... 45
- Table 18: Frequency table - Eigenmode simulation..... 48
- Table 19: Motor design parameters..... 50
- Table 20: Force sensor statistics ..... 61
- Table 21: Accuracy of the force application & measurement ..... 62
- Table 22: Repeatability test results overview ..... 63
- Table 23: Repeatability compared to Target and FS..... 64
- Table 24: Reproducibility statistics ..... 66
- Table 25: Accuracy level ..... 66
- Table 26: Combined test run statistics ..... 69
- Table 27: Requirement achievement ..... 72

# List of Appendices

Appendix 1: Overview of the frame assembly and rotor .....	VII
Appendix 2: Global dimensions, side view.....	VIII
Appendix 3: Global dimensions, top view .....	VIII
Appendix 4: Parts list frame assembly and rotor.....	IX
Appendix 5: Assembly locating frame.....	X
Appendix 6: Adjustable frame assembly.....	XI
Appendix 7: Base plate locating frame .....	XII
Appendix 8: Base plate adjustable frame .....	XII
Appendix 9: Stiffener bracket left & right .....	XIII
Appendix 10: T-nut back plate.....	XIII
Appendix 11: Bracket for force application mechanism - radial .....	XIV
Appendix 12: Bracket for force application mechanism - axial.....	XIV
Appendix 13: Force application mechanism - radial assembly.....	XV
Appendix 14: Force application mechanism - axial.....	XV
Appendix 15: Force measuring assembly.....	XVI
Appendix 16: Spacer force mechanism – axial.....	XVI
Appendix 17: Spacer force mechanism – radial.....	XVII
Appendix 18: Rail – axial .....	XVII
Appendix 19: Rail – radial.....	XVIII
Appendix 20: Top plate.....	XVIII
Appendix 21: Side plate .....	XIX
Appendix 22: Motor mounting bracket bottom .....	XX
Appendix 23: Motor mounting bracket.....	XX
Appendix 24: Rework top plate.....	XXI
Appendix 25: Top plate motor mounting.....	XXI
Appendix 26: Actuator mount.....	XXII
Appendix 27: Friction wheel.....	XXII
Appendix 28: Laser switch .....	XXIII
Appendix 29: Drive motor .....	XXIV
Appendix 30: Motor controller .....	XXV
Appendix 31: Motor controller programming device .....	XXVI
Appendix 32: Accumulator .....	XXVII
Appendix 33: Cooling fan .....	XXVIII
Appendix 34: Electric cylinder.....	XXIX
Appendix 35: Motor mounting clamp .....	XXX
Appendix 36: Motor connecting bracket .....	XXX
Appendix 37: Battery charger .....	XXXI
Appendix 38: Main dimensions - Load Cell.....	XXXII
Appendix 39: Datasheet - Load cell.....	XXXIII
Appendix 40: Datasheet - Charge amplifier.....	XXXIV
Appendix 41: LiPo Safebag .....	XXXV
Appendix 42: Fire extinguishing granules .....	XXXVI
Appendix 43: Damaged S-CON 150 controller .....	XXXVII
Appendix 44: Damaged motor Boost 160 .....	XXXVIII

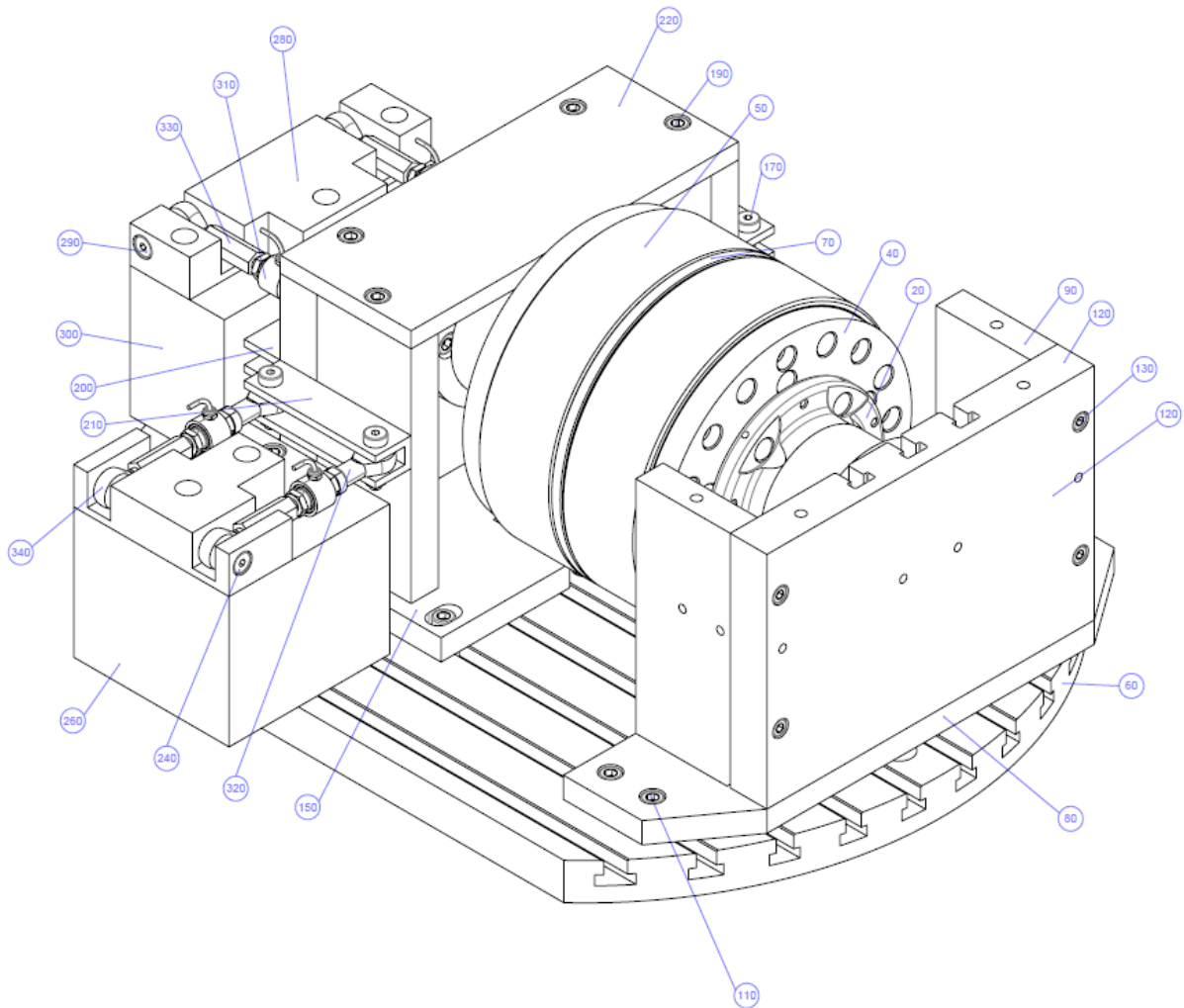
# Bibliography

- [1] **IMS LLC**, 2018, "Indianapolis 500 Historical Stats," 2019(01/08).
- [2] **AVL List GmbH**, 2014, "AVL Simulation and Testing Solutions Catalog," 2014 (17.07.2014).
- [3] **AVL List GmbH**, "AVL Internal Source - Confidential. to be Reviewed on Request,".
- [4] **Klemm, B.**, 2018, "Verlustmomentmessung Eines Radlagers".
- [5] **NASCAR Cooperation**, 2015, "NWMT Rulebook".
- [6] **Univ.-Prof. Dr.techn. Wolfgang Hirschberg, and Dr.techn. Helmut M. Waser**, 2014, "Automotive Engineering," Institute of Automotive Engineering, Graz.
- [7] **Goodyear**, 2018, "Goodyear Nascar Tire Picture," 2019.
- [8] **Encyclopædia Britannica, I.**, 2019, "Mechanical Efficiency," 2019.
- [9] **Hottinger Baldwin Messtechnik GmbH**, 2018, "Torque Measurement Methods," 2019.
- [10] **Chauvin Arnoux GmbH**, Kehl am Rhein, "Übersicht Über Verfahren Zur Drehzahlmessung".
- [11] **C.R. Howard**, 2013, "Guide to the Measurement of Force," The Institute of Measurement and Control, London,
- [12] **Schaeffler Technologies AG & Co. KG**, 2018, "Reibung Und Erwärmung," 2019.
- [13] **Timken Company**, 2019, "TIMKEN Mill Grease NLGI Grade 2," 2019.
- [14] **H. Nguyen-Schäfer**, 2017, "Numerische Auslegung Von Wälzlagern," Springer-Verlag GmbH, Deutschland, pp. 87-122.
- [15] **Lugt, P.M.**, 2013, "Grease lubrication in rolling bearings," 2013 John Wiley & Sons, Ltd, The Netherlands.
- [16] **Grote, K., Bender, B., and Göhlich, D.**, 2018, "Dubbel: Taschenbuch für den Maschinenbau," Springer Vieweg, Deutschland.
- [17] **Gasch, R., Nordmann, R., and Pfützner, H.**, 1975, "Rotordynamik," Springer Vieweg, Deutschland.
- [18] **Pichler GmbH**, 2018, "Boost 180 E-Motor," 2019.
- [19] **Conrad.at**, 2018, "Electric Cylinder," 2018.
- [20] **Conrad.at**, "Laser Sensor IDEC SA1E-L," 2019.
- [21] **Delphin Technology AG**, 2019.

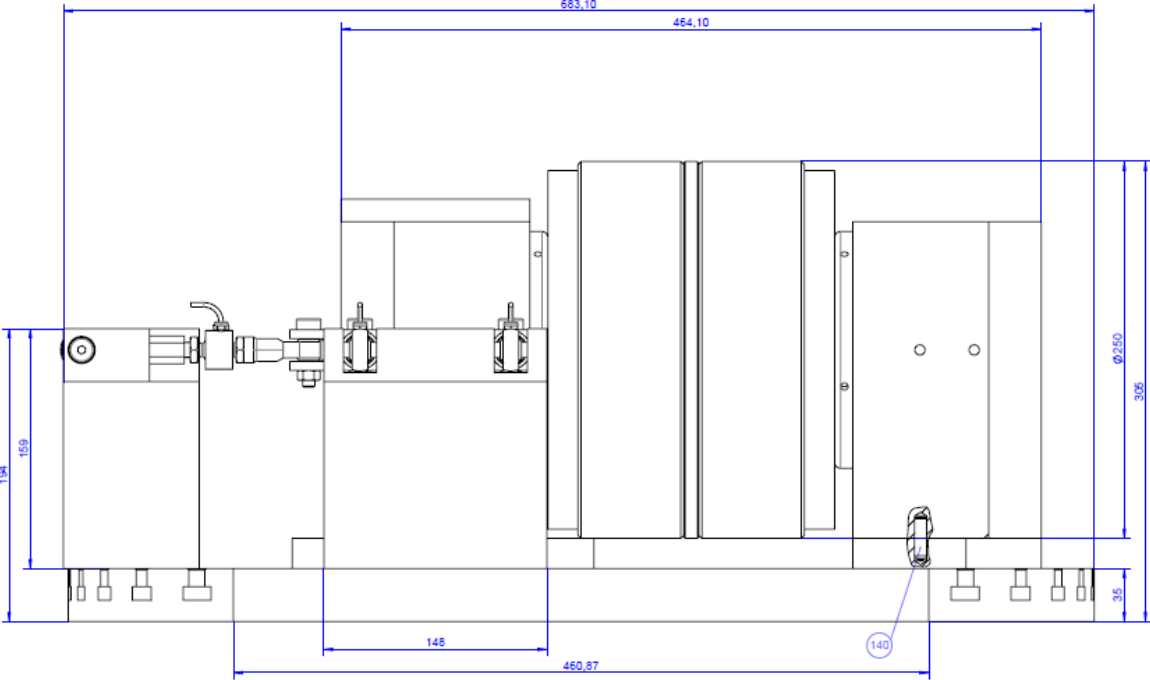


# A. Appendix

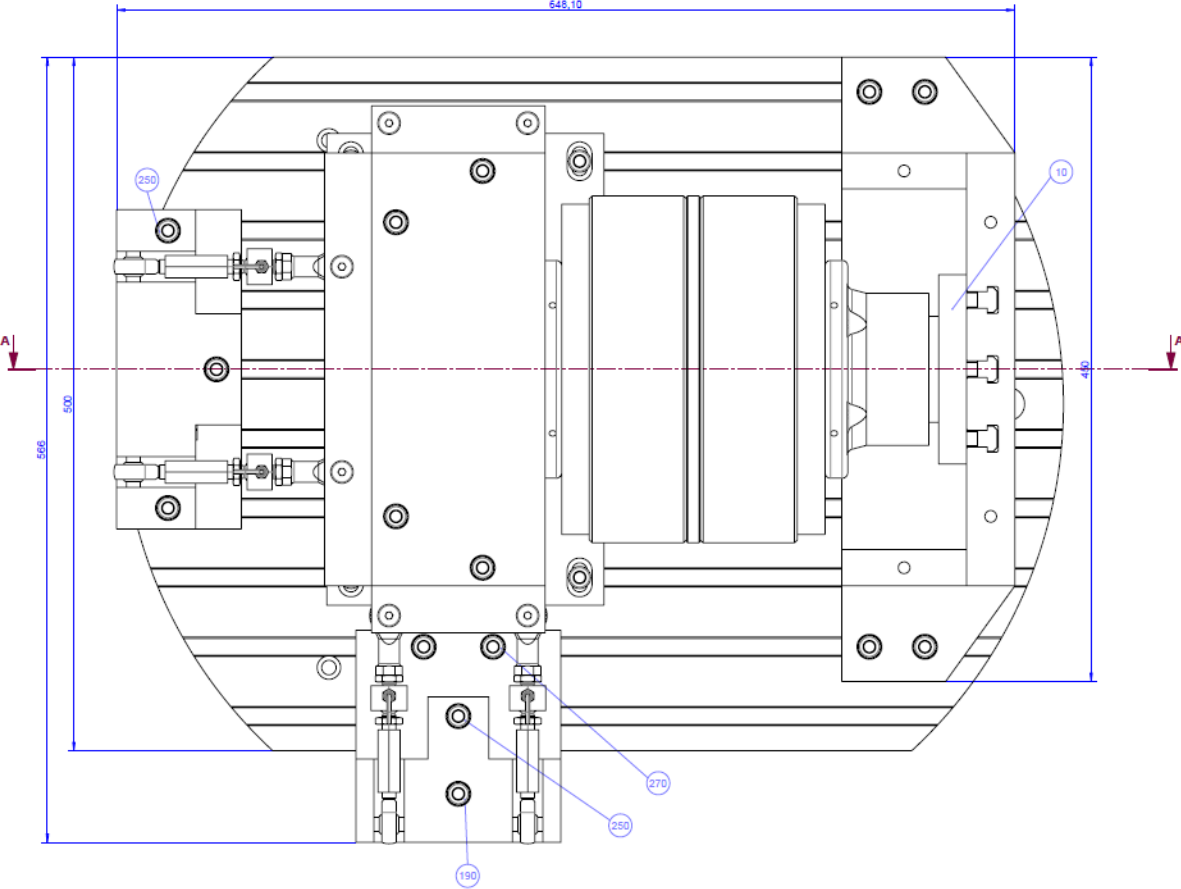
## A.1 Drawings



**Appendix 1: Overview of the frame assembly and rotor**



Appendix 2: Global dimensions, side view



Appendix 3: Global dimensions, top view

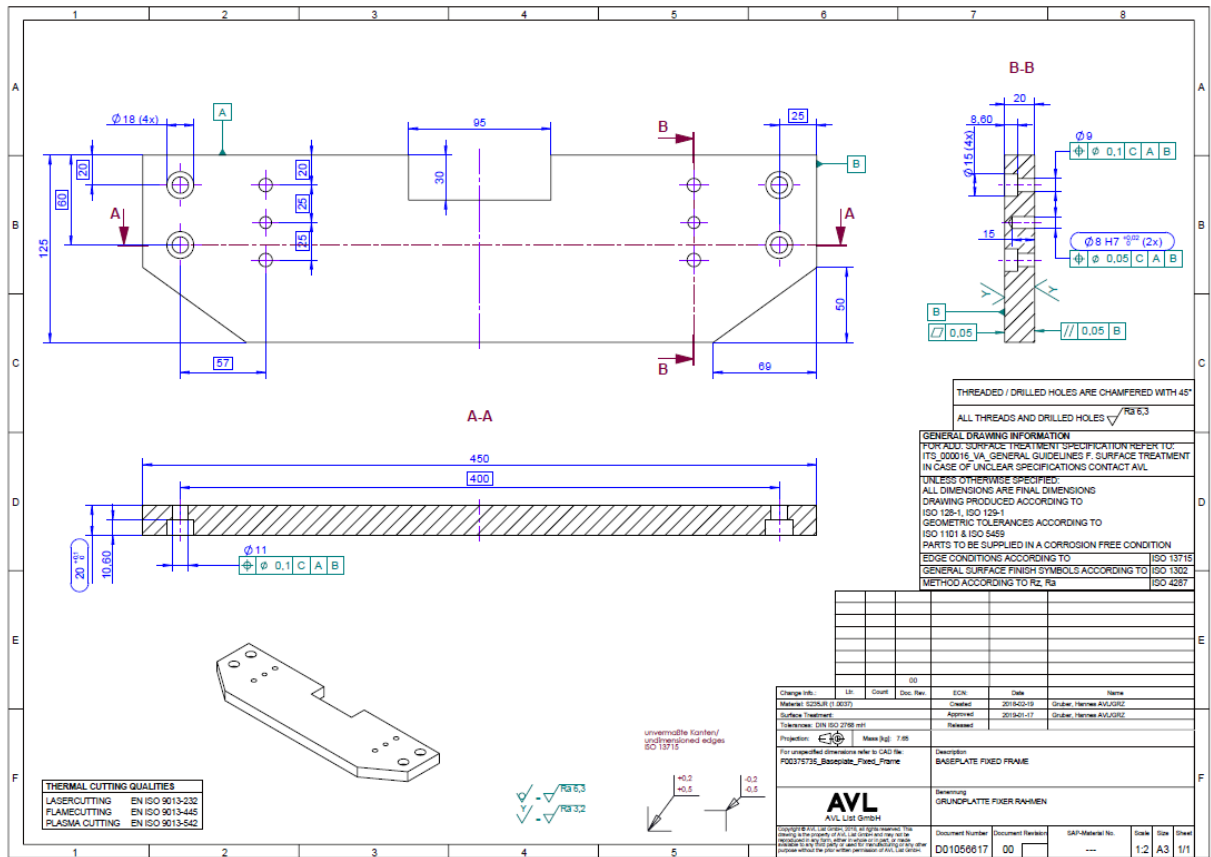
# Appendix

Item	Component	Component description	EPDM_DESCRIPTIONEN	Quantity	Material	Mass
10	---	CUSTOM SPINDLE EXISTING	CUSTOM SPINDLE EXISTING	2		
20	---	TIMKEN FRONTHUB EXISTING	TIMKEN FRONTHUB EXISTING	2		
30	---	BEARING SPACER EXISTING	BEARING SPACER EXISTING	1		
40	---	ADAPTERPLATE V2 EXISTING	ADAPTERPLATE V2 EXISTING	2		
50	---	FLYWHEEL V2 EXISTING	FLYWHEEL V2 EXISTING	2		
60	---	02_BASEPLATE03_EXISTING	02_BASEPLATE03_EXISTING	1		
70	---	FLYWHEEL CONNECTING FLANGE EXISTING	FLYWHEEL CONNECTING FLANGE EXISTING	1		
80	---	BASEPLATE FRAME	BASEPLATE FRAME	1	S235JR (1.0037)	7.65
90	---	BRACKET FRAME	BRACKET FRAME	4	S235JR (1.0037)	3.79
100	DM0225		Nut DIN 508 M10x12	22	Material <not specified>	0.02
110	DS0361		SCKT HD CAP SCR ISO 4762 M10X 25 8.8 ZN	8	8.8 zinc-plated	0.03
120	---	PLATE T NUT	PLATE T NUT	2	S235JR (1.0037)	16.17
130	DS4691		SCKT HD CAP SCR ISO 4762 M 8X 40 8.8FLZN	16	8.8 zinc-plated	0.02
140	---	Parallel pin ISO 8735 A 8m6x28	Parallel pin ISO 8735 A 8m6x28	8	Material <not specified>	0.01
150	---	BASEPLATE FRAME	BASEPLATE FRAME	1	S235JR (1.0037)	9.30
160	DS0512		SCKT HD CAP SCR ISO 4762 M 8X 20 8.8 ZN	8	8.8 zinc-plated	0.02
170	---	Hexagon socket head shoulder screw ISO 7379 10x25	Hexagon socket head shoulder screw ISO 7379 10x25	6	Material <not specified>	0.03
180	DM0098		HEX NUT ISO 4032 M 8 8 ZN	6	8 zinc-plated	0.01
190	DS0363		SCKT HD CAP SCR ISO 4762 M10X 30 8.8 ZN	5	8.8 zinc-plated	0.03
200	---	BRACKET LEDGE	BRACKET LEDGE	1	Material <not specified>	1.19
210	---	BRACKET LEDGE SIDE	BRACKET LEDGE SIDE	2	Material <not specified>	0.47
220	---	STIFFENER	STIFFENER	1	S235JR (1.0037)	4.49
230	---	MEASURING BRACKET	MEASURING BRACKET	1	S235JR (1.0037)	2.21
240	---	Hexagon socket head shoulder screw ISO 7379 10x40	Hexagon socket head shoulder screw ISO 7379 10x40	2	Material <not specified>	0.04
250	DS2051		SCKT HD CAP SCR ISO 4762 M10X150 12.9	4	12.9 blank	0.11
260	---	SPACER SIDE	SPACER SIDE	1	S235JR (1.0037)	21.73
270	DS2050		SCKT HD CAP SCR ISO 4762 M10X130 12.9	2	12.9 blank	0.09
280	---	MEASURING BRACKET BACK	MEASURING BRACKET BACK	1	S235JR (1.0037)	3.51
290	---	Hexagon socket head shoulder screw ISO 7379 10x50	Hexagon socket head shoulder screw ISO 7379 10x50	2	Material <not specified>	0.05
300	---	SPACER BACK	SPACER BACK	1	S235JR (1.0037)	16.34
310	---	MEASURING BOX U9C_20kN	MEASURING BOX U9C_20kN	4	Material <not specified>	0.11
320	---	KNUCKEL EYE U9 20kN	KNUCKLE EYE U9 20kN	4	Material <not specified>	0.08
330	---	SPANNER NUT	SPANNER NUT	4	Material <not specified>	0.05
340	---	RODEND M10 LEFTHAND	RODEND M10 LEFTHAND	4	Material <not specified>	0.07
350	DS4692		SCKT HD CAP SCR ISO 4762 M10X 25 8.8FLZN	8	8.8 zinc-plated	0.03

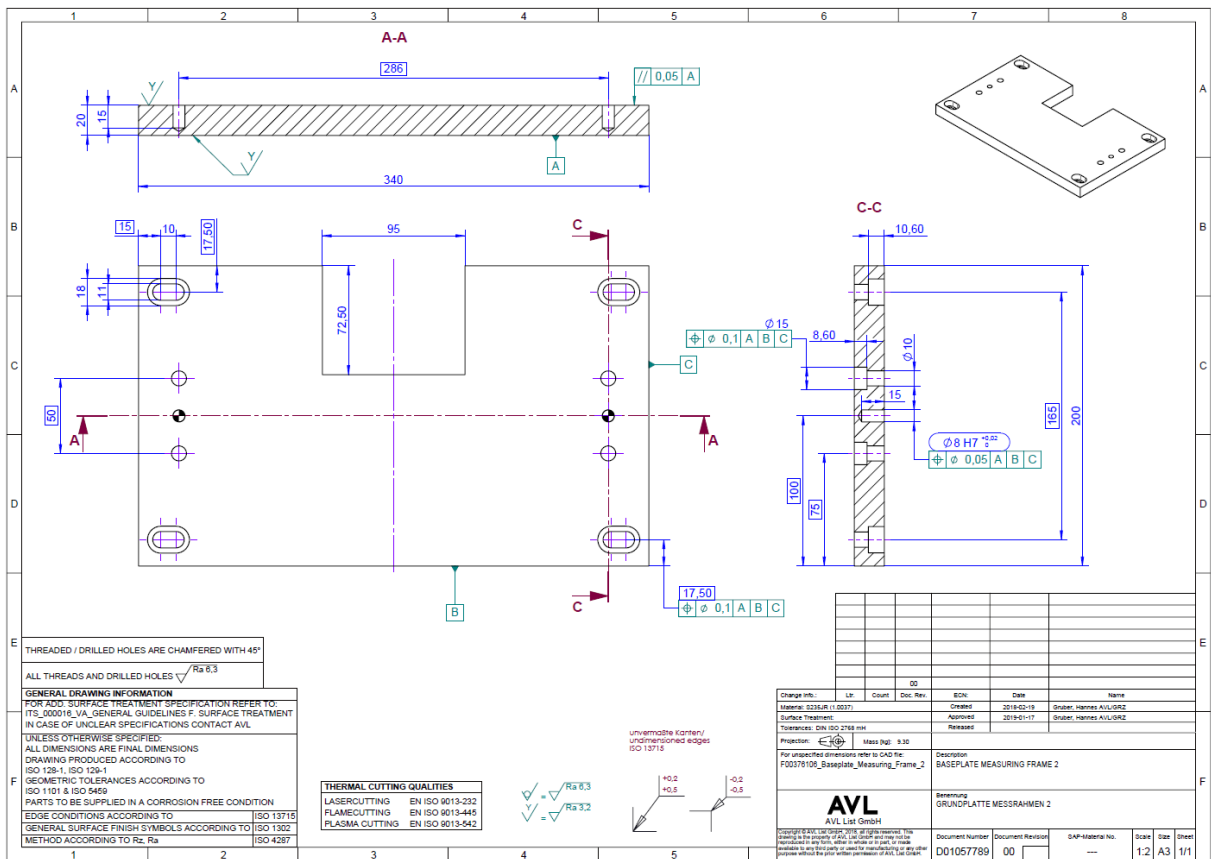
Appendix 4: Parts list frame assembly and rotor



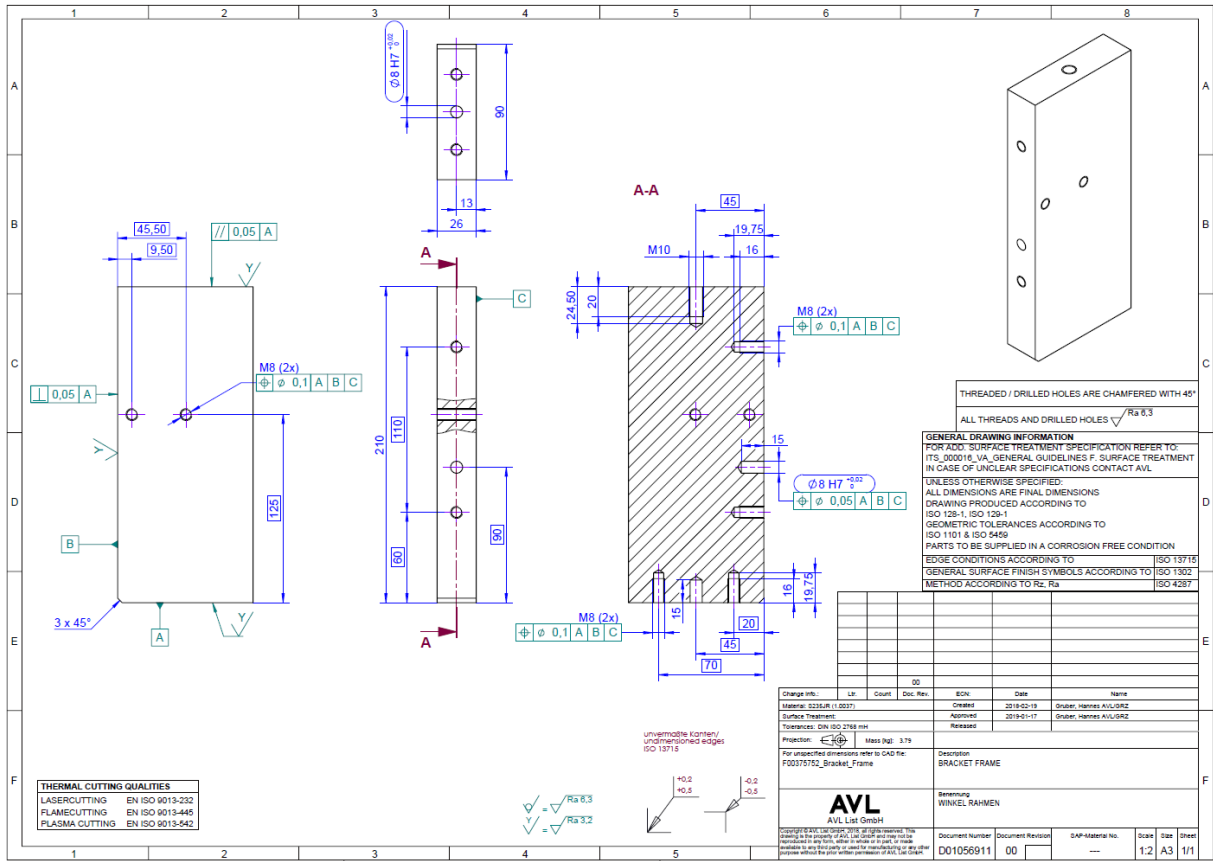




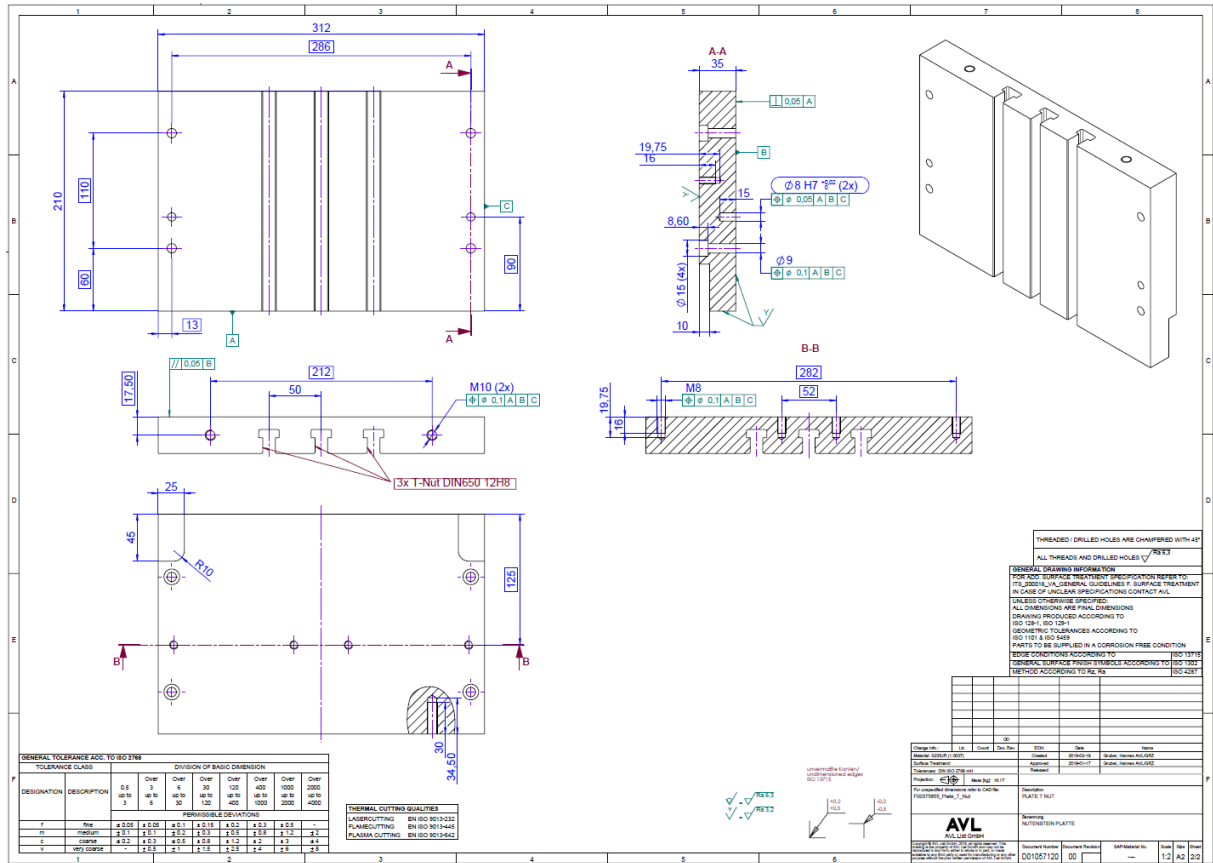
Appendix 7: Base plate locating frame



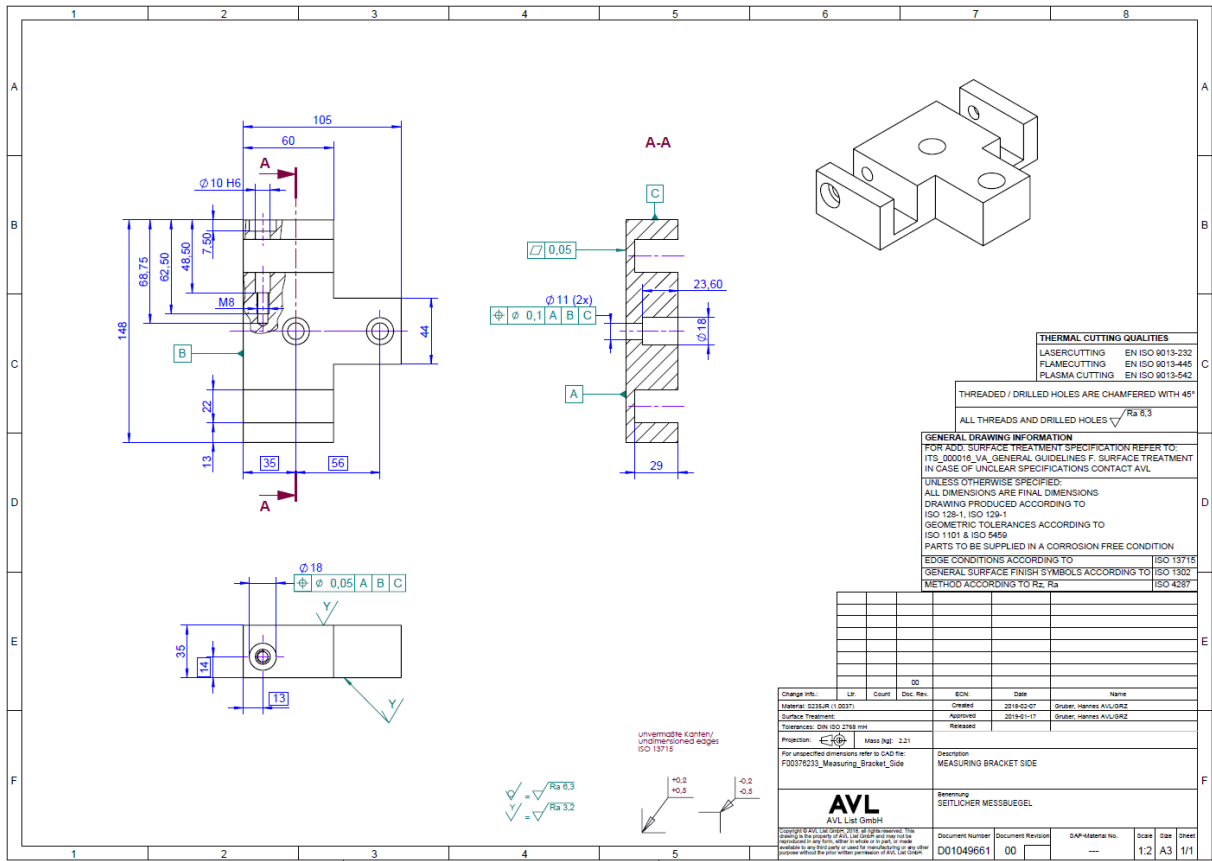
Appendix 8: Base plate adjustable frame



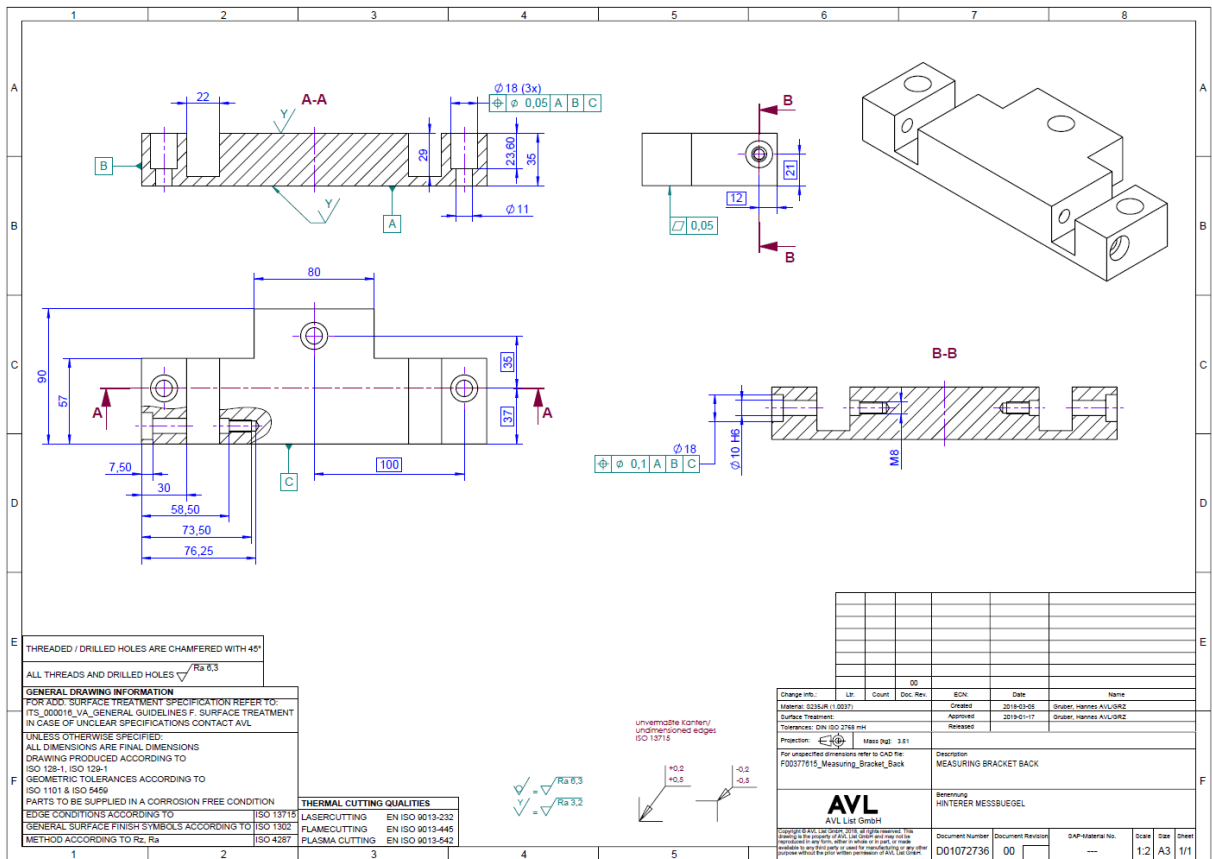
Appendix 9: Stiffener bracket left & right



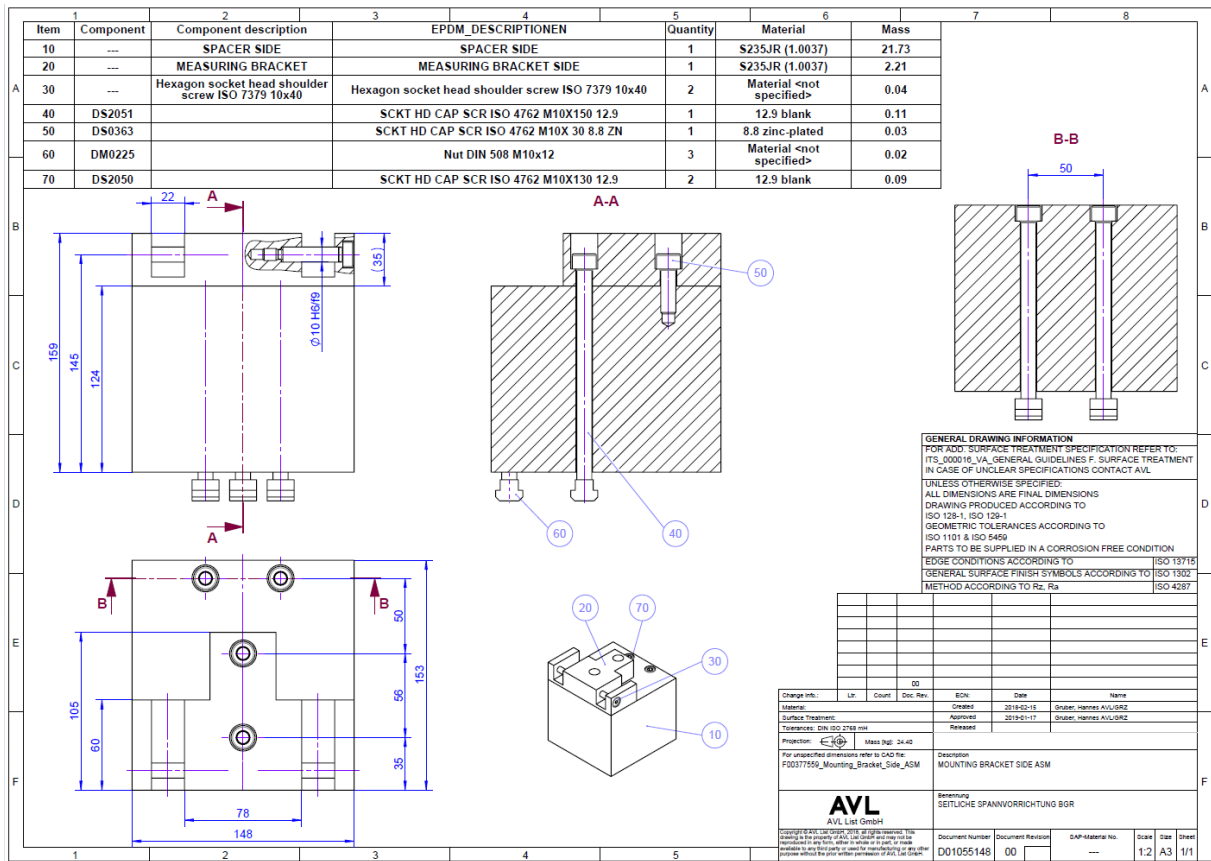
Appendix 10: T-nut back plate



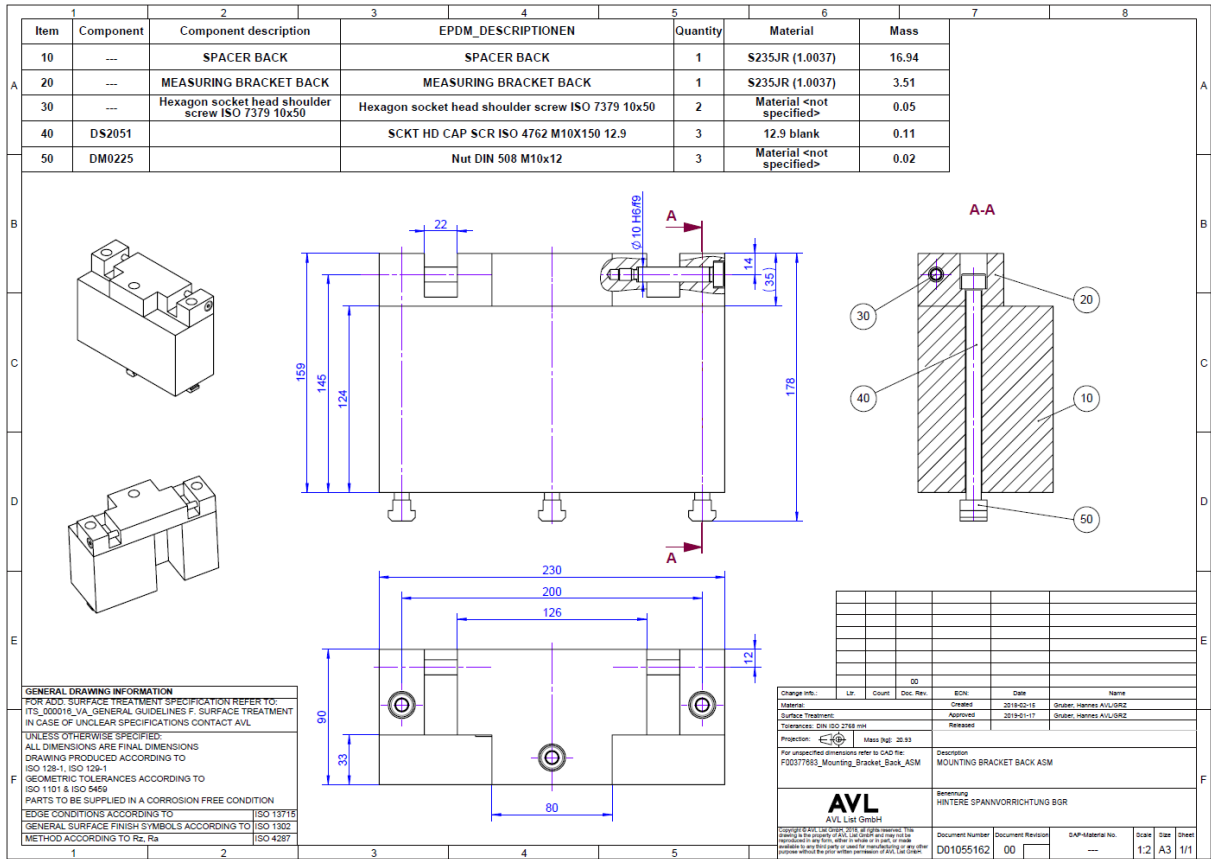
Appendix 11: Bracket for force application mechanism - radial



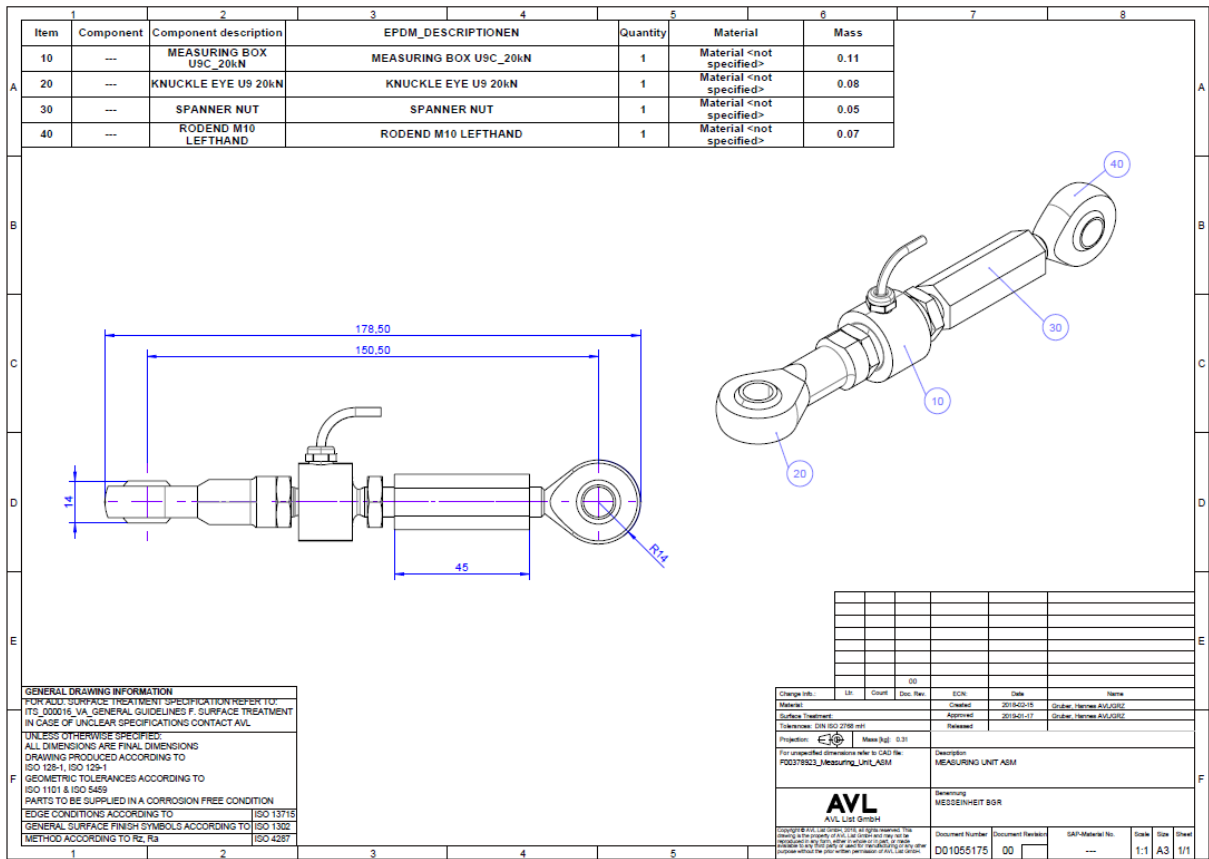
Appendix 12: Bracket for force application mechanism - axial



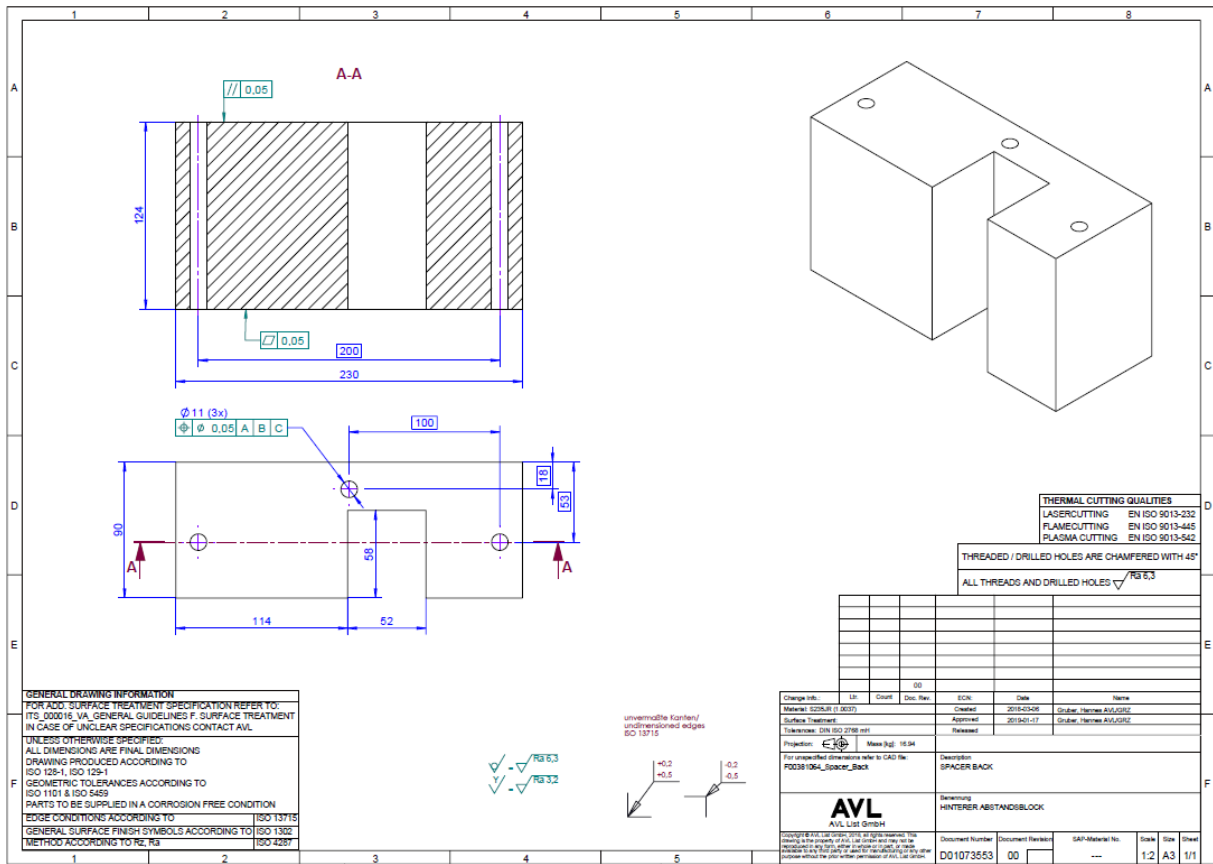
Appendix 13: Force application mechanism - radial assembly



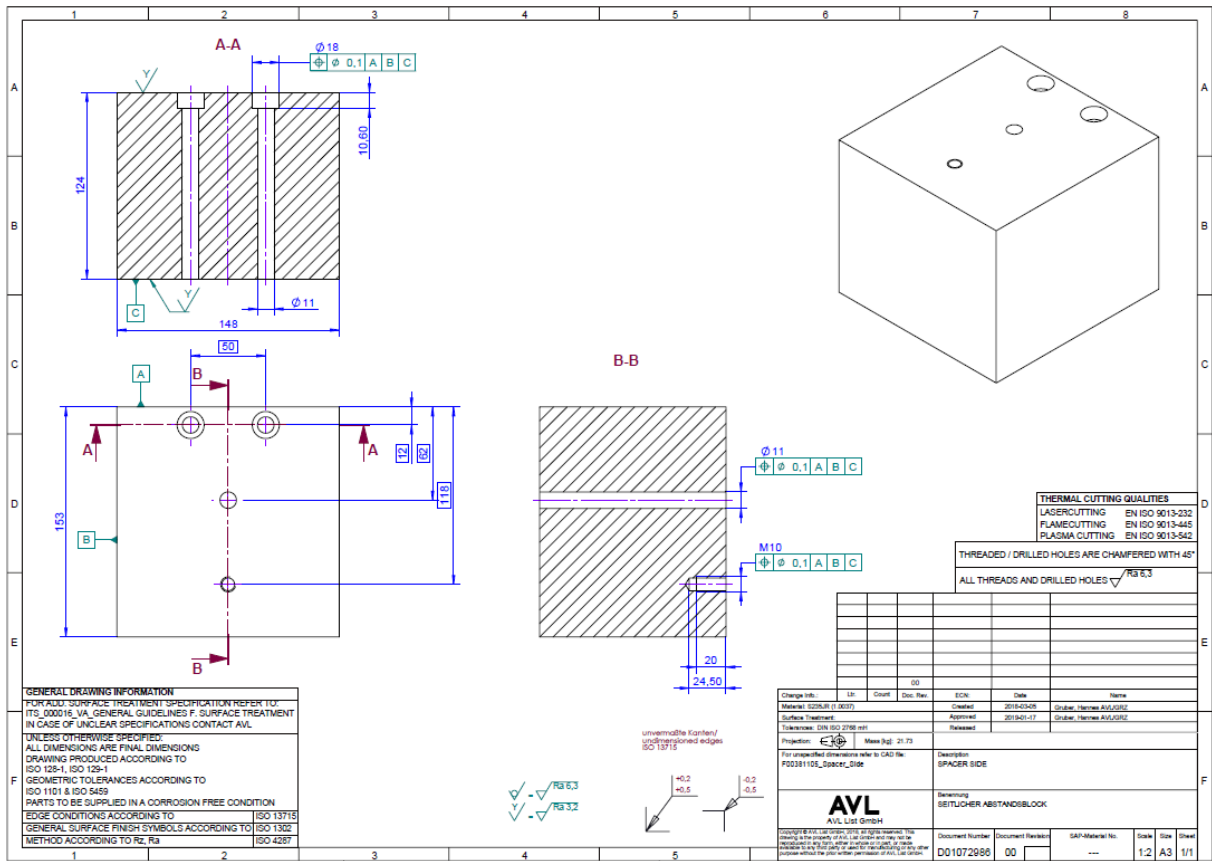
Appendix 14: Force application mechanism - axial



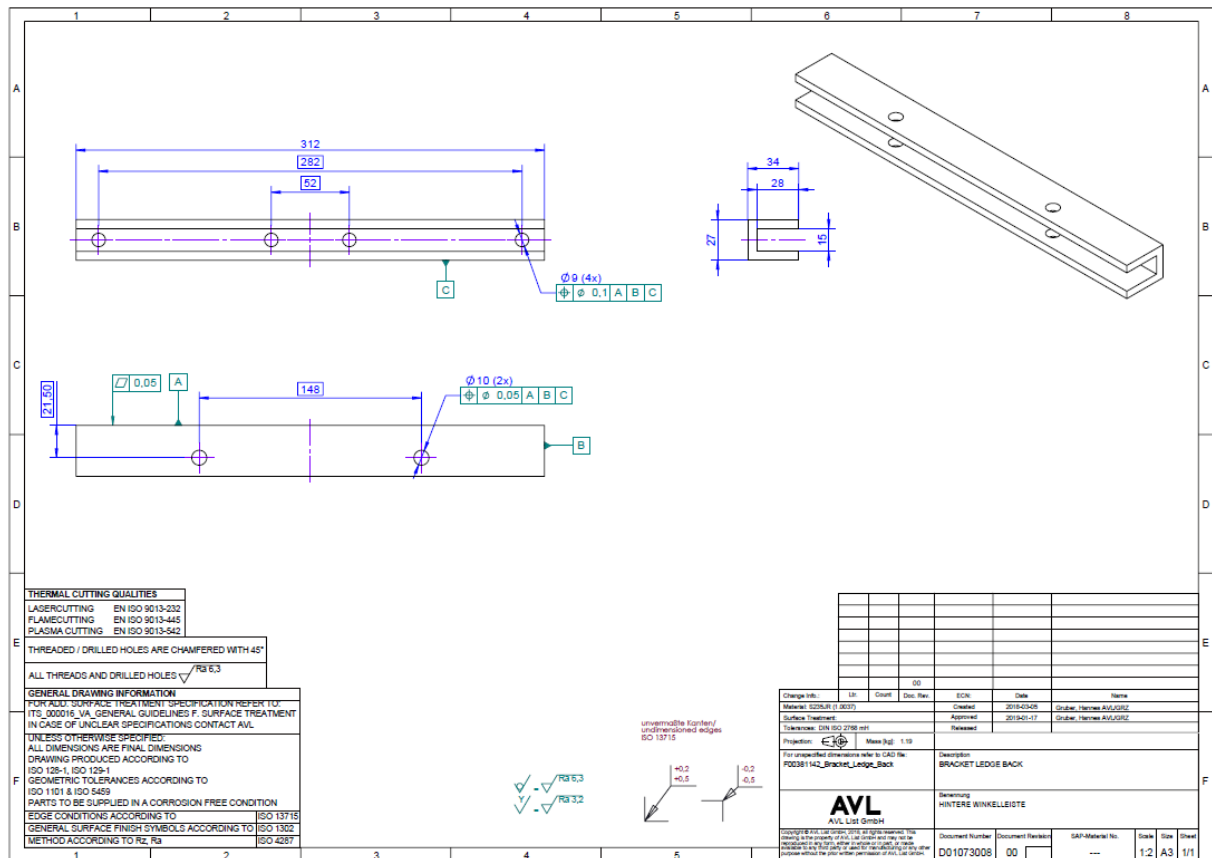
Appendix 15: Force measuring assembly



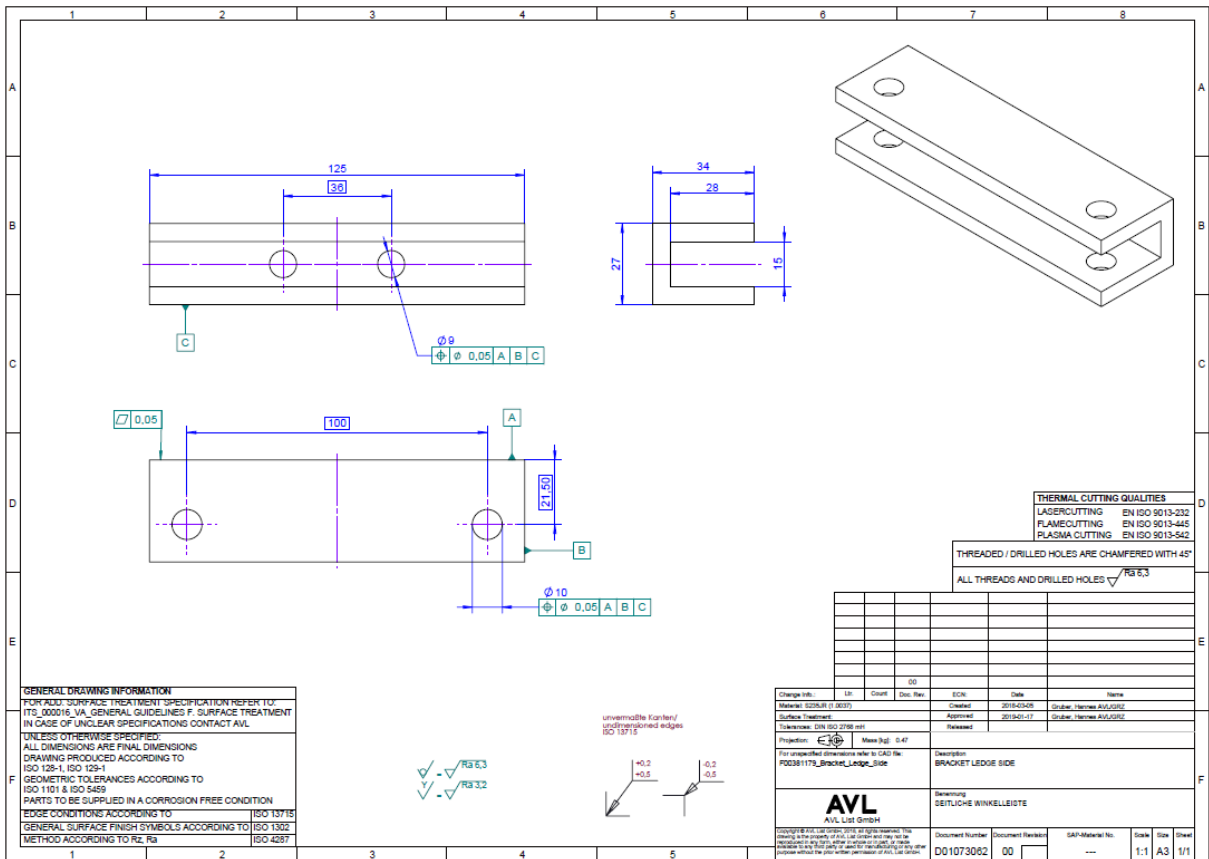
Appendix 16: Spacer force mechanism - axial



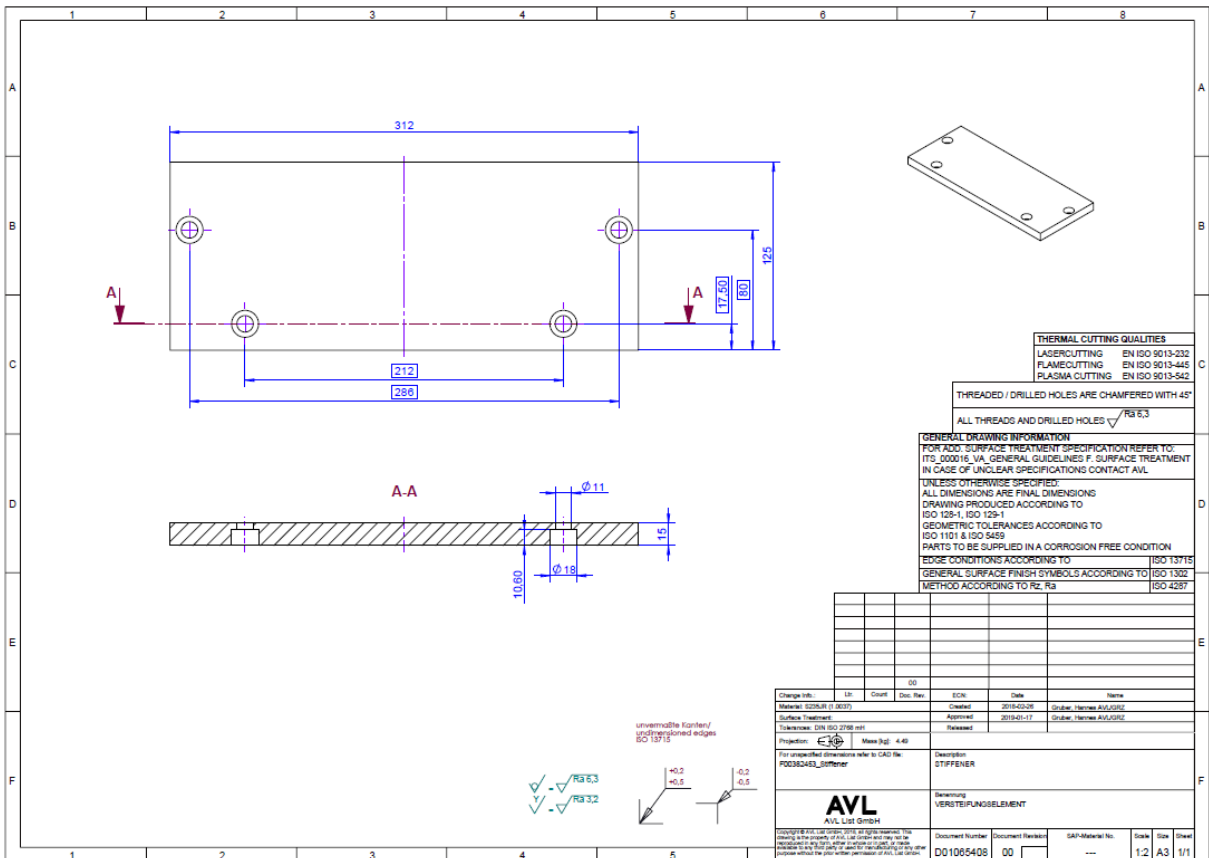
Appendix 17: Spacer force mechanism – radial



Appendix 18: Rail – axial

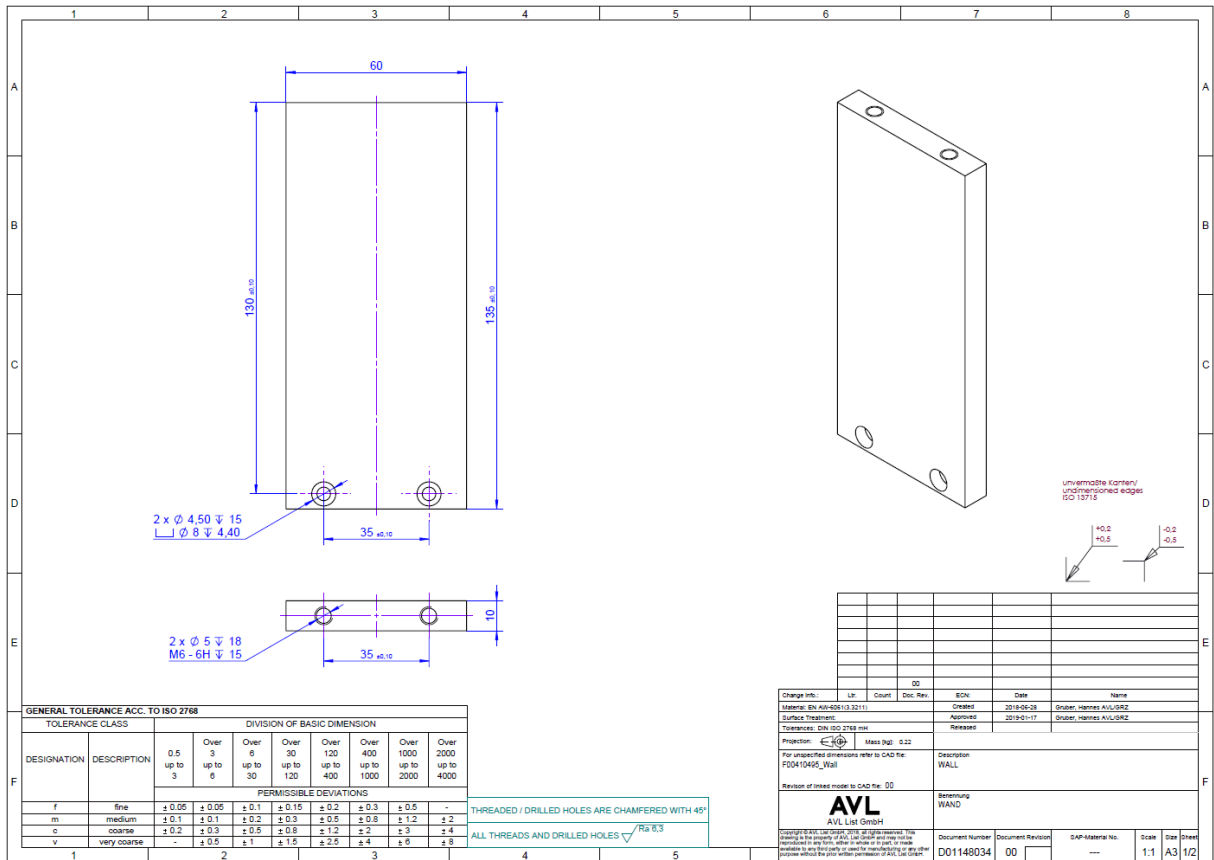


Appendix 19: Rail - radial

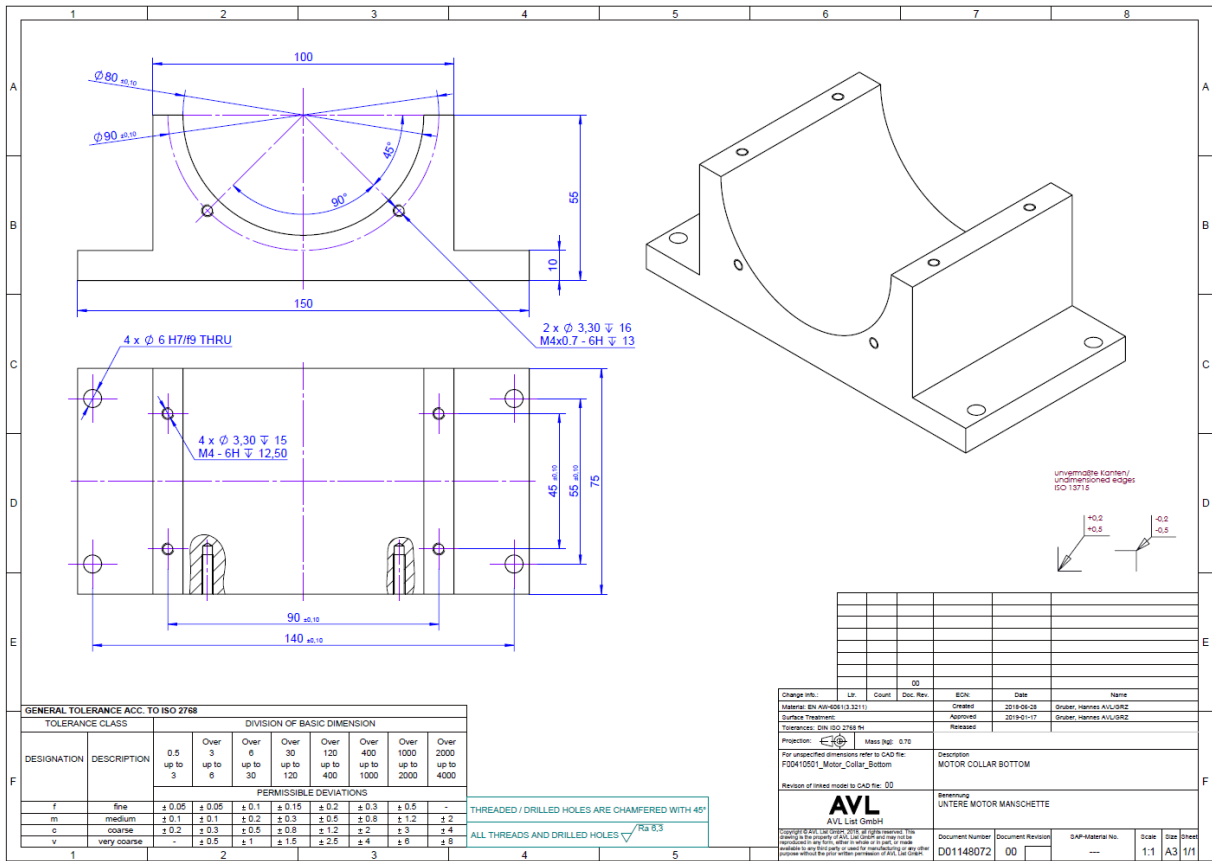


Appendix 20: Top plate

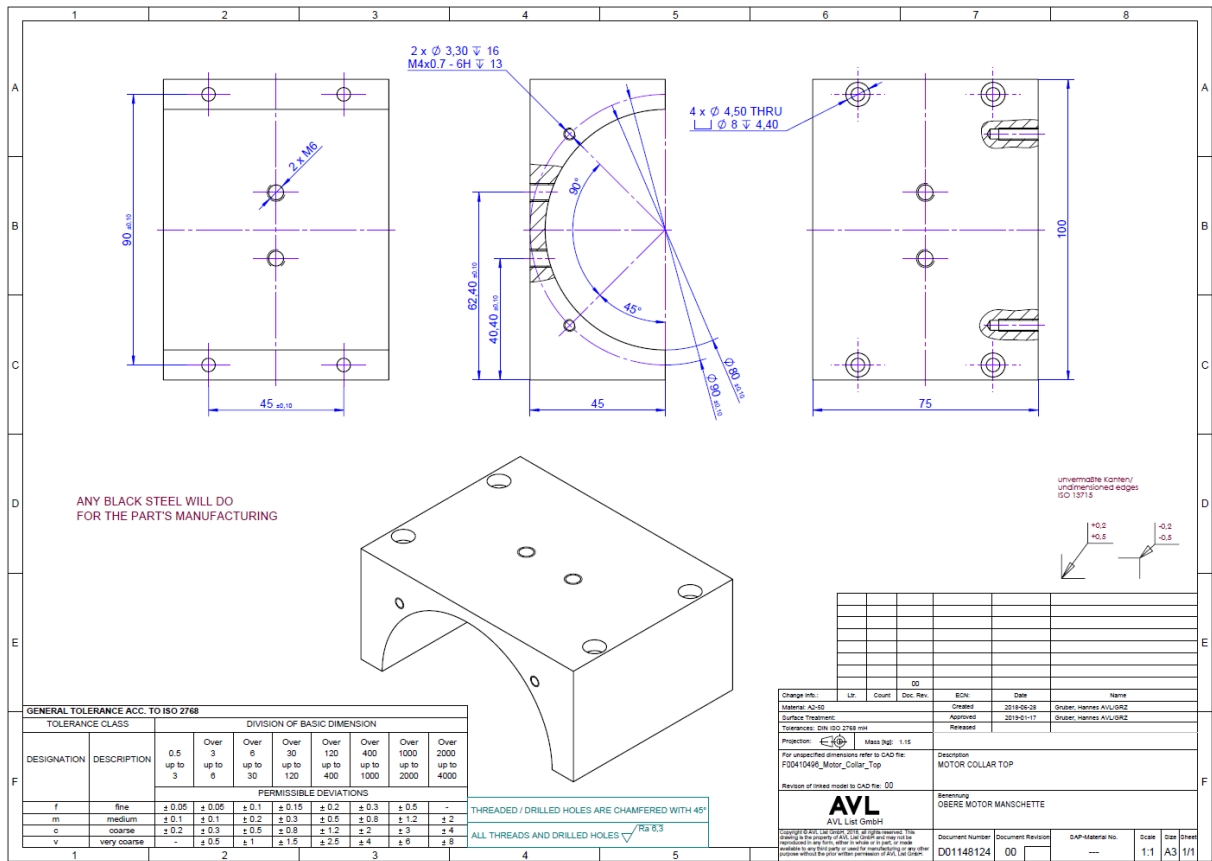
### A.1.2 Drive motor frame



Appendix 21: Side plate

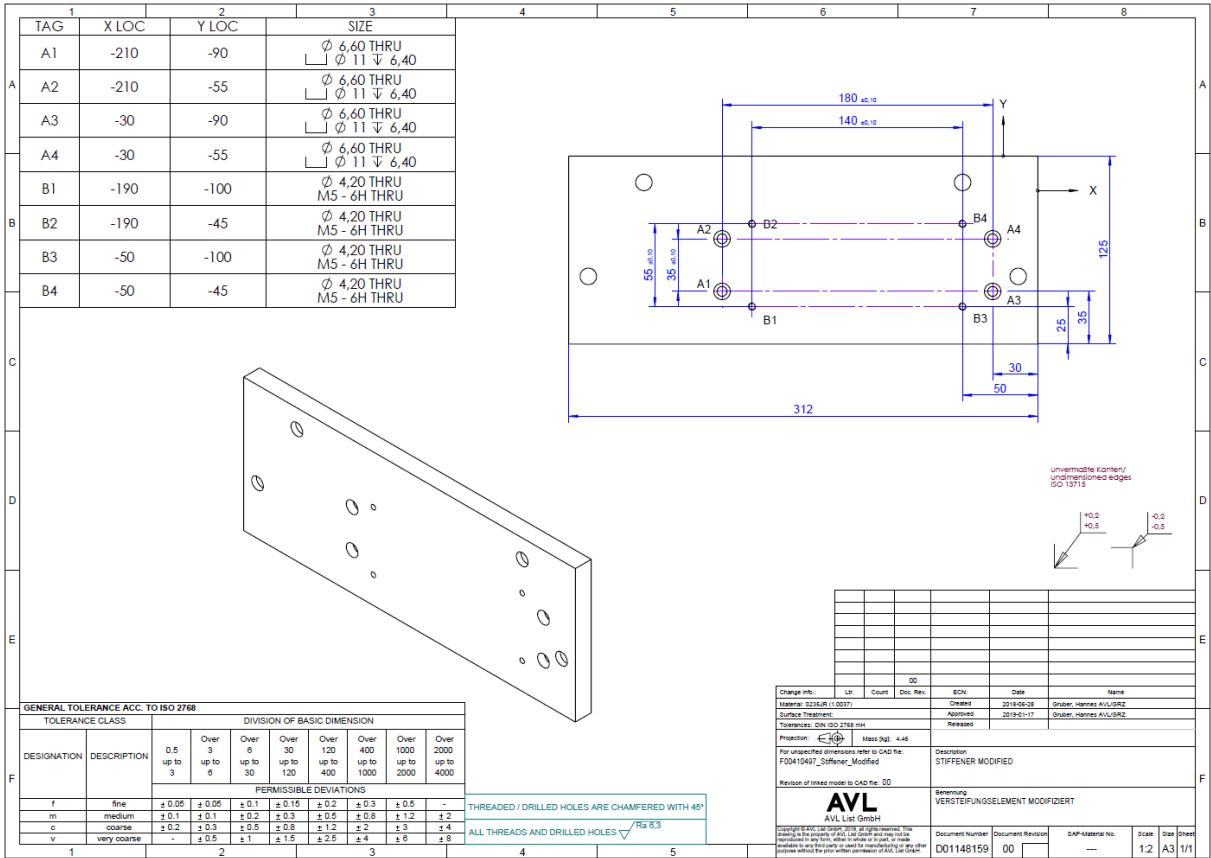


Appendix 22: Motor mounting bracket bottom

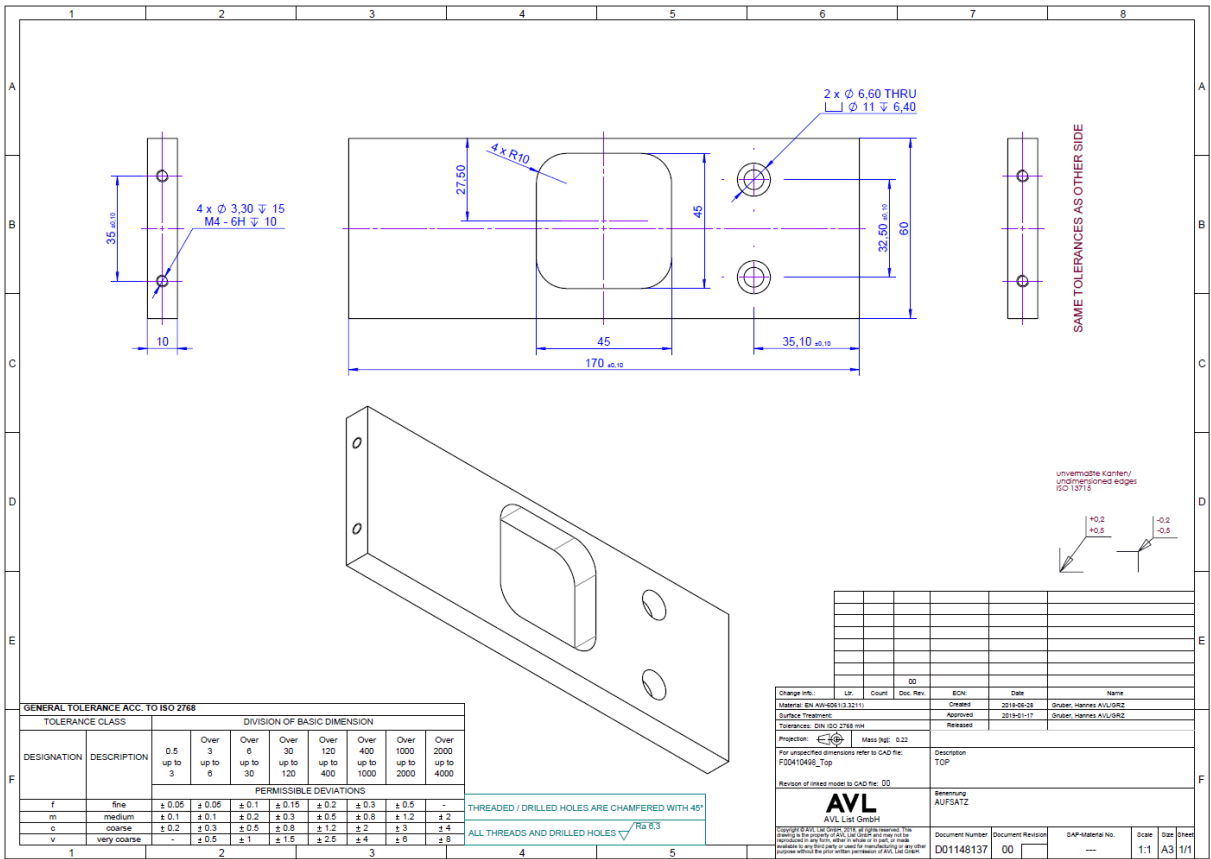


Appendix 23: Motor mounting bracket

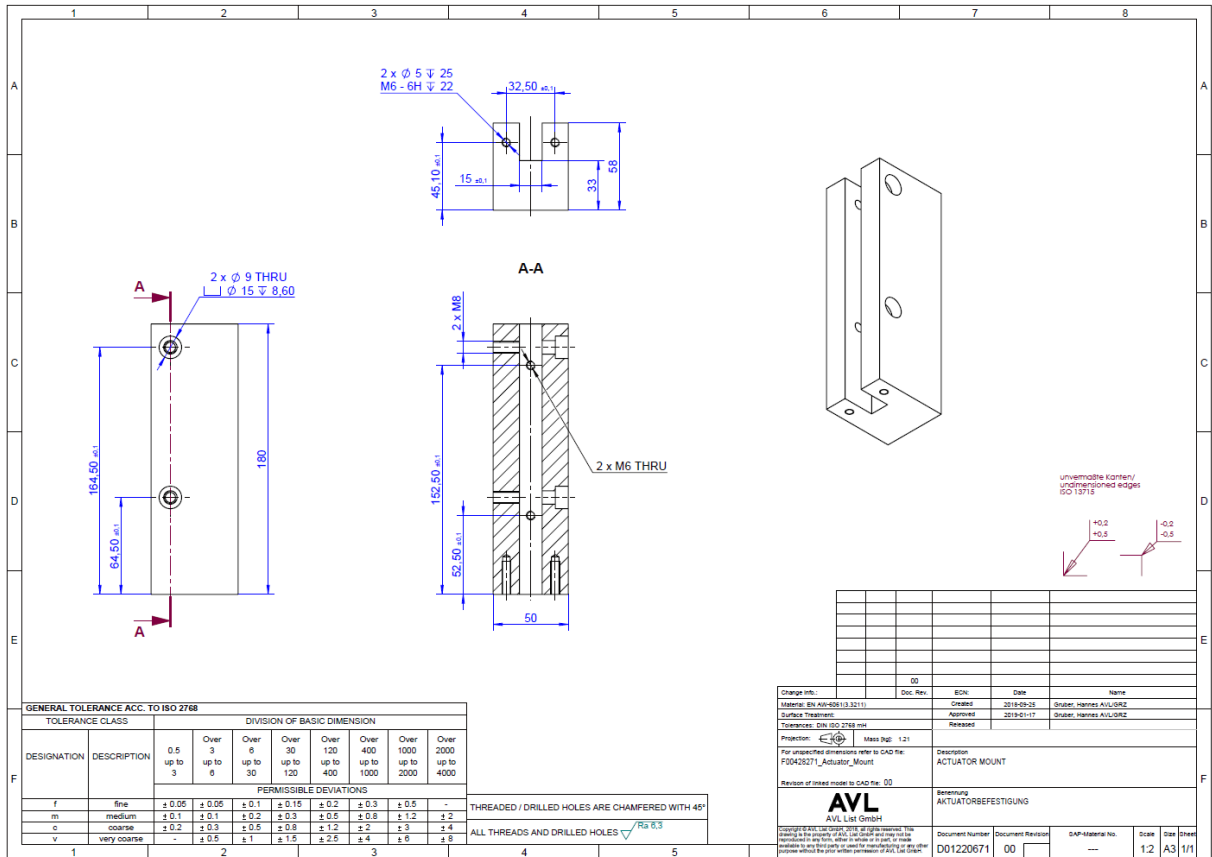
# Appendix



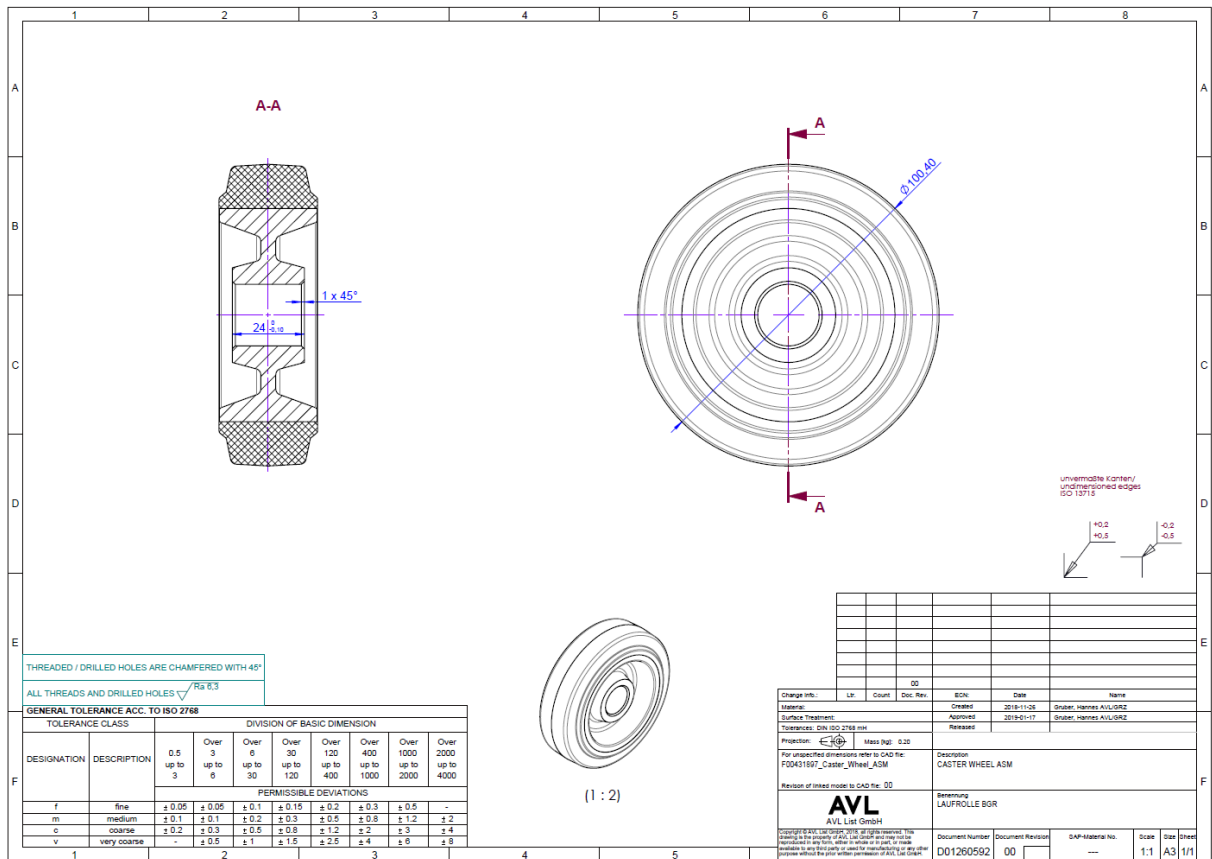
Appendix 24: Rework top plate



Appendix 25: Top plate motor mounting



Appendix 26: Actuator mount



Appendix 27: Friction wheel

## A.2 Datasheets

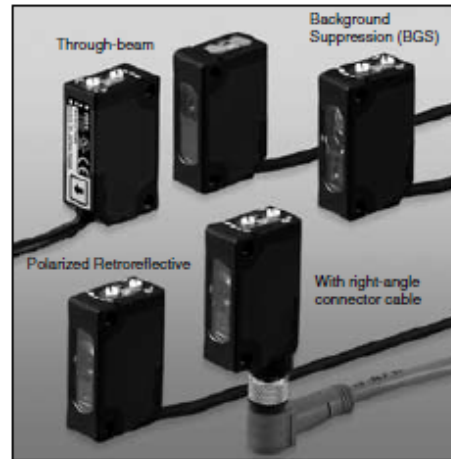
# SA1E-L

## Miniature Laser Photoelectric Switches (Built-in Amplifier)

**Class 1 laser.**

**Fastest response in its class. Reliably detects fast-moving objects.**

- Light source is a red laser (Class 1 by IEC60825-1, 2007).
- Laser beams with high degree of straightness achieve a long sensing range (30 m maximum).
- Response speed of 250  $\mu$ s is the fastest in its class. Reliably detects fast-moving small objects.
- The visible beam ensures easy and reliable positioning.
- IP67 structure can be used in environments exposed to dust or water. Operating temperature: 55°C maximum.
- Aligning the optical axis is easy because the lens unit is fixed on the housing (through-beam/polarized retroreflective).
- Light ON/Dark ON mode is selectable.
- Cable (1m, 2m, 5m cable) or M8 connector.
- CE marked.
- Compliant with Class 1 of FDA regulations (according to Laser Notice No. 50).



Package Quantity: 1

Sensing Method	Sensing Range	Connection	Cable Length	Part No.	
				NPN Output	PNP Output
Through-beam 	 See the characteristics on page 11.	Cable	1 m	SA1E-LTN3	SA1E-LTP3
			2 m	SA1E-LTN3-2M	SA1E-LTP3-2M
			5 m	SA1E-LTN3-5M	SA1E-LTP3-5M
		Connector	—	SA1E-LTN3C	SA1E-LTP3C
Polarized Retroreflective  (Note)	 See the characteristics on page 11.	Cable	1 m	SA1E-LPN3	SA1E-LPP3
			2 m	SA1E-LPN3-2M	SA1E-LPP3-2M
			5 m	SA1E-LPN3-5M	SA1E-LPP3-5M
		Connector	—	SA1E-LPN3C	SA1E-LPP3C
Background Suppression 	 See the characteristics on page 12.	Cable	1 m	SA1E-LBN3	SA1E-LBP3
			2 m	SA1E-LBN3-2M	SA1E-LBP3-2M
			5 m	SA1E-LBN3-5M	SA1E-LBP3-5M
		Connector	—	SA1E-LBN3C	SA1E-LBP3C

Note: Maintain at least the distance shown in the ( ) between the SA1E-L photoelectric switch and reflector. Reflectors are not supplied and must be ordered separately. See page 5.

### Technische Daten

Kategorie	Flugmodell Brushless Elektromotor
kV (U/min pro Volt)	185
Typ	Boost 180
Betriebsspannung	37 - 44,4 V/DC
Zellenzahl LiPo	10-12
Empf. Luftschraube	22x10"
Max. Strom	85 A
Wellen-Ø	10 mm
Länge	80 mm
Durchmesser	78 mm
Gewicht	1065 g
Herst.-Teilnr.	C5604



Appendix 29: Drive motor

### Technische Daten

Kategorie	Flugmodell Brushless Flugregler
Dauerstrom	150 A
Gewicht	123 g
Betriebsspannungsbereich	22.2 - 44.4 V
Zellenzahl LiPo	6 - 12
Belastbarkeit (max.)	180 A
Betriebsspannung max.	44.4 V
Betriebsspannung min.	22.2 V
Breite	47 mm
Höhe	16 mm
Länge	65 mm



Appendix 30: Motor controller

## Programmierbox S-CON Regler

### Beschreibung

---

Die S-CON Programmierbox besitzt folgende Grundfunktionen:

1. Einstellung der S-CON Reglerfunktionen
2. Auslesen der Flugdaten (Data Logging)
3. Nutzung als USB Adapter um den Regler mit dem PC zu verbinden
4. Firmware Update (sofern verfügbar)

### Lieferumfang

---

- Programmierbox
- Anleitung.

### Technische Daten

---

Kategorie	Programmierbox
Passend für	S-CON-Regler Serie
Herst.-Teilenr.	C6836



Appendix 31: Motor controller programming device

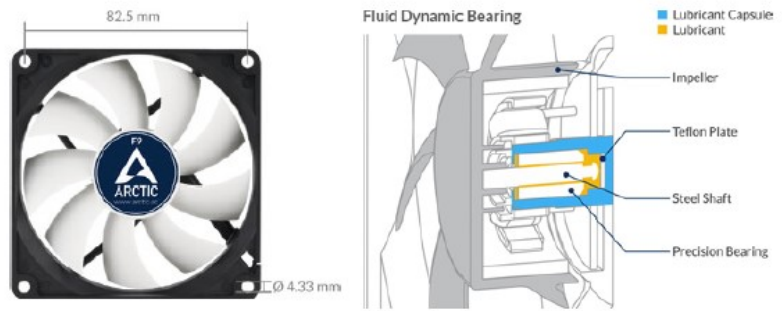
## Technische Daten

Technologie	LiPo
Zellen-Zahl	5
Spannung	18.5 V
Kapazität	5000 mAh
Belastbarkeit	20 C
Gewicht	585 g
Stecksystem	EC5
Balancer-Stecksystem	XH
Bauform	Softcase
Breite	43 mm
Herst.-Teilenr.	25000531
Höhe	48 mm
Inhalt	1 St.
Kategorie	Modellbau-Akkupack (LiPo)
Länge	138 mm



Appendix 32: Accumulator

Fan



Performance

Fan Speed:	1,800 RPM (@ 12V DC) 1,200 RPM (@ 7V DC) 800 RPM (@ 5V DC)
Air Flow:	43 CFM / 73.1 m <sup>3</sup> /h (@ 1,800 RPM)
Noise Level:	0.4 Sone (@ 1,800 RPM)

Electrical Characteristics

Typical Voltage:	12V DC
Start-up Voltage:	2.6V DC
Cable Length:	400 mm

Voltage	Current
12V DC (Nominal)	0.16A
7V DC	0.11A
5V DC	0.09A

Connection

Motherboard: +12V DC  
3-pin socket



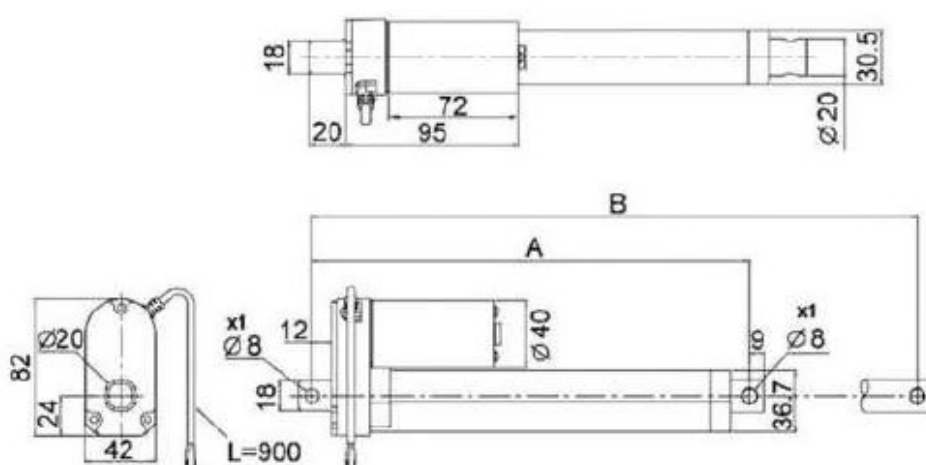
Size & Weight

Appendix 33: Cooling fan

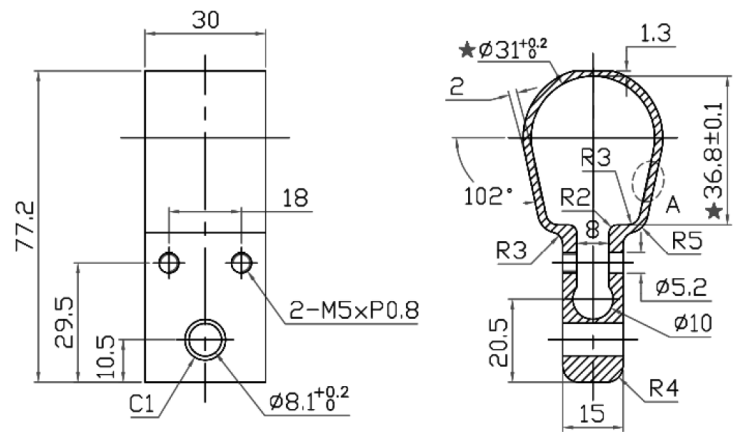
## Linear Elektrozyylinder DSZY1

### Technische Daten

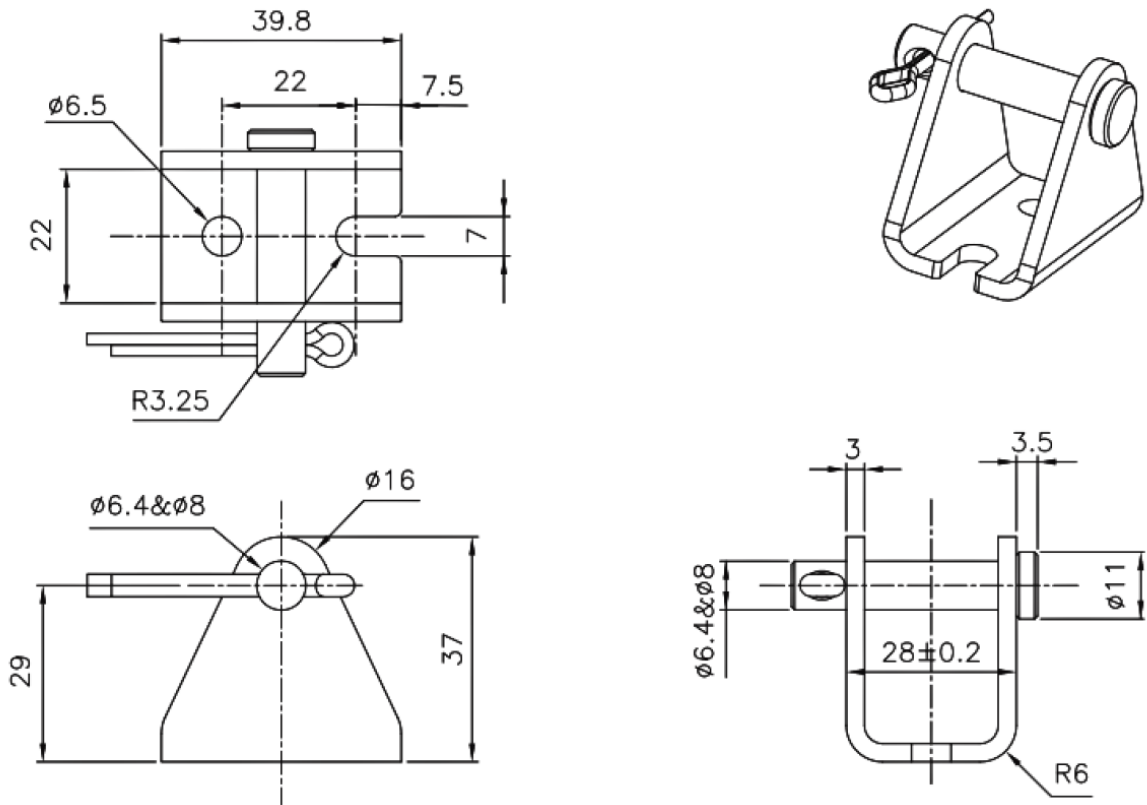
Herst.-Teilnr.:	12393
Typ	DSZY1-12-40-A-100-IP65
Geschwindigkeit (max.)	8 mm/s
Hublänge	100 mm
Kategorie	Elektrozyylinder
Nennspannung	12 V/DC
Schubkraft	1000 N



Appendix 34: Electric cylinder



Appendix 35: Motor mounting clamp



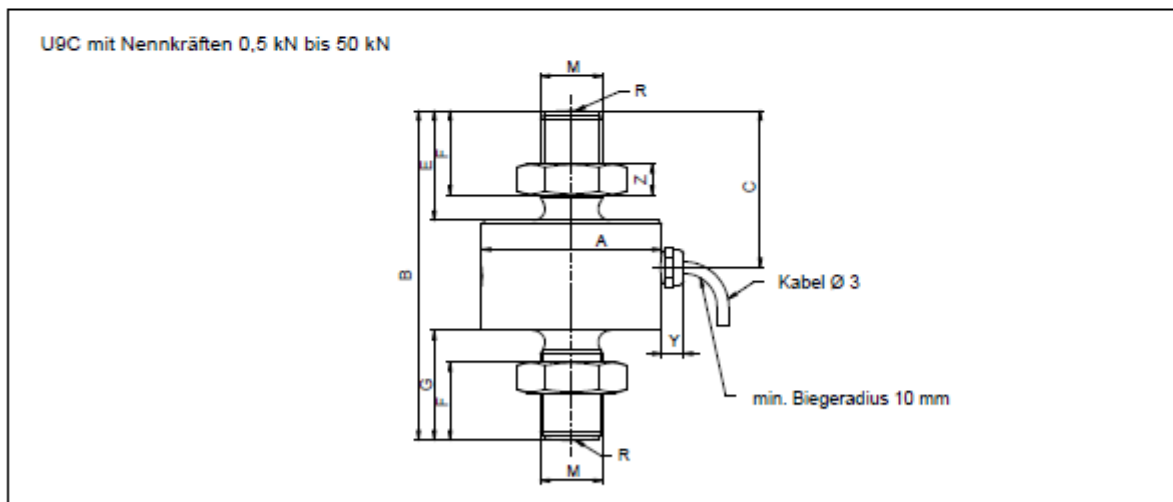
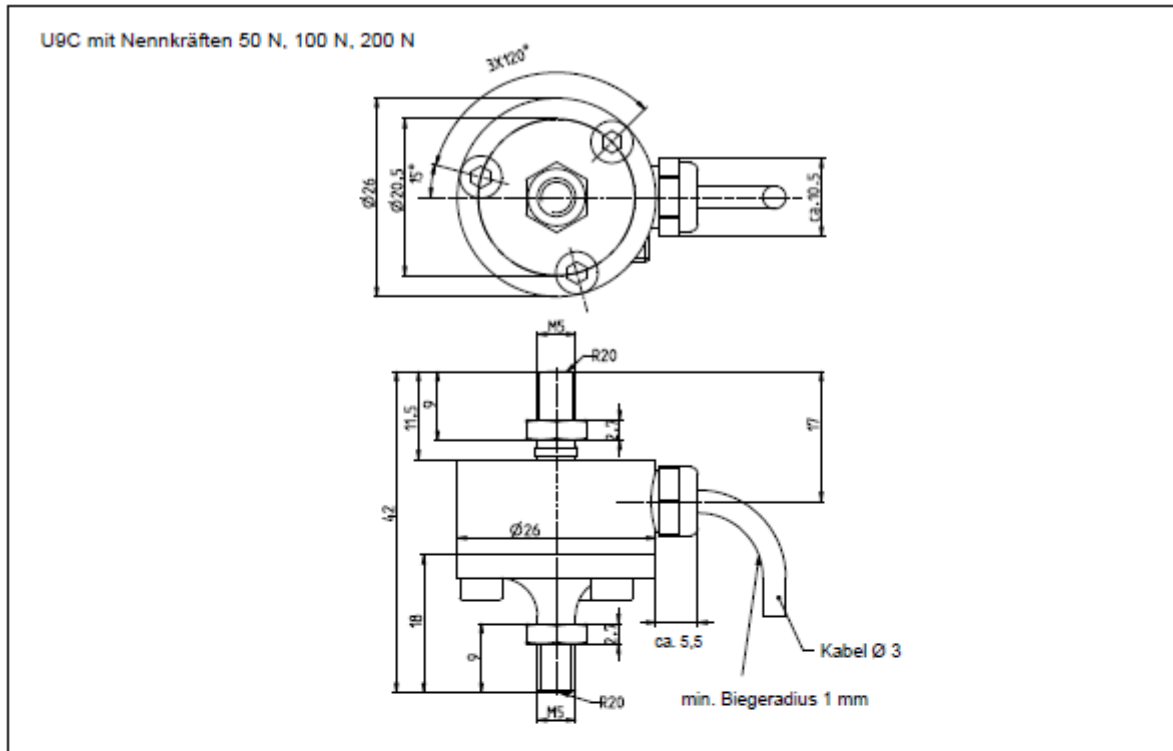
Appendix 36: Motor connecting bracket

## Technische Daten

Ausführung	V-Charge 100 Duo
Betriebsspannung	11 - 18 V/DC 100 - 240 V/AC
Ladeleistung max.	100 W
Ladestrom (max.)	10 A
Entladeleistung max.	10 W
Entlade-Strom	5 A
Ladekanäle/ -schächte	2
Stecksystem	4 mm
Balancer-Stecksystem	XH
Betriebsspannung	12 V 230 V
Breite	115 mm
Geeignet für (Zellenzahl LiPo/LiIon/LiFe) (max.)	6
Geeignet für (Zellenzahl LiPo/LiIon/LiFe) (min.)	1
Geeignet für (Zellenzahl NiCd/NiMH) (max.)	15
Geeignet für (Zellenzahl NiCd/NiMH) (min.)	1
Geeignet für Blei-Akku (max.)	20 V
Geeignet für Blei-Akku (min.)	2 V
Gewicht	1000 g
Herst.-Teilnr.	1388391
Höhe	63 mm
Kategorie	Modellbau-Multifunktionsladegerät
Länge	143 mm



Appendix 37: Battery charger



Nennkraft der U9C	A <sub>0,1</sub>	B	C	E	F	G	M	R	Y	Z
	[mm]									
0,5kN bis 1kN	26	44,5	29,5	13	9,9	13,5	M5	20	ca. 5,5	2,7
2kN bis 20kN	26	60	28,5	21	16	21	M10	40	ca. 5,5	5
50kN	46	84	40	28	21,5	28	M16x1,5	80	ca. 5,5	8

Appendix 38: Main dimensions - Load Cell

Nennkraft	F <sub>nom</sub>	N kN	50	100	200								
						0,5	1	2	5	10	20	50	
<b>Genauigkeit</b>													
Genauigkeitsklasse			0,2										
relative Spannweite in unveränderter Einbaulage	b <sub>rg</sub>	%	< 0,2										
relative Umkehrspanne	v <sub>0,5</sub>	%	< 0,2										
Linearitätsabweichung	d <sub>lin</sub>	%	< 0,2										
relatives Kriechen (30 min)	d <sub>cr,F</sub>	%	< 0,2					< 0,1					
Biegemomenteinfluss bei 10% F <sub>nom</sub> * 10mm (typisch)	d <sub>Mb</sub>	%	0,055		0,045		2,35			2,45		0,5	
<b>Temperatureinfluss auf den Kennwert</b>													
im Nenntemperaturbereich	TK <sub>C</sub>	%/10K	0,2										
im Gebrauchstemperaturbereich	TK <sub>C</sub>	%/10K	< 0,5										
<b>Temperatureinfluss auf das Nullsignal</b>													
im Nenntemperaturbereich	TK <sub>0</sub>	%/10K	< 0,2										
im Gebrauchstemperaturbereich	TK <sub>0</sub>	%/10K	< 0,50										
<b>Elektrische Kennwerte</b>													
Nennkennwert	C <sub>nom</sub>	mV/V	1										
relative Abweichung des Nullsignals	d <sub>s,0</sub>	mV/V	+/- 0,2										
Kennwertabweichung	d <sub>c</sub>	%	< +/-1 Zug , < +/-2 Druck										
Kennwertunterschied Zug/Druck	d <sub>zd</sub>	%	< 2										
Eingangswiderstand	R <sub>e</sub>	Ω	250 - 400					300 - 450					
Ausgangswiderstand	R <sub>a</sub>	Ω	200 - 400					145 - 450					
Isolationswiderstand	R <sub>is</sub>	Ω	> 1*10 <sup>9</sup>										
Gebrauchsbereich der Speisespannung	B <sub>u,gt</sub>	V	0,5...12										
Referenzspeisespannung	U <sub>ref</sub>	V	5										
Anschluss			4-Leiterschaltung										
<b>Temperatur</b>													
Referenztemperatur	t <sub>ref</sub>	°C	23										
Nenntemperaturbereich	B <sub>t,nom</sub>	°C	-10...+70										
Gebrauchstemperaturbereich	B <sub>t,g</sub>	°C	-30...+85										
Lagertemperaturbereich	B <sub>t,l</sub>	°C	-30...+85										
<b>Mechanische Kenngrößen</b>													
maximale Gebrauchskraft	F <sub>G</sub>		200					150					
Grenzkraft	F <sub>L</sub>	% von F <sub>nom</sub>	>200					> 150					
Bruchkraft	F <sub>B</sub>		> 400										
Grenzdrehmoment		Nm	1,7	3,4	2,5	3,7	4,5	28	23	11	11	35	
Grenzbiegemoment bei Belastung mit Nennkraft		Nm	0,17	0,7	1,5	3,7	3,8	10,2	14,4	8,2	8,6	28,5	
statische Grenzquerkraft bei Belastung mit Nennkraft <sup>2)</sup>	F <sub>q</sub>	% von F <sub>nom</sub>	100					50	100	50	18	6	8
Nennmessweg		mm	0,008					0,018		0,03	0,05	0,09	0,14
Grundresonanzfrequenz		kHz	8,5	9,1	12,8	15,3	15,9	13,2	14,5	14,8	14,6	7,2	
relative Schwingbreite		% von F <sub>nom</sub>	70					80					70
<b>Allgemeine Angaben</b>													
Schutzart nach EN 60529 <sup>1)</sup>			IP67										
Federkörperwerkstoff			Stahl										
Vergussmasse			Silikon										
Kabel			Vierleiterschaltung, PUR - Isolierung										
Kabellänge		m	1,5, 3, 7, 12										
Gewicht		g	75					100					400

Appendix 39: Datasheet - Load cell

## Technische Daten

Typ	LCV-U10	LCV-U5	LCV-I0	LCV-I4	LCV-I10	LCV-I12
Art.-Nr.	100430	100626	101177	100432	100956	101018
Ausgang	±10V	±5V	0 .. 20 mA	4 .. 20 mA	10±10 mA	12±8 mA

### Auswerteseite

Versorgung	Versorgungsspannung Restwelligkeit Stromaufnahme	12 .. 28VDC <10% ≤70 mA
Signalausgang	Ausgangssignal U-Out Restwelligkeit Verstärkungsdrift Nullpunktdrift Linearität Ausgangswiderstand	±5V / ±10V ≤2 mA <10 mV <0,015%/10 K <0,015%/10 K <0,02% <1 Ω
Signalausgang	Ausgangssignal I-Out Restwelligkeit bei 400 Ω Verstärkungsdrift Nullpunktdrift Linearität	0 .. 20 mA an 0 .. 400 Ω <10 mV <0,02%/10 K <0,02%/10 K <0,02%
Allgemein	Kabellänge LCV- Auswertung	U5/U10 3 m (max.10 m) I0/I4/I10/I12 3 m (max.100 m)

### Sensorseite

Versorgung	Sensorspeisung TK Versorgungsspannung	5V ≤20 mA kurzschlussfest <25 ppm/K
Signaleingang	Sensor Empfindlichkeit Eingangswiderstand	0,35 .. 3,5 mV/V 10 <sup>9</sup> Ω
Allgemein	Kabellänge LCV-Sensor	1 m (max. 3 m)

### Sonstiges

Grenzfrequenz	1 kHz -3 dB
Nenntemperaturbereich	10 .. 50°C
Gebrauchstemperaturbereich	0 .. 60°C
Lagerungstemperaturbereich	-10 .. 70°C
Maße (Ø x L)	25 x 115 mm (inkl. Verschraubung)
Schutzart	IP67

### Optionen/ Zubehör

Art.-Nr.	Typ	Bezeichnung
110564	mV/V	mV/V justierter Nennkennwert
113512	2,5±2,5V	Ausgangssignal 2,5±2,5V
110651	5±5V	Ausgangssignal 5±5V
103760	LCV/KS	Kontrollsignalansteuerung extern 5 .. 28VDC
100563	LCV/50Hz	Filter 50 Hz -3 dB
112712	LCV/R	Messbereichswiderstand
108200	5 kHz -3 dB	Erhöhte Dynamik 5kHz -3 dB
108533	10 kHz -3 dB	Erhöhte Dynamik 10kHz -3 dB

### LiPo Lade- und Transporttasche

#### Beschreibung

"Safety First" die sichere Methode für die Aufbewahrung und den Transport Ihres LiPo Akkus. Schwer entflammbares Glasfaser-Material. Auch zum Laden geeignet.

#### Lieferumfang

- Tasche.

#### Technische Daten

Breite	80 mm
Höhe	80 mm
Kategorie	LiPo-Safety-Bag
Länge	190 mm



Appendix 41: LiPo Safebag

### Ausführung

---

- Alterungsbeständig
- Geringes Gewicht
- Einfache Handhabung
- Nachrüstbar und Wartungsfrei
- Sehr gute Flüssigkeitsbindung
- Säure- und laugenfest
- 100% anorganisch inert, reaktionsarm
- Geringes Gewicht (niedrige Deponiekosten von kontaminiertem Material)
- Geringe Wärmeleitung
- Schallschluckend
- Unverderblich
- Bakterien- und keimfrei.

### Lieferumfang

---

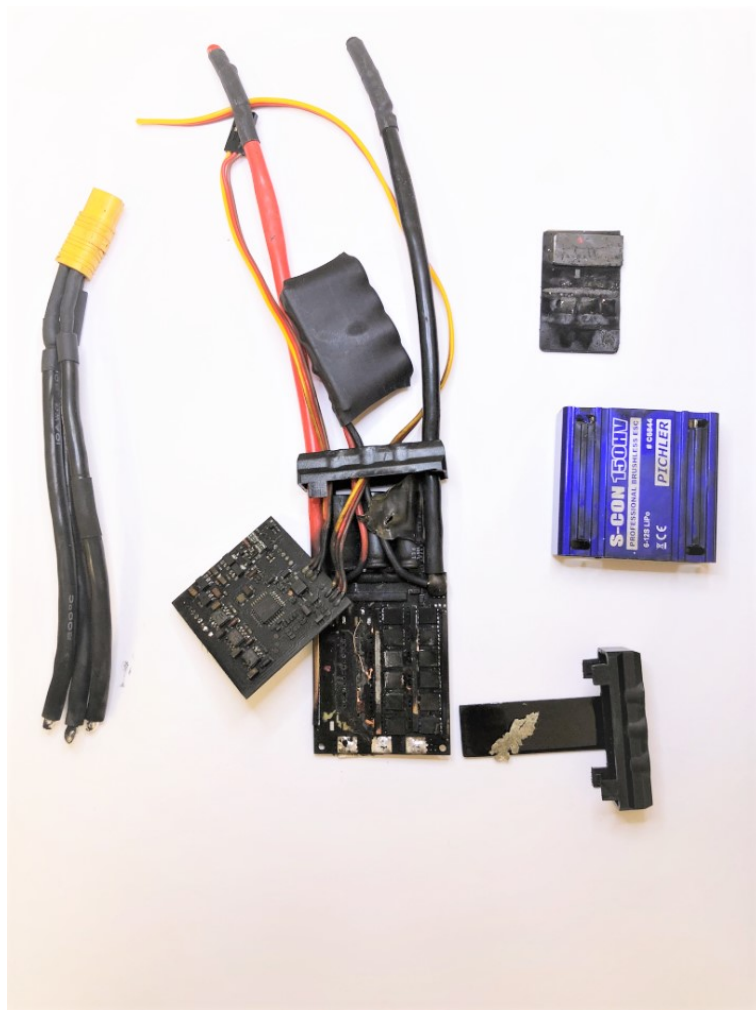
- 5 Liter Feuerlöschgranulat.



Appendix 42: Fire extinguishing granules

### A.3 Issues during the setup phase

During the setup phase, one motor and one controller was destroyed. After 30 mins of discontinuous operation, the isolation of one motor winding got damaged due to the lack of cooling. The resulting currents, induced by the short circuit in the motor, overheated the controller immediately. As a countermeasure for future testing, it is recommended, to measure the motor temperature and provide an active cooling mechanism to the test rig. Appendix 43 shows the inner parts of the burnt S-CON 150 controller.



**Appendix 43: Damaged S-CON 150 controller**

Appendix 44 shows the damaged motor from a top view. The winding section after 3 o'clock shows a darker color than the other, copper colored, windings. This provides strong evidence that this section was responsible for the short circuit.



**Appendix 44: Damaged motor Boost 160**